# Grasping Deformable Planar Objects: Squeeze, Stick/Slip Analysis, and Energy-Based Optimalities

Yan-Bin Jia  Feng Guo  Huan Lin
Department of Computer Science
Iowa State University
Ames, IA 50011, USA
jia,fguo,linhuan@iastate.edu

**Abstract**

Robotic grasping of deformable objects is difficult and under-researched, not simply due to the high computational cost of modeling. More fundamentally, several issues arise with the deformation of an object being grasped: a changing wrench space, growing finger contact areas, and pointwise varying contact modes inside these areas. Consequently, contact constraints needed for deformable modeling are hardly established at the beginning of the grasping operation. This paper presents a grasping strategy that squeezes the object with two fingers under specified displacements rather than forces. A 'stable' squeeze minimizes the potential energy for the same amount of squeezing, while a 'pure' squeeze ensures that the object undergoes no rigid body motion as it deforms. Assuming linear elasticity, a finite element analysis guarantees equilibrium and the uniqueness of deformation during a squeeze action. An event-driven algorithm tracks the contact regions as well as the modes of contact in their interiors under Coulomb friction, which in turn serve as the needed constraints for deformation update. Grasp quality is characterized as the amount of work performed by the grasping fingers in resisting a known push by some adversary finger. Simulation and multiple experiments have been conducted to validate the results over solid and ring-like 2D objects.

KEY WORDs — deformation, linear elasticity, finite element analysis, displacement-based grasping, stable and pure squeezes, analysis of segment contact, potential energy, work, grasp resistance

## 1 Introduction

Grasping deformable objects is inherently different from grasping rigid ones for which two types of analysis have been developed. Form closure (Reuleaux,1876) on a rigid object eliminates all of its degrees of freedom, while force closure (Nguyen 1988) keeps the object in equilibrium with the ability to resist any external wrench. On a deformable object, however, form closure is impossible to achieve due to the object's infinite degrees of freedom. Meanwhile, a force-closure analysis is inapplicable because torques applied on the object would vary as it deforms, even if contact forces could stay the same.

Robot grasping of deformable objects is an under-researched area for reasons that come from both mechanics and computation. Besides changing an object's geometry, deformation also causes its contacts with the grasping fingers to grow from points into areas. Inside such a contact area, a point that sticks on the corresponding finger may later slide, while a point that slides on the finger may later stick, as the deformation continues.

The focus on force and torque balances in rigid body grasping is no longer justified for deformable body grasping, because the prescribed forces cannot guarantee equilibrium on an initially free object once it starts to deform. Classical elasticity theory (Saada, 1993; Fung and Tong, 2001) only treats deformation of a mechanically constrained object under some applied loads, which are balanced by the constraint forces. At the start of a grasp, however, the object is under no such constraints. In our recent work (Jia et al. 2011) that considered specifying forces to achieve a grasp, extra geometric constraints had to be imposed on finger contacts in order to model the resulting deformation. Nevertheless, enforcement of such constraints required torques that could not be generated by the grasp itself in a realistic situation. The lesson was *not to achieve force equilibrium by means of specifying forces*.

The good news is that angular momentum is conserved (thus, torque equilibrium is guaranteed) under force equilibrium (Bower, 2009, pp. 49–52). Determining a small deformation based on linear elasticity comes down to solving a system of fourth order differential equations (Crandall et al., 1978, p. 288), which generally has no closed-form solution. In practice, computation is conducted using the finite element method (FEM) (Gallagher, 1975) under positional constraints. Forces and torques obtained via FEM will guarantee equilibrium following the fact that the object's stiffness matrix has a null space describing all of its rigid body movements. (This will be revealed more clearly via the force-displacement relationship (11) in Section 3.1.)

In practice it is also much easier to command a finger to move to a designated location than to control it to exert a prescribed force. Plus, force magnitude is not much of our concern as long as the object can be grasped.

For the above reasons, we choose to specify desired displacements for the grasping fingers (rather than the forces they exert). Knowing the finger locations, we hope to infer the current locations of those FEM nodes on the deformed object that are in contact with the fingers, and obtain the needed positional constraints for a deformation update. This, however, is not a trivial task. Since no part of the object is fixed during a grasp operation, contacts are maintained under friction only to some extent, and they evolve with deformation. To complicate the issue further, a contact point sliding on a finger imposes a force constraint (that the contact force must be along an edge of the contact friction cone) rather than a position constraint. Not only do we need to track which nodes are in contact, but also in which contact mode (stick or slip), in order to exert the correct constraints during an update of the deformed shape.

Table 1 shows a foam rubber square grasped by semicircular plastic tips mounted on two fingers of a Barrett Hand. The fingertips squeezed the object by translating toward each other respectively in the directions of the two opposing arrows drawn in the central image, until their distance along the common line of the arrows was reduced by 12%. The deformed shape, modeled as a triangular mesh under FEM, is superposed onto the real shape almost perfectly. Columns 1 and 3 compare the contact segments generated by simulation (row 1) with those observed in the experiment (row 2), on the left finger and the right finger, respectively, at the end of the squeeze shown in the central image. A total of 14 nodes on the object, marked by dots[1], were in contact with the fingertips. Among them, the 12 solid dots represent sticking contact nodes at the last moment, while the two hollow dots represent sliding contact nodes. The result was generated by a squeeze algorithm to be described in Section 5.

To model a grasping operation like the one shown in Table 1, we are facing a paradox inherent to classical elasticity theory. There, despite being a gradual physical process, deformation is assumed to happen instantaneously. This makes it almost impossible to predict a grasp's final configuration with area contacts that did not even exist at the beginning. To cope with this issue, deformable modeling needs to be conducted step by step. We track the varying set of finger contacts and their modes, and apply them as displacement constraints in predicting additional deformation. The shape change will eventually trigger a change in the

[1] Some nodes are labeled by their numbers in the mesh.

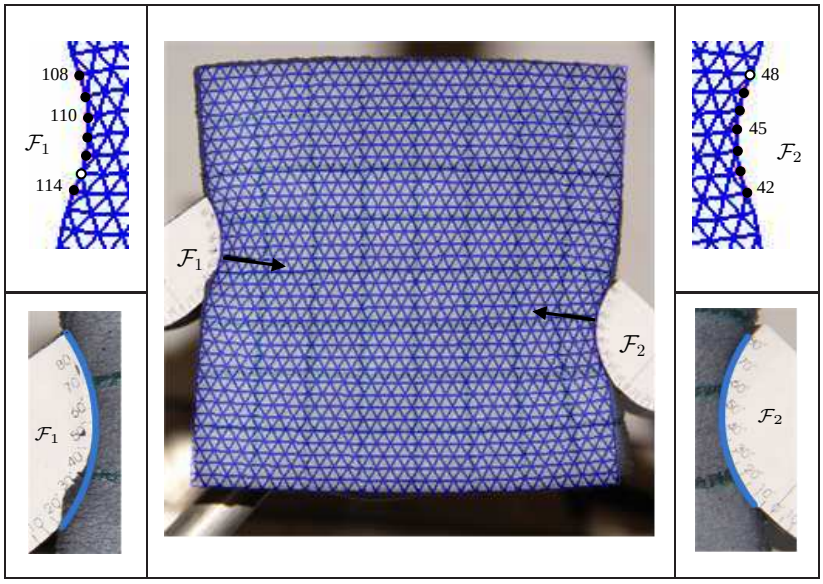


**Table 1**: Grasped foam rubber square with its deformed mesh superposed (center). The contact segments from simulation (row 1) each consist of six sticking nodes (solid dots) and one sliding node (hollow dot) numbered in the ranges 108–114 and 42–48, respectively. Nodes 110 and 45 were the initial contacts $\boldsymbol{p}_i$ and $\boldsymbol{p}_j$ with the two fingers. The contact segments in the experiment (row 2) are enlarged from the central image.

contact configuration, starting a new round of deformation update. To do this requires a contact mode analysis with event detection that is quite different from the one performed in rigid body dynamics.

The computational issue we have to face is the high cost of FEM-based deformable modeling. The subcubic time complexity in the number of discretization nodes is typically high for accurate modeling.[2] To make the matter worse, repeated deformation computations are needed to search for a successful grasp or to choose one with the best quality. The standard FEM procedure exerts every fixed node constraint by eliminating the corresponding row and column from the object's stiffness matrix. This is inapplicable to a grasping situation, since the (reduced) stiffness matrix varies whenever the contacts change. An improvement is made possible in this paper by carrying out all computation directly on the original stiffness matrix, which has its spectral decomposition precomputed. This can reduce the cost of a grasp test for point fingers to linear time.

The last issue that will be tackled in this paper is how to measure the quality of a grasp of a deformable object. On a rigid body, the grasping forces do not cause any deformation, thereby conduct no work. Existing metrics for rigid body grasps are mostly force-centered, either to minimize the possibility of violating some hard constraints, to maximize the worst-case adversary force resistible by a 'unit' total grasping force, or to minimize the maximum contact force by some finger to resist a known adversary force. On a deformable object, the grasping fingers perform work, most of which are converted into the object's strain energy through deformation. It is therefore natural for *a quality measure to be energy-based.* Particularly, we may measure a grasp in terms of stability from the energy point of view, or by the amount of work it will perform to resist an external disturbing force.

[2]Large deformations, meanwhile, can only be modeled by nonlinear elasticity (and computed using the even more expensive nonlinear FEM). They are not considered in this paper.

## 1.1 Paper Outline

This paper investigates two-finger grasping of a deformable object by squeezing it. We refer to the grasp thus formed as a *squeeze grasp*. Some rather mild assumptions are made below.

(a) The object is deformable, isotropic, and either planar or thin $2\frac{1}{2}$D.

(b) The object or its cross section is bounded by a continuously differentiable curve.

(c) The two grasping fingers are rigid with point or rounded tips.

(d) The fingers are coplanar and in frictional contact with the object.

(e) Gravity and dynamics are ignored.

(f) The grasp yields a small deformation within the scope of the linear elasticity theory.

In classical elasticity theory, deformation happens instantaneously. In this paper, we will sometimes picture deformation as a continuous process happening in an infinitesimal amount of time, in order to characterize the growing contact areas between the object and the fingers.

The initial finger placement needs to prevent all Euclidean motion, leaving deformation the only possibility. In the presence of friction, the placement would have to be force closure if the object were rigid. From a result by Nguyen (1988), the segment connecting the two initial contact points must lie inside their friction cones. Under a squeeze, each contact point will grow into a segment in which the points may switch their contact modes between stick and slip. The contact will not slide as long as one point on the segment sticks.

Section 2 will briefly review some basics of linear elasticity, examine displacement fields that yield rigid body movements or pure deformations via an introduced inner product, and characterize stable and pure finger squeezes of a deformable object. Section 3 will describe how to compute the deformation of an object under the FEM from specified displacements of its boundary contact nodes, and study the discrete versions of stable and pure squeezes. Section 4 will investigate deformation yielded by two translating point fingers in fixed contact with the object. Accounting for frictional segment contact, Section 5 will present an event-driven grasping algorithm that tracks deformation and contact configuration during a squeeze. A contact mode analysis will also be performed. In Section 6, we will construct grasps that perform minimum work to resist an adversary finger, progressing from the cases of fixed point and segment contacts to that of frictional segment contacts. Section 7 will be on grasping ring-like objects that make frictional point contacts with the grasping fingers. Several experiments will be described in Sections 5.5, 6.4, and 7.2 to validate the introduced grasping and optimization algorithms. Some discussion on future research will follow in Section 8.

## 1.2 Related Work

Rigid body grasping is an extensively studied topic rich with theoretical analyses, algorithmic syntheses, and implementations with robotic hands (Bicchi and Kumar, 2000). Salisbury and Roth (1983) deemed a hand design acceptable if the hand could not only immobilize a grasped object but also impart a desired force and displacement to the object that it was interacting with.

First-order form closure (Rimon and Burdick, 1996) is widely regarded as equivalent to force closure with frictionless contacts. Mishra et al. (1987) gave upper bounds on the numbers of contact points sufficient and/or necessary for form closure. Tighter bounds were later derived for 2D and 3D objects with piecewise

smooth boundaries (Markenscoff et al., 1990). Algorithms were developed to compute all form closure grasps of polygonal parts (Brost and Goldberg, 1994; van der Stappen et al., 2000). There was also work (Rimon and Blake, 1999; Rodriguez et al., 2012) on 'caging' an object with imposed frictionless contacts such that it could move but not escape.

Two-finger force-closure grasps of 2D objects are efficiently computable for polygons (Nguyen, 1988) and piecewise smooth curved shapes (Ponce et al., 1993). Ponce et al. (1997) also gave algorithms for grasping 3D objects. Trinkle (1992) formulated the test for force closure as a linear program with an objective function that measured the distance from losing the closure.

The notion of task ellipsoid (Li and Sastry, 1988) formalized the idea that the choice of a grasp ought to be based on its capacity to generate wrenches that were relevant to the task. Grasp quality measures for multifingered hands considered selection of internal grasping forces that were furthest from violating any closure, friction, or mechanical constraints (Kerr and Roth, 1986), or were directly derived from the grasp matrix which characterized the wrench space of a grasp (Li and Sastry, 1988). Grasp metrics for polygons and polyhedra often sought to maximize the worst-case external force that could be resisted by a unit grasping force (Markenscoff and Papadimitriou, 1989; Mirtich and Canny, 1994; Jia, 1995). Mishra (1995) offered a summary on various grasp metrics, addressing the trade-offs among grasp goodness, object geometry, the number of fingers, and the computational complexity for grasp synthesis. Some recent work (Buss et al., 1998; Boyd and Wegbreit 2007) focused on minimizing the maximum magnitude of the applied force at any frictional contact of a grasp in order to maintain equilibrium against a known adversary wrench, via employing semidefinite programming techniques.

Less work exists on grasping deformable objects, a problem that needs to deal with changes in the local contact geometry as well as the global object geometry caused by the physical action. The concept of bounded force-closure (Wakamatsu et al., 1996) was proposed for this type of grasps. Hirai et al. (2001) showed that visual and tactile information were effective on controlling the motion of a grasped deformable object. The deformation-space approach (Gopalakrishnan and Goldberg, 2005) characterized the optimal grasp of a deformable part as the one from which the potential energy needed for a release equals the amount at the part's elastic limit.

In contrast, manipulation of flexible linear objects such as wires or ropes has been a very active area, with work on static modeling (Wakamatsu and Hirai, 2004), knotting and unknotting (Saha and Isto, 2006; Matsuno and Fukuda, 2006; Ladd and Kavraki, 2004; Wakamatsu et al., 2006), pickup (Remde et al., 1999), and path planning (Moll and Kavraki, 2006). These operations, however, can be carried out without a serious need for deformable modeling.

Sinha and Abel (1992) proposed a model for the deformation of contact regions under a grasp. It predicted normal and tangential contact forces with no concern of global deformation or grasp computation. Luo and Xiao (2006) demonstrated that simulation accuracy and efficiency could be improved based on derived geometric properties at a deformable contact. The recent work involving the first author (Tian and Jia 2010) investigated deformable modeling of shell-like objects that were already grasped under point contacts.

More thorough investigations were conducted by the mechanics community on the elastic contact problem concerned with two deformable bodies under a known applied load. The gradual nature of the physical process suggests iterative updates of the growing contact region(s). In the work by Francavilla and Zienkiewicz (1975), an FEM-based solution was given to the 2D elastic contact problem under no friction. It was extended to incorporate Coulomb friction by Okamoto and Nakazawa (1979) and by Sachdeva and Ramakrishnan (1981) via iterative updating of the contact zone and the modes of individual contact nodes: stick, slip, contact break, or contact establishment. In each iteration, FEM computed the deformed shape

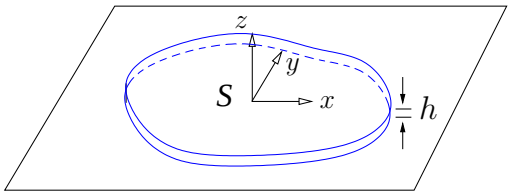


**Figure 1**: Thin flat object.

based on some position and friction constraints derived from the contact modes under Coulomb friction. This event-based approach was extended by Chandrasekaran et al. (1987) to handle geometric and physical nonlinearities as well as node-edge contacts in solving for the exact loading condition from prescribed displacements.

This paper combines the results in two conference papers: Guo et al. (2013) on squeeze grasping of deformable objects and Jia et al. (2013) on optimal squeezing of such objects in order to resist external disturbances. New materials include a physics-based characterization of squeeze strategies independent of any discrete representation of deformation, and some most recent experimental findings.

### 1.3 Notation

In this paper, sets of integers (or indices) are represented by English letters in the blackboard bold font (e.g., $\mathbb{I}$). Points and vectors are always denoted by bold face letters, English or Greek (e.g., $\boldsymbol{v}$). A vector with a caret (e.g., $\hat{\boldsymbol{v}}$) is a unit vector. A subvector consisting of some entries from a vector $\boldsymbol{v}$ is denoted as $\bar{\boldsymbol{v}}$. A cross product of two tuples is treated as a scalar whenever no ambiguity arises.

By convention, $I_n$, integer $n > 0$, denotes an $n \times n$ identity matrix. The null space, column space, and rank of a matrix $M$ are denoted by $\mathrm{null}(M)$, $\mathrm{col}(M)$, and $\mathrm{rank}(M)$, respectively.

Whether an object deforms or not, a node in its FEM representation with $n$ nodes is referred to as $\boldsymbol{p}_i$, for $1 \leq i \leq n$, . When appearing in an expression, $\boldsymbol{p}_i$ also refers to the node's original location (before deformation). A displacement of the node $\boldsymbol{p}_i$ is referred to as $\boldsymbol{\delta}_i$, and its displaced location as $\tilde{\boldsymbol{p}}_i = \boldsymbol{p}_i + \boldsymbol{\delta}_i$.

Metric system units are used throughout the paper. In particular, we use meter for length, Newton for force, Pascal for pressure, and Joule for work and energy. All units will be omitted from now on.

## 2 Stable and Pure Deformations

This section begins with a review of plane linear elasticity, and follows with a characterization of rigid body displacements. To prepare for the later study of grasping, it introduces an inner product for two displacement fields, and the notions of pure and stable deformations of an object induced by the specified movements of a subset of its boundary points.

### 2.1 Linear Plane Elasticity

Consider a thin flat object shown in Figure 1 with its thickness $h$ significantly less than its two other dimensions. Essentially, the object is a generalized cylinder which results from translating the region $S$ bounded by a closed simple curve in the $xy$-plane along the $z$-direction upward and downward each by $h/2$. The origin is placed at the centroid of $S$.

In this paper, we consider *plane stress* (Fung and Tong, 2001, pp. 280–281) parallel to the $xy$-plane. It assumes zero normal stress $\sigma_z$ along the $z$-axis and zero shear stresses $\tau_{xz}$ and $\tau_{yz}$ in the $x$-$z$ and $y$-$z$ planes, respectively. This leaves the normal stress components $\sigma_x$ and $\sigma_y$ in the $x$- and $y$-directions, respectively, and the shear stress $\tau_{xy}$ in the $x$-$y$ plane.

Under a *displacement field* $\boldsymbol{\delta} = (u(x, y), v(x, y))^T$ (the field is continuously differentiable with respect to $x$ and $y$), every point $(x, y)^T$ inside $S$ moves to $(x + u, y + v)^T$. The same displacement applies to all the points inside the object that are vertically above or below the point $(x, y)^T$. The normal strains $\epsilon_x$ and $\epsilon_y$ along the $x$- and $y$-axes, respectively, and the shearing strain $\gamma_{xy}$ are given below:

$$\begin{aligned} \epsilon_x &= \frac{\partial u}{\partial x}, \\ \epsilon_y &= \frac{\partial v}{\partial y}, \\ \gamma_{xy} &= \frac{\partial u}{\partial y} + \frac{\partial v}{\partial x}. \end{aligned} \tag{1}$$

Under Hooke's law (Crandall et al., 1978, p. 284), the following stress-strain relationships hold:

$$\begin{aligned} \epsilon_x &= \frac{1}{E}(\sigma_x - \nu\sigma_y), \\ \epsilon_y &= \frac{1}{E}(\sigma_y - \nu\sigma_x), \\ \gamma_{xy} &= \frac{2(1+\nu)}{E}\tau_{xy}, \end{aligned} \tag{2}$$

where $E$ and $\nu$ are Young's modulus and Poisson's ratio of the material, respectively, with $E > 0$ and $-1 \leq \nu \leq \frac{1}{2}$.[3] The strain energy of the object is (Crandall et al., 1978, p. 302)

$$U = \frac{h}{2}\iint_S \left( \frac{E}{1-\nu^2}\left(\epsilon_x^2 + 2\nu\epsilon_x\epsilon_y + \epsilon_y^2\right) + \frac{E}{2(1+\nu)}\gamma_{xy}^2 \right) dxdy. \tag{3}$$

The above expression excludes the value $\nu = -1$, as we will from now on since it is a theoretical limit not achieved by common materials.

Suppose $\boldsymbol{\delta}$ is due to external forces applied in the plane at some boundary points, which form a set $\Gamma$. Denote by $\boldsymbol{f}(x, y)$ the force acts at $(x, y)^T \in \Gamma$. The total potential of these forces is

$$W = -\sum_{(x,y)^T \in \Gamma} \boldsymbol{\delta}(x, y)^T \boldsymbol{f}(x, y). \tag{4}$$

Its sum with the strain energy constitutes the total potential energy of the system:

$$\Pi = U + W. \tag{5}$$

The principle of minimum potential energy states that $\boldsymbol{\delta}$ minimizes $\Pi$.

[3] Most materials have Poisson's ratio values ranging between 0 and $\frac{1}{2}$.

## 2.2 Rigid Body Displacement

A displacement field does not necessarily cause the object to deform. It may simply make it undergo a rigid body movement in the form of a translation and/or a rotation. If not deformed at all, $\epsilon_x = \epsilon_y = \gamma_{xy} = 0$, resulting in zero strain energy according to (3). Next is a known result that characterizes this type of displacement fields, together with our simple proof.

**Theorem 1** *Under linear elasticity, any displacement field $\boldsymbol{\delta} = (u(x,y), v(x,y))^T$ that yields zero strain energy is linearly spanned by the following three fields:*

$$\boldsymbol{t}_x = \begin{pmatrix} 1 \\ 0 \end{pmatrix}, \qquad \boldsymbol{t}_y = \begin{pmatrix} 0 \\ 1 \end{pmatrix}, \qquad \text{and} \qquad \boldsymbol{r} = \begin{pmatrix} -y \\ x \end{pmatrix}. \tag{6}$$

**Proof** Suppose $U = 0$ under a displacement field $\boldsymbol{\delta} = (u, v)^T$. The integrand in (3) can be rewritten as a sum of non-negative terms with the following substitution:

$$\epsilon_x^2 + 2\nu\epsilon_x\epsilon_y + \epsilon_y^2 = (1 \mp \nu)(\epsilon_x^2 + \epsilon_y^2) \pm \nu(\epsilon_x \pm \epsilon_y)^2, \tag{7}$$

where the top symbol in each of '$\mp$', '$\pm$', '$\pm$' on the right hand side above is chosen when $0 \le \nu \le \frac{1}{2}$, and the bottom symbol in each is chosen when $-1 < \nu < 0$. We infer from $U = 0$ that the strains $\epsilon_x, \epsilon_y$, $\gamma_{xy}$ must vanish everywhere inside the body. Substituting (1) in, we integrate $\epsilon_x = 0$ and $\epsilon_y = 0$ to obtain $u = u(y)$ and $v = v(x)$. Since $\gamma_{xy} = 0$, $du/dy + dv/dx = 0$ holds inside the body. Because $u$ and $v$ do not share variables, the only possibility is that $dv/dx = -du/dy = c$, for some constant $c$. Integration of the two derivatives gives

$$\begin{pmatrix} u \\ v \end{pmatrix} = c\boldsymbol{r} + d\boldsymbol{t}_x + e\boldsymbol{t}_y,$$

for some constants $d$ and $e$. □

The fields $\boldsymbol{t}_x$ and $\boldsymbol{t}_y$ respectively describe unit translations in the $x$ and $y$ directions, and the field $\boldsymbol{r}$ represents (or essentially, approximates) a rotation about the origin under linear elasticity. A displacement field $\boldsymbol{\delta}$ that generates no deformation is called a *rigid body displacement*.

## 2.3 Pure Deformation Field

A displacement field $\boldsymbol{\delta}$ often contains a rigid body displacement. This component will not affect the deformed shape, but only its translation and rotation as deformation takes place. A rigid body displacement (even just a translation) is unnecessary from the perspective of grasping. Also, since a large rotation cannot be modeled by linear elasticity theory, it is often desirable to prevent any rotation if possible.

Therefore, we often want to extract the remaining component of $\boldsymbol{\delta}$ that describes deformation only. To do this, we introduce an inner product for two displacement fields $\boldsymbol{\alpha}(x,y)$ and $\boldsymbol{\beta}(x,y)$:

$$\langle \boldsymbol{\alpha}, \boldsymbol{\beta} \rangle = \iint_S \boldsymbol{\alpha}^T \boldsymbol{\beta} \, dxdy. \tag{8}$$

All four properties of an inner product are clearly satisfied; namely, the above operator is commutative, distributive (with respect to addition), non-negative when $\boldsymbol{\alpha} = \boldsymbol{\beta}$, and scales with both $\boldsymbol{\alpha}$ and $\boldsymbol{\beta}$. The two fields are *orthogonal* if $\langle \boldsymbol{\alpha}, \boldsymbol{\beta} \rangle = 0$.

Under $\iint_S (x,y)^T \, dxdy = (0,0)^T$, it is easy to verify that the three displacement fields $\boldsymbol{t}_x, \boldsymbol{t}_y, \boldsymbol{r}$ given in (6) for translations and rotation are orthogonal to each other:

$$\langle \boldsymbol{t}_x, \boldsymbol{t}_y \rangle = \langle \boldsymbol{t}_x, \boldsymbol{r} \rangle = \langle \boldsymbol{t}_y, \boldsymbol{r} \rangle = 0.$$

The inner product (8) allows us to identify a displacement field $\boldsymbol{\delta}(x,y)$ with a 'vector' in the infinite-dimensional space of all displacement fields. Applying the Gram-Schmidt orthogonalization (Rice, 1963, pp.45–48), we remove from $\boldsymbol{\delta}$ its projections onto $\boldsymbol{t}_x, \boldsymbol{t}_y, \boldsymbol{r}$, yielding

$$\boldsymbol{\delta}_\perp = \boldsymbol{\delta} - \frac{\langle \boldsymbol{\delta}, \boldsymbol{t}_x \rangle}{\langle \boldsymbol{t}_x, \boldsymbol{t}_x \rangle} \boldsymbol{t}_x - \frac{\langle \boldsymbol{\delta}, \boldsymbol{t}_y \rangle}{\langle \boldsymbol{t}_y, \boldsymbol{t}_y \rangle} \boldsymbol{t}_y - \frac{\langle \boldsymbol{\delta}, \boldsymbol{r} \rangle}{\langle \boldsymbol{r}, \boldsymbol{r} \rangle} \boldsymbol{r}. \tag{9}$$

The resulting displacement field $\boldsymbol{\delta}_\perp$, orthogonal to $\boldsymbol{t}_x, \boldsymbol{t}_y, \boldsymbol{r}$, contains no rigid body movement. It is called a *pure deformation field*.

### 2.4 Stable and Pure Squeezes

In this paper, we look at grasping an object under specified displacements for some boundary points. Denote by $\Gamma$ the set formed by these points, and for every point $(x,y)^T \in \Gamma$, $\boldsymbol{\delta}_\Gamma(x,y)$ its specified displacement. In the context of grasping, such displacements are due to a squeeze action performed by the grasping fingers, which make frictional contacts with the object at these points. The fingers can only exert compressive forces at the points in $\Gamma$.[4] Hence, $\boldsymbol{\delta}_\Gamma(x,y)$ must be pointing inward at every point $(x,y)^T \in \Gamma$. If this condition is satisfied, we refer to $\boldsymbol{\delta}_\Gamma$ as a *squeeze*.

The contact displacements, trackable from the movements of the fingers, will serve as the positional constraints over the object's deformation.[5] The resulting displacement field $\boldsymbol{\delta}(x,y)$ can be determined by solving a system of second order partial differential equations for equilibrium (Crandall et al. 1978), or more practically, using a discretization method such as the finite element method (FEM) (Gallagher 1975) or the boundary element method (BEM) (Aliabadi 2002). Apparently, $\boldsymbol{\delta}$ specializes to $\boldsymbol{\delta}_\Gamma$ over $\Gamma$.

Two types of squeeze are introduced out of different considerations. On the one hand, we expect the resulting deformation to be 'stable' for the same amount of squeezing. This leads to a squeeze $\boldsymbol{\delta}_\Gamma$ that minimizes the potential energy of the system among all squeezes of the same magnitude. Such a squeeze is called a *stable squeeze*.

On the other hand, we expect a squeeze to generate a pure deformation of the object, in order to avoid rotation and translation. Such a squeeze $\boldsymbol{\delta}_\Gamma$ is called a *pure squeeze* since the solution displacement field $\boldsymbol{\delta}$ is a pure deformation field.

We can also characterize the optimal resistance to a translating adversary finger as the minimum work done by the grasping fingers during their extra squeeze to counter this disturbance. In doing so, all fingers (including the adversary one) achieve a stable squeeze (after some relaxation) or a pure squeeze. In the remainder of this paper, our study will be focused on stable and pure squeezes in the FEM framework.

## 3 Deformation from Contact Displacements

This section begins with a review of the FEM, characterizing the null space of the stiffness matrix. It then describes how to determine the shape of an object from prescribed displacements of some boundary nodes. The section ends with a study of stable and pure contact displacements, which are the discrete counterparts to stable and pure squeezes.

[4] Sticky fingers are not considered in this paper, as in most robot grasping literature.

[5] As shown later in Section 5, force constraints such as the one for sliding under Coulomb friction can also be dealt with.

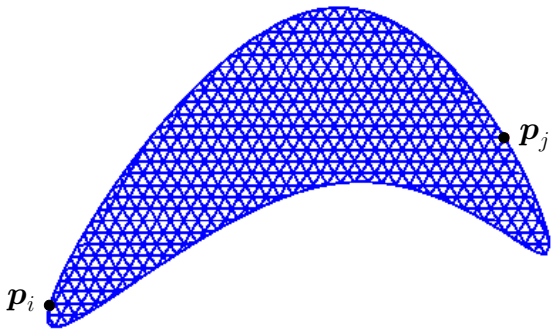


**Figure 2**: Meshed object with 517 nodes, including 112 on the boundary.

### 3.1 Finite Element Method

Generally, the strain energy integral (3) has no closed form. It is computed using the FEM as follows. Discretize the object's cross section into a finite number of elements with $n$ vertices (or nodes) $\boldsymbol{p}_k = (x_k, y_k)^T$, for $1 \le k \le n$. In this paper, triangular elements are used.[6] Figure 2 shows an example. Under deformation, every node $\boldsymbol{p}_k$ is displaced by $\boldsymbol{\delta}_k$ to the location $\tilde{\boldsymbol{p}}_k = \boldsymbol{p}_k + \boldsymbol{\delta}_k$. The displacement of any interior point of an element is linearly interpolated over those of its three vertices. The deformed shape of the object is thus completely described by $\boldsymbol{\Delta} = (\boldsymbol{\delta}_1^T, \ldots, \boldsymbol{\delta}_n^T)^T$, referred to as the *displacement vector*[7].

Given the displacement vector $\boldsymbol{\Delta}$, we obtain the strain energies of individual elements via separate integrations of (3), and then assemble the results into the total strain energy,

$$U = \frac{1}{2}\boldsymbol{\Delta}^T K \boldsymbol{\Delta}, \tag{10}$$

where the $2n \times 2n$ matrix $K$ is referred to as the *stiffness matrix*. The symmetry of $K$ follows from Betti's law[8] (Saada, 1993, pp. 447–448). The non-negativeness of strain energy ensures that $K$ is positive semidefinite.

Aggregate the external forces $\boldsymbol{f}_i$ applied at the nodes $\boldsymbol{p}_i$, $1 \le i \le n$, into a vector $\boldsymbol{F}$. The total potential of these external forces is $W = -\boldsymbol{\Delta}^T \boldsymbol{F}$. Minimization of the total potential energy $\Pi = U + W$ over $\boldsymbol{\Delta}$ yields familiar constitutive equation,

$$K\boldsymbol{\Delta} = \boldsymbol{F}. \tag{11}$$

It is easy to verify that $\Pi = -U$ holds at equilibrium.

The strain energy $U$ is zero if and only if $K\boldsymbol{\Delta} = 0$, that is, $\boldsymbol{\Delta} \in \mathrm{null}(K)$. Such a vector $\boldsymbol{\Delta}$ represents a rigid body motion (Gallagher, 1975, p. 48). Meanwhile, from its form (3) along with (7), $U$ is zero if and only if it is zero over every triangular element. By Theorem 1 and from linear interpolation within an

[6] A mesh is generated using our simplified version of the GridMesh algorithm (Nealen et al., 2009), which, roughly speaking, places a closed simple curve onto a triangular grid and moves the vertices of those crossed triangles (after possible further subdivisions) onto the curve via a bijective mapping followed by some optimization.

[7] also called the element displacement field by Gallagher (1975)

[8] Betti's law states that the deflection at one point in a given direction caused by a load at another point in a second direction equals the deflection at the second point in the second direction due to a unit load at the first point in the first direction.

element, we infer that $\mathrm{null}(K)$ is spanned by the following three $2n$-vectors:

$$\begin{aligned} \boldsymbol{w}_x &= (1,0,\ldots,1,0)^T, \\ \boldsymbol{w}_y &= (0,1,\ldots,0,1)^T, \\ \boldsymbol{w}_r &= (-y_1,x_1,\ldots,-y_n,x_n)^T. \end{aligned} \tag{12}$$

Equations $\boldsymbol{w}_x^T\boldsymbol{F} = (\boldsymbol{w}_x^T K)\boldsymbol{\Delta} = 0$ and $\boldsymbol{w}_y^T\boldsymbol{F} = 0$ together imply force equilibrium $\sum_{i=1}^n \boldsymbol{f}_i = 0$, while equation $\boldsymbol{w}_r^T\boldsymbol{F} = 0$ implies torque equilibrium $\sum_{i=1}^n \boldsymbol{p}_i \times \boldsymbol{f}_i = 0$.

The positive semidefiniteness of $K$ implies that it has $2n-3$ positive eigenvalues $\lambda_1, \lambda_2, \ldots, \lambda_{2n-3}$. Let $\boldsymbol{v}_1, \boldsymbol{v}_2, \ldots, \boldsymbol{v}_{2n-3}$ be the corresponding unit eigenvectors that are orthogonal to each other. We normalize $\boldsymbol{w}_x, \boldsymbol{w}_y$, and the orthogonal component

$$\boldsymbol{w}_\perp = \boldsymbol{w}_r - \frac{\boldsymbol{w}_r^T\boldsymbol{w}_x}{\boldsymbol{w}_x^T\boldsymbol{w}_x}\boldsymbol{w}_x - \frac{\boldsymbol{w}_r^T\boldsymbol{w}_y}{\boldsymbol{w}_y^T\boldsymbol{w}_y}\boldsymbol{w}_y \tag{13}$$

of $\boldsymbol{w}_r$ to obtain three orthogonal unit eigenvectors,

$$\boldsymbol{v}_{2n-2} = \frac{\boldsymbol{w}_x}{\sqrt{n}}, \quad \boldsymbol{v}_{2n-1} = \frac{\boldsymbol{w}_y}{\sqrt{n}}, \quad \text{and} \quad \boldsymbol{v}_{2n} = \frac{\boldsymbol{w}_\perp}{\|\boldsymbol{w}_\perp\|}. \tag{14}$$

It follows from the Spectral Theorem (Strang, 1993, p. 273) that

$$K = V\Lambda V^T, \tag{15}$$

where $V = (v_{ij}) = (\boldsymbol{v}_1, \boldsymbol{v}_2, \ldots, \boldsymbol{v}_{2n})$ and $\Lambda = \mathrm{diag}(\lambda_1, \ldots, \lambda_{2n-3}, 0, 0, 0)$.

The discrete counterpart of the inner product (8) acts on two displacement vectors $\boldsymbol{\Delta} = (\boldsymbol{\delta}_1^T, \ldots, \boldsymbol{\delta}_n^T)^T$ and $\boldsymbol{\Delta}' = (\boldsymbol{\delta}_1'^T, \ldots, \boldsymbol{\delta}_n'^T)^T$ as follows:

$$\langle \boldsymbol{\Delta}, \boldsymbol{\Delta}' \rangle = \sum_{k=1}^n \boldsymbol{\delta}_k^T \boldsymbol{\delta}_k'. \tag{16}$$

Similarly, as in the continuous case, from $\boldsymbol{\Delta}$ we can construct a displacement vector $\boldsymbol{\Delta}_\perp$ that contains no rigid body movement and generates the same deformation up to translation and rotation. It is given as

$$\begin{aligned} \boldsymbol{\Delta}_\perp &= \boldsymbol{\Delta} - \frac{\langle \boldsymbol{\Delta}, \boldsymbol{w}_x \rangle}{\langle \boldsymbol{w}_x, \boldsymbol{w}_x \rangle}\boldsymbol{w}_x - \frac{\langle \boldsymbol{\Delta}, \boldsymbol{w}_y \rangle}{\langle \boldsymbol{w}_y, \boldsymbol{w}_y \rangle}\boldsymbol{w}_y - \frac{\langle \boldsymbol{\Delta}, \boldsymbol{w}_r \rangle}{\langle \boldsymbol{w}_r, \boldsymbol{w}_r \rangle}\boldsymbol{w}_r \\ &= \boldsymbol{\Delta} - \sum_{k=2n-2}^{2n} \langle \boldsymbol{\Delta}, \boldsymbol{v}_k \rangle \boldsymbol{v}_k \\ &= \boldsymbol{\Delta} - (\boldsymbol{v}_{2n-2}, \boldsymbol{v}_{2n-1}, \boldsymbol{v}_{2n})(\boldsymbol{v}_{2n-2}, \boldsymbol{v}_{2n-1}, \boldsymbol{v}_{2n})^T \boldsymbol{\Delta}, \end{aligned} \tag{17}$$

We refer to $\boldsymbol{\Delta}_\perp$ as the *pure deformation vector* equivalent to $\boldsymbol{\Delta}$.

### 3.2 Contact Displacement Vector

Because the stiffness matrix $K$ is singular, the constitutive equation (11) cannot be solved for the deformation $\boldsymbol{\Delta}$ even if the nodal force vector $\boldsymbol{F}$ is known. Extra constraints need to be imposed on some nodes to prevent any rigid body movement. In this paper, the nodal displacements $\boldsymbol{\delta}_1, \ldots, \boldsymbol{\delta}_n$ are due to the forces

exerted by the grasping fingers in contact with some boundary nodes $\boldsymbol{p}_{i_1}, \ldots, \boldsymbol{p}_{i_m}$, $i_1 < i_2 < \cdots < i_m$ (one finger may be in contact with multiple nodes). In Figure 2, for instance, $m = 2$ with $i_1 = i$ and $i_2 = j$. Zero external forces are applied at all interior nodes and non-contact boundary nodes; namely,

$$\boldsymbol{f}_k = \mathbf{0}, \qquad 1 \le k \le n \text{ and } k \neq i_1, \ldots, i_m. \tag{18}$$

Suppose the displacement $\boldsymbol{\delta}_{i_k}$ of every contact node $\boldsymbol{p}_{i_k}$, $1 \le k \le m$, is known[9]. We would like to determine the forces $\boldsymbol{f}_{i_k}$ exerted by the fingers at all contact nodes $\boldsymbol{p}_{i_k}$ and the displacement vector $\boldsymbol{\Delta}$.

Let us substitute the decomposition (15) of $K$ into the constitutive equation (11), and left multiply both sides of the resulting equation by $V^T$. Because $V$ is an orthogonal matrix, this yields $\Lambda V^T \boldsymbol{\Delta} = V^T \boldsymbol{F}$, which expands into $2n$ equations:

$$\begin{aligned} \boldsymbol{v}_k^T \boldsymbol{\Delta} &= \frac{1}{\lambda_k} \boldsymbol{v}_k^T \boldsymbol{F}, \qquad k = 1, \ldots, 2n-3; \\ 0 &= \boldsymbol{v}_k^T \boldsymbol{F}, \qquad k = 2n-2, 2n-1, 2n. \end{aligned}$$

With them we represent $\boldsymbol{\Delta}$ in terms of $\boldsymbol{v}_1, \boldsymbol{v}_2, \ldots, \boldsymbol{v}_{2n}$ via projection:

$$\boldsymbol{\Delta} = \sum_{k=1}^{2n-3} \frac{1}{\lambda_k} (\boldsymbol{v}_k^T \boldsymbol{F}) \boldsymbol{v}_k + \sum_{k=2n-2}^{2n} g_k \boldsymbol{v}_k, \tag{19}$$

where $g_k = \boldsymbol{v}_k^T \boldsymbol{\Delta}$, $k = 2n-2, 2n-1, 2n$, represent the components of $\boldsymbol{\Delta}$ that form a rigid body displacement.

From now on, we denote by $\bar{\boldsymbol{a}}$ the vector that selects the entries from a $2n$-vector $\boldsymbol{a} = (a_1, \ldots, a_{2n})^T$ indexed at $2i_1 - 1, 2i_1, \ldots, 2i_m - 1, 2i_m$, which correspond to the contact nodes $\boldsymbol{p}_{i_1}, \ldots, \boldsymbol{p}_{i_m}$. For instance,

$$\bar{\boldsymbol{v}}_k = (v_{2i_1-1,k}, v_{2i_1,k}, \ldots, v_{2i_m,k})^T, \tag{20}$$

for $1 \le k \le n$, and $\bar{\boldsymbol{F}} = (\boldsymbol{f}_{i_1}^T, \ldots, \boldsymbol{f}_{i_m}^T)^T$. Since $\boldsymbol{f}_k = \mathbf{0}$, for $k \neq i_1, \ldots, i_m$, we have $\bar{\boldsymbol{v}}_k^T \bar{\boldsymbol{F}} = \boldsymbol{v}_k^T \boldsymbol{F}$. Equation (19) then becomes

$$\boldsymbol{\Delta} = (\boldsymbol{v}_1, \ldots \boldsymbol{v}_{2n}) \begin{pmatrix} \bar{\boldsymbol{v}}_1^T \bar{\boldsymbol{F}} / \lambda_1 \\ \vdots \\ \bar{\boldsymbol{v}}_{2n-3}^T \bar{\boldsymbol{F}} / \lambda_{2n-3} \\ \boldsymbol{g} \end{pmatrix}, \tag{21}$$

where $\boldsymbol{g} = (g_{2n-2}, g_{2n-1}, g_{2n})^T$. Assemble the equations for $\boldsymbol{\delta}_{i_1}, \ldots, \boldsymbol{\delta}_{i_m}$ within (21):

$$\bar{\boldsymbol{\Delta}} = \begin{pmatrix} \boldsymbol{\delta}_{i_1} \\ \vdots \\ \boldsymbol{\delta}_{i_m} \end{pmatrix} = A \bar{\boldsymbol{F}} + B \boldsymbol{g}, \tag{22}$$

where

$$A = \sum_{k=1}^{2n-3} \frac{1}{\lambda_k} \bar{\boldsymbol{v}}_k \bar{\boldsymbol{v}}_k^T, \tag{23}$$

$$B = (\bar{\boldsymbol{v}}_{2n-2}, \bar{\boldsymbol{v}}_{2n-1}, \bar{\boldsymbol{v}}_{2n}). \tag{24}$$

[9] from finger movements or sensor measurements, for instance

We refer to $\bar{\boldsymbol{\Delta}}$ as the *contact displacement vector*. It follows from (14) that $\mathrm{col}(B) = \mathrm{span}(\{\bar{\boldsymbol{w}}_x, \bar{\boldsymbol{w}}_y, \bar{\boldsymbol{w}}_r\})$, the subspace spanned by these three vectors.

Meanwhile, left multiplications of $\boldsymbol{v}_{2n-2}^T$, $\boldsymbol{v}_{2n-1}^T$, $\boldsymbol{v}_{2n}^T$ respectively with both sides of $K\boldsymbol{\Delta} = \boldsymbol{F}$ yield

$$\begin{aligned} 0 &= (\boldsymbol{v}_{2n-2}, \boldsymbol{v}_{2n-1}, \boldsymbol{v}_{2n})^T \boldsymbol{F} \\ &= B^T \bar{\boldsymbol{F}}. \qquad \text{(by (18))} \end{aligned} \tag{25}$$

Combine (22) and (25):

$$M \begin{pmatrix} \bar{\boldsymbol{F}} \\ \boldsymbol{g} \end{pmatrix} = \begin{pmatrix} \bar{\boldsymbol{\Delta}} \\ 0 \\ 0 \\ 0 \end{pmatrix}, \tag{26}$$

where

$$M = \begin{pmatrix} A & B \\ B^T & \mathbf{0} \end{pmatrix}. \tag{27}$$

By its definition (23), $A$ is symmetric, and so is $M$.[10]

### 3.3 Uniqueness of Deformation

If $\bar{\boldsymbol{F}}$ and $\boldsymbol{g}$ are solvable from (26), we will be able to determine the displacement vector $\boldsymbol{\Delta}$ from (21), and thus the deformed shape. First, a negative result is given regarding single contact.

**Lemma 2** *The matrix $M$ is singular if $m = 1$, that is, if there is only one contact node.*

**Proof** Let $\boldsymbol{p}_i$ be the sole contact node. Because the matrix $B^T$ is $3 \times 2$, the last three rows of $M$ in (27) are linearly dependent. □

Specifying the displacement of only one node is equivalent to pushing the object via single contact for the specified amount and then rotating it about the node. This is a rigid body movement. The good news is that $M$ becomes nonsingular for $m \geq 2$. To establish this, we need the following two lemmas.

**Lemma 3** *For $m \geq 2$, $\mathrm{rank}(B) = 3$.*

**Proof** It suffices to establish the claim for $m = 2$ from the form (24) of $B$. Equivalently, under (13) and (14), we show that the following three vectors are linearly independent:

$$\bar{\boldsymbol{w}}_x = \begin{pmatrix} 1 \\ 0 \\ 1 \\ 0 \end{pmatrix}, \qquad \bar{\boldsymbol{w}}_y = \begin{pmatrix} 0 \\ 1 \\ 0 \\ 1 \end{pmatrix}, \qquad \text{and} \qquad \bar{\boldsymbol{w}}_r = \begin{pmatrix} -y_{i_1} \\ x_{i_1} \\ -y_{i_2} \\ x_{i_2} \end{pmatrix}.$$

Clearly, $\bar{\boldsymbol{w}}_x$ and $\bar{\boldsymbol{w}}_y$ are orthogonal to each other. Subtract from $\bar{\boldsymbol{w}}_r$ its components that are along $\bar{\boldsymbol{w}}_x$ and $\bar{\boldsymbol{w}}_y$, yielding

$$\begin{aligned} \bar{\boldsymbol{w}}_\perp &= \bar{\boldsymbol{w}}_r - \frac{\bar{\boldsymbol{w}}_r^T \bar{\boldsymbol{w}}_x}{\bar{\boldsymbol{w}}_x^T \bar{\boldsymbol{w}}_x} \bar{\boldsymbol{w}}_x - \frac{\bar{\boldsymbol{w}}_r^T \bar{\boldsymbol{w}}_y}{\bar{\boldsymbol{w}}_y^T \bar{\boldsymbol{w}}_y} \bar{\boldsymbol{w}}_y \\ &= \frac{1}{2} \begin{pmatrix} y_{i_2} - y_{i_1} \\ x_{i_1} - x_{i_2} \\ y_{i_1} - y_{i_2} \\ x_{i_2} - x_{i_1} \end{pmatrix}. \end{aligned}$$

[10] Note that $A$ may be singular. In particular, $AB = 0$ when $n = m$. This implies $\mathrm{rank}(A) \leq 2n - 3$.

The vector $\bar{\boldsymbol{w}}_\perp$ does not vanish because $\boldsymbol{p}_{i_1} \neq \boldsymbol{p}_{i_2}$, and is orthogonal to $\bar{\boldsymbol{w}}_x$ and $\bar{\boldsymbol{w}}_y$. □

**Lemma 4** *The product $\boldsymbol{x}^T A\boldsymbol{x} > 0$ whenever $B^T\boldsymbol{x} = \mathbf{0}$, for any $2m$-vector $\boldsymbol{x} \neq 0$ with $m \geq 2$.*

**Proof** Consider the matrix $\bar{V} = (\bar{\boldsymbol{v}}_1, \ldots, \bar{\boldsymbol{v}}_{2n})$. The rows of $\bar{V}$ are also of $V$ and therefore orthogonal to each other. Hence, $\mathrm{rank}(\bar{V}) = 2m$, which is also the matrix's column rank.

It holds that every $2m$-vector $\boldsymbol{x} \in \mathrm{col}(\bar{V})$. Suppose $B^T\boldsymbol{x} = \mathbf{0}$. Namely, the vector $\boldsymbol{x}$ is orthogonal to $\bar{\boldsymbol{v}}_{2n-2}, \bar{\boldsymbol{v}}_{2n-1}, \bar{\boldsymbol{v}}_{2n}$. It must then be a linear combination of $\bar{\boldsymbol{v}}_1, \bar{\boldsymbol{v}}_2, \ldots, \bar{\boldsymbol{v}}_{2n-3}$. There must exist some $\bar{\boldsymbol{v}}_j$, $1 \leq j \leq 2n-3 \geq 2m-3 \geq 1$, such that $\bar{\boldsymbol{v}}_j^T\boldsymbol{x} \neq 0$. Therefore,

$$\begin{aligned} \boldsymbol{x}^T A\boldsymbol{x} &= \boldsymbol{x}^T \left( \sum_{k=1}^{2n-3} \frac{1}{\lambda_k} \bar{\boldsymbol{v}}_k \bar{\boldsymbol{v}}_k^T \right) \boldsymbol{x} \\ &\geq \frac{1}{\lambda_j} (\bar{\boldsymbol{v}}_j^T \boldsymbol{x})^2 \\ &> 0. \end{aligned}$$

□

**Theorem 5** *The matrix $M$ is nonsingular for $m \geq 2$.*

**Proof** It suffices to show that

$$M \begin{pmatrix} \bar{\boldsymbol{F}} \\ \boldsymbol{g} \end{pmatrix} \neq \mathbf{0} \tag{28}$$

whenever $\bar{\boldsymbol{F}} \neq \mathbf{0}$ or $\boldsymbol{g} \neq \mathbf{0}$. Consider the case $\bar{\boldsymbol{F}} = \mathbf{0}$ first. Then $\boldsymbol{g} \neq \mathbf{0}$ must hold. From (27) we have

$$M \begin{pmatrix} \bar{\boldsymbol{F}} \\ \boldsymbol{g} \end{pmatrix} = \begin{pmatrix} B\boldsymbol{g} \\ \mathbf{0} \end{pmatrix},$$

where

$$B\boldsymbol{g} = (\bar{\boldsymbol{v}}_{2n-2}, \bar{\boldsymbol{v}}_{2n-1}, \bar{\boldsymbol{v}}_{2n}) \begin{pmatrix} g_1 \\ g_2 \\ g_3 \end{pmatrix}.$$

By Lemma 3, $\mathrm{rank}(B) = 3$; thus $\bar{\boldsymbol{v}}_{2n-2}, \bar{\boldsymbol{v}}_{2n-1}, \bar{\boldsymbol{v}}_{2n}$ are linearly independent. This, together with $\boldsymbol{g} \neq 0$, implies $B\boldsymbol{g} \neq \mathbf{0}$. Hence (28) holds.

Next, consider that $\bar{\boldsymbol{F}} \neq \mathbf{0}$. If $B^T\bar{\boldsymbol{F}} \neq \mathbf{0}$, then (28) apparently holds given the form (27) of $M$. If $B^T\bar{\boldsymbol{F}} = \mathbf{0}$, we have

$$\begin{aligned} & (\bar{\boldsymbol{F}}^T, \boldsymbol{g}^T) M \begin{pmatrix} \bar{\boldsymbol{F}} \\ \boldsymbol{g} \end{pmatrix} \\ = \; & \bar{\boldsymbol{F}}^T A \bar{\boldsymbol{F}} + \boldsymbol{g}^T B^T \bar{\boldsymbol{F}} + \bar{\boldsymbol{F}}^T B\boldsymbol{g} \\ = \; & \bar{\boldsymbol{F}}^T A \bar{\boldsymbol{F}} && \text{(since } B^T\bar{\boldsymbol{F}} = \mathbf{0} \text{ and } \bar{\boldsymbol{F}}^T B = \mathbf{0}) \\ > \; & 0 && \text{(by Lemma 4).} \end{aligned}$$

The product would be zero if (28) did not hold. □

From now on, we consider only $m \geq 2$ since a grasp requires at least two fingers making contact with the object. Since $M$ is nonsingular, its inverse $M^{-1}$ exists and is symmetric because $M$ is:

$$M^{-1} = \begin{pmatrix} C & E \\ E^T & H \end{pmatrix}, \tag{29}$$

where $C, E, H$ have dimensions $2m \times 2m$, $2m \times 3$, and $3 \times 3$, respectively. We have

$$MM^{-1} = \begin{pmatrix} AC + BE^T & AE + BH \\ B^T C & B^T E \end{pmatrix} = I_{2m+3}. \tag{30}$$

Equation (26) now has the solution

$$\begin{pmatrix} \bar{\boldsymbol{F}} \\ \boldsymbol{g} \end{pmatrix} = \begin{pmatrix} C \\ E^T \end{pmatrix} \bar{\boldsymbol{\Delta}}. \tag{31}$$

We call $C$ the *reduced stiffness matrix* as it relates the forces exerted at the contact nodes to their specified displacements. The displacement vector $\boldsymbol{\Delta}$ is immediately obtained from $\bar{\boldsymbol{\Delta}}$ using (21) and (31):

$$\boldsymbol{\Delta} \;=\; V \begin{pmatrix} \bar{\boldsymbol{v}}_1^T C/\lambda_1 \\ \vdots \\ \bar{\boldsymbol{v}}_{2n-3}^T C/\lambda_{2n-3} \\ E^T \end{pmatrix} \bar{\boldsymbol{\Delta}}. \tag{32}$$

Equation (32) defines a linear mapping $\boldsymbol{\chi}$: $\bar{\boldsymbol{\Delta}} \to \boldsymbol{\Delta}$ that is trivially one-to-one since $\bar{\boldsymbol{\Delta}}$ is a subvector of $\boldsymbol{\Delta}$.

The potential energy form (10) is simplified to

$$\begin{aligned} U &= \frac{1}{2}\boldsymbol{\Delta}^T \boldsymbol{F} \\ &= \frac{1}{2}\bar{\boldsymbol{\Delta}}^T \bar{\boldsymbol{F}} \qquad \text{(since } \boldsymbol{f}_j = 0 \text{ for } j \neq i_1, \ldots, i_m\text{)} \\ &= \frac{1}{2}\bar{\boldsymbol{\Delta}}^T C \bar{\boldsymbol{\Delta}}. \qquad \text{(by (31))} \end{aligned} \tag{33}$$

**Corollary 6** *Suppose $\bar{\boldsymbol{\Delta}}$ with $m \geq 2$ is part of some rigid body displacement $\boldsymbol{\Delta}$. Then $\bar{\boldsymbol{F}} = \boldsymbol{0}$, and $\boldsymbol{\Delta}$ is given in (32).*

**Proof** Suppose $m \geq 2$. Let $\boldsymbol{\Delta}$ be a rigid body displacement that contains $\bar{\boldsymbol{\Delta}}$. By Theorem 5, $M^{-1}$ (and thus $C$) uniquely exists. Therefore, $\boldsymbol{\Delta}$ is uniquely determined from (32). This uniqueness implies that the vector $\bar{\boldsymbol{F}} = C\bar{\boldsymbol{\Delta}}$ must be contained in $\boldsymbol{F} = K\boldsymbol{\Delta} = \boldsymbol{0}$. Hence $\bar{\boldsymbol{F}} = \boldsymbol{0}$. □

The next theorem presents some facts about the submatrices of $M$ and $M^{-1}$, which will be used later in the analysis and design of grasping strategies. We refer the reader to Appendix A for a proof of the theorem.

**Theorem 7** *Suppose $m \geq 2$. The following statements hold for the submatrices of $M$ and $M^{-1}$ in (27) and (29).*

*(i) $C$ is symmetric and positive semidefinite such that*

$$\text{null}(C) = \text{col}(B). \tag{34}$$

*Consequently, the $2m$-dimensional space is a direct sum of the column spaces of $C$ and $B$, i.e.,*

$$\mathbb{R}^{2m} = \text{col}(C) \oplus \text{col}(B). \tag{35}$$

*(ii)* $\mathrm{rank}(AC) = 2m - 3$ *and* $AC$ *has only one eigenvalue 1 (of multiplicity* $2m - 3$*).*

*(iii)* $\mathbb{R}^{2m} = \mathrm{col}(AC) \oplus \mathrm{col}(E)$.

The spectral decomposition (15) of the stiffness matrix can be computed via singular value decomposition (SVD) in $O(n^3)$ time. The matrix $A$ requires $O(m^2 n)$ time to set up, so does the linear system (26). The inverse $A^{-1}$ can be easily computed in $O(m^3)$ time using, say, LU decomposition[11]. This is also the time needed to solve for $\bar{\boldsymbol{F}}$ and $\boldsymbol{g}$. The displacement of a non-contact boundary node is obtained according to (32) as follows. First, compute the product $(\bar{\boldsymbol{v}}_1, \ldots, \bar{\boldsymbol{v}}_{2n-3})^T C$ in $O(m^2 n)$ time. This determines the second matrix in (32) after divisions of the first $2n - 3$ entries in the product by $\lambda_1, \ldots, \lambda_{2n-3}$. Multiply the matrix with $\bar{\boldsymbol{\Delta}}$ in $O(mn)$ time. Then left multiply the resulting vector with the two rows in $V$ whose indices correspond to that of the node, spending extra $O(n)$ time to obtain its displacement. After SVD, the displacement vector $\boldsymbol{\Delta}$ can be computed in $O(m^2 n)$ time.

To determine the deformed shape, the displacement of every boundary node needs to be computed. For a uniform mesh, there are $O(\sqrt{n})$ nodes on the boundary. Therefore, $O(\sqrt{n})$ rows from $V$ need to be multiplied in the last stage described in the above paragraph, taking $O(n^{3/2})$ time. The overall computation after SVD therefore takes $O(n(m^2 + \sqrt{n}))$ time after SVD. Since $m$ is often very small and can be treated as a constant, the computation time reduces to $O(n^{3/2})$.

### 3.4 Pure Contact Displacement

The displacement vector $\boldsymbol{\chi}(\bar{\boldsymbol{\Delta}})$ resulting from the contact displacement $\bar{\boldsymbol{\Delta}}$ often contains some rigid body movement. Corollary 6 gives one situation where this happens. Sometimes it is desirable to convert $\bar{\boldsymbol{\Delta}}$ into a contact displacement vector $\bar{\boldsymbol{\Delta}}'$ that yields a pure deformation vector $\boldsymbol{\chi}(\bar{\boldsymbol{\Delta}}')$. Such a vector $\bar{\boldsymbol{\Delta}}'$ is referred to as a *pure contact displacement vector*.

**Theorem 8** *Suppose the contact displacement vector* $\bar{\boldsymbol{\Delta}}$ *yields the displacement field* $\boldsymbol{\Delta}$ *according to (32). Then the contact displacement vector* $(AC)\bar{\boldsymbol{\Delta}}$ *yields the equivalent pure deformation vector* $\boldsymbol{\Delta}_\perp$ *in (17).*

**Proof** From (22), we have $A\bar{\boldsymbol{F}} = \bar{\boldsymbol{\Delta}} - B\boldsymbol{g}$ which, after substitution of $\bar{\boldsymbol{F}} = C\bar{\boldsymbol{\Delta}}$, becomes

$$(AC)\bar{\boldsymbol{\Delta}} = \bar{\boldsymbol{\Delta}} - B\boldsymbol{g}.$$

Since the mapping $\boldsymbol{\chi}$ is linear, we have

$$\begin{aligned} \boldsymbol{\chi}((AC)\bar{\boldsymbol{\Delta}}) &= \boldsymbol{\chi}(\bar{\boldsymbol{\Delta}}) - \boldsymbol{\chi}(B\boldsymbol{g}) \\ &= \boldsymbol{\Delta} - \boldsymbol{\chi}(B\boldsymbol{g}). \end{aligned}$$

To establish $\boldsymbol{\chi}((AC)\bar{\boldsymbol{\Delta}}) = \boldsymbol{\Delta}_\perp$, we just need to show that

$$\begin{aligned} \boldsymbol{\chi}(B\boldsymbol{g}) &= (\boldsymbol{v}_{2n-2}, \boldsymbol{v}_{2n-1}, \boldsymbol{v}_{2n})(\boldsymbol{v}_{2n-2}, \boldsymbol{v}_{2n-1}, \boldsymbol{v}_{2n})^T \boldsymbol{\Delta} \\ &= (\boldsymbol{v}_{2n-2}, \boldsymbol{v}_{2n-1}, \boldsymbol{v}_{2n})\boldsymbol{g}, \end{aligned} \tag{36}$$

[11] Faster asymptotic times can be achieved on matrix inversion: $O(m^{2.807})$ using Strassen's algorithm (Strassen, 1969) and $O(m^{2.376})$ using the Coppersmith-Winograd algorithm (Coppersmith and Winograd, 1990). However, these algorithms are mainly useful for proving theoretical time bounds.

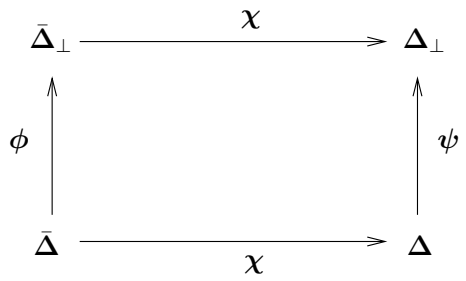


**Figure 3**: From contact displacements to pure deformation.

by the definition of $\boldsymbol{g}$. This is easy from (32) for we have

$$\begin{aligned}
\boldsymbol{\chi}(B\boldsymbol{g}) &= V \begin{pmatrix} \bar{\boldsymbol{v}}_1^T/C\lambda_1 \\ \vdots \\ \bar{\boldsymbol{v}}_{2n-3}^T C/\lambda_{2n-3} \\ E^T \end{pmatrix} B\boldsymbol{g} \\
&= V \begin{pmatrix} \bar{\boldsymbol{v}}_1^T CB/\lambda_1 \\ \vdots \\ \bar{\boldsymbol{v}}_{2n-3}^T CB/\lambda_{2n-3} \\ E^T B \end{pmatrix} \boldsymbol{g} \\
&= V \begin{pmatrix} \mathbf{0} \\ I_3 \end{pmatrix} \boldsymbol{g}. \qquad (37)
\end{aligned}$$

The last step follows from (30), more specifically, from $B^T C = 0$, which implies $CB = 0$, and $B^T E = I_3$, which implies $E^T B = I_3$. Equation (37) clearly establishes (36). □

Multiplication with $AC$ strips off the component of the contact displacement $\bar{\boldsymbol{\Delta}}$ that would yield a rigid body movement, leading to the same pure deformation vector that would be obtained from the displacement vector $\boldsymbol{\Delta}$ resulting from $\bar{\boldsymbol{\Delta}}$. From the arbitrariness of $\bar{\boldsymbol{\Delta}}$ as a vector in $\mathbb{R}^{2m}$, we infer that $\mathrm{col}(AC) = \chi(\mathbb{R}^{2m})$ consists of all pure contact displacement vectors.

Denote by $\bar{\boldsymbol{\Delta}}_\perp = AC\bar{\boldsymbol{\Delta}}$ and let $\boldsymbol{\phi} : \bar{\boldsymbol{\Delta}} \mapsto \bar{\boldsymbol{\Delta}}_\perp$ be this linear mapping. Similarly, let $\boldsymbol{\psi} : \boldsymbol{\Delta} \mapsto \boldsymbol{\Delta}_\perp$ be the linear mapping defined by (17). The relationships among the contact displacements $\bar{\boldsymbol{\Delta}}$, $\bar{\boldsymbol{\Delta}}_\perp$ and their resulting displacement vectors $\boldsymbol{\Delta}$, $\boldsymbol{\Delta}_\perp$ are illustrated in Figure 3. Arithmetically, computation of $\boldsymbol{\phi}$ consists of $4m^2$ multiplications and $2m(2m-1)$ additions once $AC$ has been precomputed, while that of $\boldsymbol{\psi}$ consists of $12n$ multiplications, $10n-3$ additions, and $2n$ subtractions. Since it is often the case that $m \ll \sqrt{n}$, obtaining $\boldsymbol{\Delta}_\perp$ via the path $\bar{\boldsymbol{\Delta}} \to \bar{\boldsymbol{\Delta}}_\perp \to \boldsymbol{\Delta}_\perp$ is more efficient than via $\bar{\boldsymbol{\Delta}} \to \boldsymbol{\Delta} \to \boldsymbol{\Delta}_\perp$. Thus, if we desire a pure deformation via contact, we can simply modify the specified contact displacements via a multiplication with $AC$.

By the definition in Section 2.4, a pure contact displacement $\bar{\boldsymbol{\Delta}}$ constitutes a pure squeeze if every nodal displacement $\boldsymbol{\delta}_{i_k}$ is inward.

### 3.5 Stable Contact Displacement

When the rotation due to a deformation is very small, less emphasis is placed on yielding a pure deformation vector through contact. A *stable* contact displacement $\bar{\boldsymbol{\Delta}}$ yields a local minimum of the potential energy

among all contact displacements of the same magnitude. Without loss of generality, we consider all unit displacements $\bar{\mathbf{\Delta}} = (\boldsymbol{\delta}_{i_1}, \ldots, \boldsymbol{\delta}_{i_m})^T$. Minimizing the potential energy $\Pi$ on the unit hypersphere $\|\bar{\mathbf{\Delta}}\| = 1$ in $\mathbb{R}^{2m}$ is equivalent to maximizing the strain energy $U = \frac{1}{2}\bar{\mathbf{\Delta}}^T C \bar{\mathbf{\Delta}}$. At the maximizing $\bar{\mathbf{\Delta}}$, any deviation on the unit hypersphere would decrease the strain energy. Generally, any deviation in the neighborhood of the maximizing $\bar{\mathbf{\Delta}}$ in $\mathbb{R}^{2m}$ is unstable unless it is along the direction of $\bar{\mathbf{\Delta}}$, in which case, it becomes another stable contact displacement.

The component of $\bar{\mathbf{\Delta}}$ that is in $\mathrm{null}(C)$ has no effect on the strain energy. Hence we need only consider a unit $\bar{\mathbf{\Delta}}$ such that $\bar{\mathbf{\Delta}} \perp \mathrm{null}(C)$, which is equivalent to $\bar{\mathbf{\Delta}} \in \mathrm{row}(C) = \mathrm{col}(C)$, given the symmetry of $C$. For optimization we use the method by Horn (1987). Let $\lambda_1, \lambda_2, \ldots, \lambda_{2m-3}$ be the eigenvalues of $C$ such that $\lambda_1 \geq \lambda_2 \geq \cdots \geq \lambda_{2m-3} > 0$. Let $\hat{\boldsymbol{u}}_1, \hat{\boldsymbol{u}}_2, \ldots, \hat{\boldsymbol{u}}_{2m-3}$ be the corresponding orthogonal unit eigenvectors. Each $\hat{\boldsymbol{u}}_i$, $1 \leq i \leq 2m-3$, results in a force vector $\bar{\boldsymbol{F}} = \lambda_i \hat{\boldsymbol{u}}_i$ that is collinear with $\hat{\boldsymbol{u}}_i$. Decompose $\bar{\mathbf{\Delta}}$ in terms of the eigenvectors

$$\bar{\mathbf{\Delta}} = \alpha_1 \hat{\boldsymbol{u}}_1 + \cdots + \alpha_{2m-3} \hat{\boldsymbol{u}}_{2m-3}. \tag{38}$$

It follows from (33) that

$$U = \frac{1}{2}(\lambda_1 \alpha_1^2 + \cdots + \lambda_{2m-3} \alpha_{2m-3}^2). \tag{39}$$

The potential energy has the minimum value $\frac{1}{2}\lambda_1$ when $\bar{\mathbf{\Delta}} = \pm \hat{\boldsymbol{u}}_1$.[12]

**Theorem 9** *The strain energy $U$ due to unit contact displacement $\bar{\mathbf{\Delta}}$ has no local maximum other than the absolute maximum.*

**Proof** By contradiction. Suppose a local minimum is achieved at some unit eigenvector $\hat{\boldsymbol{u}}_k$ such that $\lambda_k < \lambda_1$. Show that $U$ can be increased locally on the unit hypersphere $\|\bar{\mathbf{\Delta}}\| = 1$. Details omitted. □

Under the above theorem, the only stable contact displacements are in the subspace spanned by $\hat{\boldsymbol{u}}_1, \ldots, \hat{\boldsymbol{u}}_l$, where $l \geq 1$ and $\lambda_1 = \cdots = \lambda_l > \lambda_{l+1}$. Such a contact displacement is a stable squeeze by the definition in Section 2.4 if every specified nodal displacement is inward.

# 4 Foundation of Two-Point Squeezing

A human being is quite adept at grasping soft objects by squeezing them with two fingers. This section examines the reason behind this manipulation skill under the point contact model, paving the way for a full two-finger grasp strategy to be introduced in Section 5. Let $\boldsymbol{p}_i$ and $\boldsymbol{p}_j$ be the only two contact nodes on the deformable object. Define the unit contact displacement vector

$$\hat{\boldsymbol{u}} = \begin{pmatrix} \boldsymbol{\delta}_i \\ \boldsymbol{\delta}_j \end{pmatrix} = \frac{1}{\sqrt{2}\|\boldsymbol{p}_i - \boldsymbol{p}_j\|} \begin{pmatrix} \boldsymbol{p}_j - \boldsymbol{p}_i \\ \boldsymbol{p}_i - \boldsymbol{p}_j \end{pmatrix}. \tag{40}$$

It specifies the movements of the two nodes toward each other.

[12] Alternatively, we can maximize the strain energy $U$ under the constraint $\frac{1}{2}(1 - \bar{\mathbf{\Delta}}^T \bar{\mathbf{\Delta}}) = 0$ using a Lagrange multiplier $\lambda$. This reduces to an unconstrained problem of maximizing the Lagrangian $L = U + \lambda \cdot \frac{1}{2}(1 - \bar{\mathbf{\Delta}}^T \bar{\mathbf{\Delta}})$. The first order necessary condition yields $\boldsymbol{F} = C\bar{\mathbf{\Delta}} = \lambda \bar{\mathbf{\Delta}}$, which states that $\lambda$ is an eigenvalue and $\bar{\mathbf{\Delta}}$ the corresponding eigenvector, i.e., one of $\hat{\boldsymbol{u}}_i$, $1 \leq i \leq 2m-3$.

**Theorem 10** *In the case of only two contact nodes $\boldsymbol{p}_i$ and $\boldsymbol{p}_j$, the vector $\hat{\boldsymbol{u}}$ is orthogonal to* $\mathrm{null}(C)$. *Moreover,*

$$C = \frac{1}{\hat{\boldsymbol{u}}^T A \hat{\boldsymbol{u}}} \hat{\boldsymbol{u}} \hat{\boldsymbol{u}}^T. \tag{41}$$

**Proof** By (34), $\mathrm{null}(C)$ is spanned by $\bar{\boldsymbol{w}}_x = (1,0,1,0)^T$, $\bar{\boldsymbol{w}}_y = (0,1,0,1)^T$, and $\bar{\boldsymbol{w}}_r = (-y_i, x_i, -y_j, x_j)^T$. It is straightforward to verity that the vector

$$\boldsymbol{\xi} = \begin{pmatrix} \boldsymbol{p}_j - \boldsymbol{p}_i \\ \boldsymbol{p}_i - \boldsymbol{p}_j \end{pmatrix}$$

is orthogonal to $\bar{\boldsymbol{w}}_x$, $\bar{\boldsymbol{w}}_y$, and $\bar{\boldsymbol{w}}_r$. Thus, $\hat{\boldsymbol{u}} = \boldsymbol{\xi}/\|\boldsymbol{\xi}\| \perp \mathrm{null}(C)$.

Because $\mathrm{null}(C)$ has rank 3, the $4 \times 4$ matrix $C$ must have a one-dimensional row space (and thus a one-dimensional column space due to symmetry). Therefore, the four columns of $C$ must be collinear with $\hat{\boldsymbol{u}}$. We write $C = \hat{\boldsymbol{u}}\boldsymbol{c}^T$, and perform the following steps of reasoning:

$$\begin{aligned} C = C^T \quad &\Rightarrow \quad \hat{\boldsymbol{u}}\boldsymbol{c}^T = \boldsymbol{c}\hat{\boldsymbol{u}}^T \\ &\Rightarrow \quad \hat{\boldsymbol{u}}(\boldsymbol{c}^T\hat{\boldsymbol{u}}) = \boldsymbol{c}(\hat{\boldsymbol{u}}^T\hat{\boldsymbol{u}}) = \boldsymbol{c} \qquad \text{(right multiplication with } \hat{\boldsymbol{u}}) \\ &\Rightarrow \quad \boldsymbol{c} = \lambda\hat{\boldsymbol{u}}, \end{aligned}$$

where $\lambda = \boldsymbol{c}^T\hat{\boldsymbol{u}}$. This establishes

$$C = \lambda \hat{\boldsymbol{u}}\hat{\boldsymbol{u}}^T. \tag{42}$$

Meanwhile, from (30) we have

$$\begin{aligned} AC + BE^T = I_4 \quad &\Rightarrow \quad A(\lambda\hat{\boldsymbol{u}}\hat{\boldsymbol{u}}^T) + BE^T = I_4 && \text{(substitution of (42))} \\ &\Rightarrow \quad \lambda A\hat{\boldsymbol{u}} + B(E^T\hat{\boldsymbol{u}}) = \hat{\boldsymbol{u}} && \text{(right multiplications with } \hat{\boldsymbol{u}}) \\ &\Rightarrow \quad \lambda\hat{\boldsymbol{u}}^T A\hat{\boldsymbol{u}} + (\hat{\boldsymbol{u}}^T B)(E^T\hat{\boldsymbol{u}}) = \hat{\boldsymbol{u}}^T\hat{\boldsymbol{u}} && \text{(left multiplications with } \hat{\boldsymbol{u}}^T) \\ &\Rightarrow \quad \lambda\hat{\boldsymbol{u}}^T A\hat{\boldsymbol{u}} = 1. && \text{(since } \hat{\boldsymbol{u}} \perp \mathrm{null}(C) = \mathrm{col}(B)) \end{aligned}$$

The last equation implies $\hat{\boldsymbol{u}}^T A\hat{\boldsymbol{u}} \neq 0$ and $\lambda = 1/(\hat{\boldsymbol{u}}^T A\hat{\boldsymbol{u}})$. Equation (41) then follows from a substitution for $\lambda$ into (42). □

Following the theorem, $\mathrm{col}(C)$ has only one dimension. Therefore, $\hat{\boldsymbol{u}}$ maximizes the strain energy $U$, and is a stable squeeze by the definition in Section 2.4, provided that it corresponds to inward displacements of $\boldsymbol{p}_i$ and $\boldsymbol{p}_j$.[13] Any squeeze specified by $\boldsymbol{\Delta} = \rho\hat{\boldsymbol{u}}$, $\rho > 0$ is a stable squeeze once $\hat{\boldsymbol{u}}$ is. Via a substitution of (41) into (33), we rewrite the strain energy as

$$\begin{aligned} U_s &= \frac{1}{2}\rho^2 \hat{\boldsymbol{u}}^T C \hat{\boldsymbol{u}} \\ &= \frac{1}{2}\rho^2 \hat{\boldsymbol{u}}^T \left( \frac{1}{\hat{\boldsymbol{u}}^T A\hat{\boldsymbol{u}}} \hat{\boldsymbol{u}}\hat{\boldsymbol{u}}^T \right) \hat{\boldsymbol{u}} \\ &= \frac{\rho^2}{2\hat{\boldsymbol{u}}^T A\hat{\boldsymbol{u}}}. \end{aligned} \tag{43}$$

Similarly, the nodal contact forces are $\bar{\boldsymbol{F}} = \rho\hat{\boldsymbol{u}}/(\hat{\boldsymbol{u}}^T A\hat{\boldsymbol{u}})$ from (31).

[13] If it corresponds to outward displacements of both points, then $-\hat{\boldsymbol{u}}$ is a stable squeeze. If it is neither case, then a stable squeeze does not exist at the two points.

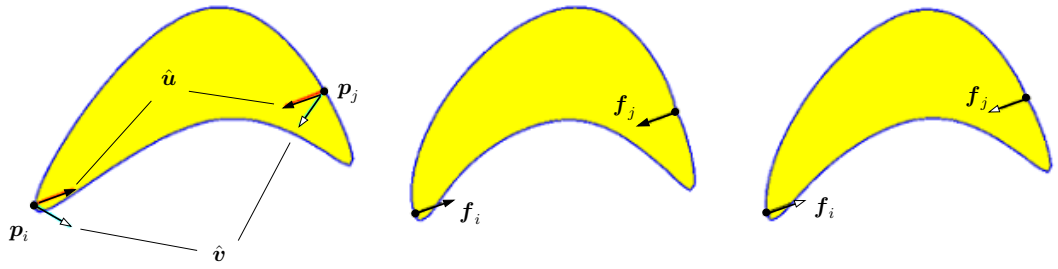


**Figure 4**: Comparison between unit stable and pure squeezes. (a) Original shape from Figure 2 shown with a stable squeeze $\hat{\boldsymbol{u}} = (0.65923,\ 0.25577, -0.65923, -0.25577)^T$ and a pure squeeze $\hat{\boldsymbol{v}} = (0.79644, -0.49167, -0.20702, -0.28477)^T$. (b) Deformed shape under $\hat{\boldsymbol{u}}$ with resulting contact forces $\boldsymbol{f}_i = (0.90772, 0.35218)^T$ and $\boldsymbol{f}_j = (-0.90772, -0.35218)^T$. (c) Deformed shape under $\hat{\boldsymbol{v}}$ with $\boldsymbol{f}_i = (0.55243, 0.21433)^T$ and $\boldsymbol{f}_j = (-0.55243, -0.21433)^T$.

From Section 3.4, a contact displacement from the set $\mathrm{col}(AC)$ causes pure deformation on the object with no rigid body motion. It is a pure squeeze following the definition in Section 2.4, provided that the displacements of $\boldsymbol{p}_i$ and $\boldsymbol{p}_j$ are inward. Since $AC = A\hat{\boldsymbol{u}}\hat{\boldsymbol{u}}^T/(\hat{\boldsymbol{u}}^T A\hat{\boldsymbol{u}})$ following Theorem 10, we infer that $\mathrm{col}(AC)$ is spanned by $A\hat{\boldsymbol{u}}$. Let

$$\hat{\boldsymbol{v}} = A\hat{\boldsymbol{u}}/\|A\hat{\boldsymbol{u}}\| = A\begin{pmatrix}\boldsymbol{p}_j - \boldsymbol{p}_i \\ \boldsymbol{p}_i - \boldsymbol{p}_j\end{pmatrix} \Bigg/ \left\| A\begin{pmatrix}\boldsymbol{p}_j - \boldsymbol{p}_i \\ \boldsymbol{p}_i - \boldsymbol{p}_j\end{pmatrix} \right\|. \tag{44}$$

A pure squeeze specified by $\rho\hat{\boldsymbol{v}}$, $\rho > 0$ yields the strain energy $U_p = \rho^2 \hat{\boldsymbol{u}}^T A\hat{\boldsymbol{u}}/(2\hat{\boldsymbol{u}}^T AA\hat{\boldsymbol{u}})$ and contact forces $\bar{\boldsymbol{F}} = \rho\hat{\boldsymbol{u}}/\|A\hat{\boldsymbol{u}}\|$.

While a stable squeeze makes sure that the movements of the two fingers do not contain any rigid body motion, a pure squeeze makes sure that the object deforms with no rigid body motion component. Figure 4 compares the effects of the unit stable squeeze $\hat{\boldsymbol{u}}$ and the unit pure squeeze $\hat{\boldsymbol{v}}$ on the object in Figure 2 with the same contact nodes $\boldsymbol{p}_i$ and $\boldsymbol{p}_j$. For clarity, all (meshed) solid objects from now on will be drawn non-meshed. While under $\hat{\boldsymbol{u}}$ the fingers drive the two contact points toward each other, under $\hat{\boldsymbol{v}}$ they bend the object to prevent any Euclidean motion, in a 'smart' way by exerting smaller contact forces.

We refer to $\rho$ in a squeeze $\rho\hat{\boldsymbol{u}}$ or $\rho\hat{\boldsymbol{v}}$ as the *squeeze depth*. This is different from the relative distance by which one finger moves toward the other during the squeeze. Such relative distance is $\sqrt{2}\rho$ for a stable squeeze, and $\rho\sqrt{\|\boldsymbol{v}_i - \boldsymbol{v}_j\|^2}$, where $\hat{\boldsymbol{v}} = (\boldsymbol{v}_i^T, \boldsymbol{v}_j^T)^T$, for a pure squeeze.

Translating two fingers $\mathcal{F}_1$ and $\mathcal{F}_2$ by $\boldsymbol{\delta}_i$ and $\boldsymbol{\delta}_j$, respectively, is equivalent to fixing one finger, say $\mathcal{F}_1$, while translating $\mathcal{F}_2$ by $\boldsymbol{\delta}_j - \boldsymbol{\delta}_i$. The two resulting configurations are identical except for a translation by $\boldsymbol{\delta}_i$. For this reason, we call a squeeze stable (respectively, pure) if it is equivalent to $\rho\hat{\boldsymbol{u}}$ (respectively, $\rho\hat{\boldsymbol{v}}$) up to translation and rotation.

## 5 Squeeze Grasping with Rounded Fingers and Contact Mode Analysis

Two fingers achieve a *squeeze grasp* of a deformable object by translating themselves to squeeze the object. The object caves in under a squeeze. If the object is solid and the fingers are pointed ones, this would create tangential discontinuities (and piercing effects), and in theory, infinite displacements at the contact

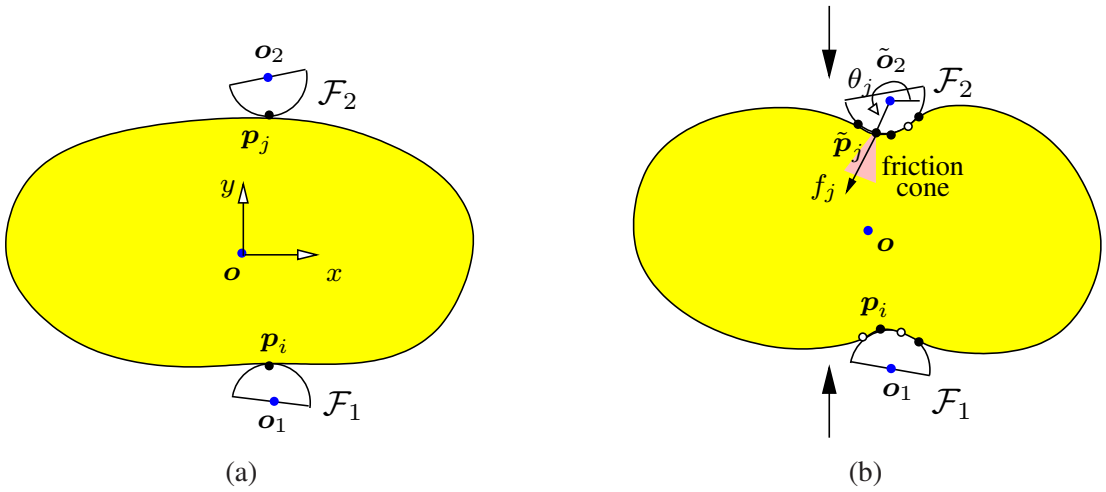


**Figure 5**: Object (a) before and (b) during a squeeze grasp. Solid dots represent the sticking contact nodes at the moment, while hollow dots represent the sliding contact nodes.

points.[14] In this section, we investigate squeeze grasping of solid objects with frictional contacts. Curved fingertips are assumed for practicality. They make area contacts with an object being grasped. Point fingers are appropriate for grasping hollow elastic objects where contact areas are small. Their treatment will be deferred to Section 7.

For the clarity of analysis, the two grasping fingers $\mathcal{F}_1$ and $\mathcal{F}_2$ have identical semicircular tips with radius $r$. They are initially placed on the object at its boundary nodal points, say, $\boldsymbol{p}_i$ and $\boldsymbol{p}_j$, respectively, as shown in Figure 5(a). Denote the placement by $\mathcal{G}(\boldsymbol{p}_i, \boldsymbol{p}_j)$. We assume that during the grasp the object will not make contact with either finger outside its semicircular tip.

As before, a frame is placed at the centroid $\boldsymbol{o}$ of the object. The orientation of a finger is irrelevant due to rotational symmetry of its tip. The centers $\boldsymbol{o}_1$ and $\boldsymbol{o}_2$ of the two fingertips are located on the outward normals at $\boldsymbol{p}_i$ and $\boldsymbol{p}_j$, respectively.

For squeezing to be possible, the object must be initially restrained from any rigid body displacement by $\mathcal{F}_1$ and $\mathcal{F}_2$ under contact friction. This requires the finger placement $\mathcal{G}(\boldsymbol{p}_i, \boldsymbol{p}_j)$ to be force closure were the object rigid. By the result of Nguyen (1988), the line segment $\overline{\boldsymbol{p}_i \boldsymbol{p}_j}$ must lie within the contact friction cones at $\boldsymbol{p}_i$ and $\boldsymbol{p}_j$. A finger placement $\mathcal{G}(\boldsymbol{p}_i, \boldsymbol{p}_j)$ violating this constraint can be immediately rejected.

As $\mathcal{F}_1$ and $\mathcal{F}_2$ squeeze the object, their contacts evolve from $\boldsymbol{p}_i$ and $\boldsymbol{p}_j$ into segments. A node inside such a segment may change its contact mode between sticking and sliding as the squeeze proceeds. Figure 5(b) illustrates a hypothetical configuration at an instant during the squeeze. The two contact segments are each represented by a sequence of contact nodes.

## 5.1 Termination Criteria

The squeeze continues until one of the following three situations arises:

(i) Either $\mathcal{F}_1$ or $\mathcal{F}_2$ starts to slip at its contact;

(ii) The strain at some node exceeds the value $\epsilon^*$ that corresponds to the material's proportional limit;

[14] In Flamant's problem (Lurie 2005, pp. 570–575), in the two-dimensional space a concentrated normal force acting on a half-plane can create infinite displacements at both a location at infinity and one that approaches the point of force application.

(iii) The object can be picked up against its weight vertically from the plane (if this is the goal).

The maximum squeeze depth $\rho^*$ should be the smallest value at which one of the above situations occurs. The grasp is a success if the first two situations do not occur before a specified squeeze depth is reached or when the third situation occurs. Below we take a closer look at the three situations.

A finger slips on the object if all of its contact nodes are sliding in the same direction. The contact mode of a node indeed represents the contact status of a small neighborhood of the node on the boundary. If two adjacent nodes are sliding in opposite directions, then some point between them must be sticking. In such a case, the finger still sticks.

The proportional limit (Crandall et al., 1978, p. 270) is the greatest stress for which the stress is still proportional to the strain, that is, Hooke's law (2) still holds. This limit is $E\epsilon^*$ for some strain $\epsilon^* > 0$. We transplant the maximum principal strain theory (i.e., the St. Venant theory) (Negi, 2008, p. 196) to assume that linear elasticity holds as long as

$$|\epsilon_x| \leq \epsilon^* \qquad \text{and} \qquad |\epsilon_y| \leq \epsilon^*. \tag{45}$$

Finally, to pick up the object from the horizontal plane, the vertical frictional forces generated by the two fingers at their contacts must balance the object's weight $w$. Let $\mathbb{I}$ be the set of indices of the nodes in contact with the finger $\mathcal{F}_1$, and $\mathbb{J}$ the set of indices of those in contact with the finger $\mathcal{F}_2$. Denote by $\boldsymbol{n}_k$ and $\boldsymbol{t}_k$ the unit normal and tangent at a contact node $\boldsymbol{p}_k$, $k \in \mathbb{I} \cup \mathbb{J}$, on the deformed shape. Under Coulomb's friction law, the vertical frictional force at $\boldsymbol{p}_k$ is of magnitude at most $c_k = \sqrt{\mu^2(\boldsymbol{f}_k \cdot \boldsymbol{n}_k)^2 - (\boldsymbol{f}_k \cdot \boldsymbol{t}_k)^2}$, where $\mu$ is the coefficient of friction. Then the object can be picked up if both $\sum_{k\in\mathbb{I}} c_k$ and $\sum_{l\in\mathbb{J}} c_l$ exceed $\frac{w}{2\mu}$ (assume that torque balance can be achieved by friction as well).

If a pickup is not the objective and no squeeze depth is specified, the squeeze may stop before slip happens or the strain exceeds $\epsilon^*$ at some node.

## 5.2 Contact Configuration

During a squeeze, some boundary nodal points may come into contact with the fingertips, as illustrated in Figure 5(b), while others may break contact with them. A node in contact may be sticking to a fingertip or it may be sliding on it. The *contact configuration* at a squeeze depth $\rho$ describes which nodal points are in contact, and among them, which are sticking and which are sliding.

Knowing a contact configuration is critical because it yields some position and force constraints that will be needed by FEM to compute the deformed shape for the current squeeze depth. This will in turn allow us to track the change in the contact configuration as the squeeze continues.

A squeeze is represented by some displacement $\rho\hat{\boldsymbol{u}}$ or $\rho\hat{\boldsymbol{v}}$, where $\hat{\boldsymbol{u}}$ or $\hat{\boldsymbol{v}}$ is calculated from the initial contact points according to (40) or (44). The magnitude $\rho$ will be sequenced into $\rho_0 = 0 < \rho_1 < \cdots$ such that at $\rho = \rho_l$ some event happens to trigger a change in the contact configuration. Based on the contact configuration at $\rho_l$, we evaluate the changes in the contact forces $\bar{\boldsymbol{F}}$ and the displacements of all boundary nodes using the FEM for $\rho > \rho_l$, and predict the squeeze depth $\rho_{l+1}$ at which the next event will happen.

At $\rho_l$, the following two index sets are maintained to record the current contact configuration:

$$\begin{aligned} \mathbb{T} &= \{k \mid \text{the node } \boldsymbol{p}_k \text{ sticks on a finger}\}; \\ \mathbb{P} &= \{k \mid \text{the node } \boldsymbol{p}_k \text{ slides on a finger}\}. \end{aligned}$$

They are referred to as the *contact index sets*. Now, increase $\rho$ by $\xi > 0$. The sets $\mathbb{T}$ and $\mathbb{P}$ will not change as $\rho$ varies within $[\rho_l, \rho_l + \xi)$ for small enough $\xi$.

For $k \in \mathbb{T} \cup \mathbb{P}$, denote by $\theta_k$ the polar angle of the node $\boldsymbol{p}_k$ with respect to the center of the fingertip that it is in contact with. See Figure 5(b) for an illustration over $\boldsymbol{p}_j$. Denote by $\boldsymbol{\delta}_k^{(l)}, \boldsymbol{f}_k^{(l)}$ and $\theta_k^{(l)}$ the values of $\boldsymbol{\delta}_k, \boldsymbol{f}_k$, and $\theta_k$, respectively, when $\rho = \rho_l$. Write the 4-tuple $\hat{\boldsymbol{u}}$ (or $\hat{\boldsymbol{v}}$) as $(\boldsymbol{t}_1^T, \boldsymbol{t}_2^T)^T$, where $\boldsymbol{t}_i$, $i = 1, 2$, is the translation of $\mathcal{F}_i$. The change $\boldsymbol{\delta}_k'$ in $\boldsymbol{\delta}_k$ at $\rho = \rho_l + \xi$ from $\rho_l$ is then

$$\boldsymbol{\delta}_k' = \xi \boldsymbol{\sigma}_k + r \begin{pmatrix} \cos\theta_k - \cos\theta_k^{(l)} \\ \sin\theta_k - \sin\theta_k^{(l)} \end{pmatrix}, \tag{46}$$

where $\boldsymbol{\sigma}_k = \boldsymbol{t}_1$ or $\boldsymbol{t}_2$ depending on whether $\boldsymbol{p}_k$ is in contact with $\mathcal{F}_1$ or $\mathcal{F}_2$.

A node $\boldsymbol{p}_k$ in sticking contact imposes a position constraint on deformation such that $\theta_k = \theta_k^{(l)}$. If $\boldsymbol{p}_k$ slips, then the contact force $\boldsymbol{f}_k = \boldsymbol{f}_k^{(l)} + \boldsymbol{f}_k'$ must stay on one edge of the friction cone at $\boldsymbol{p}_k$ as the node moves. This imposes a force constraint,

$$\left(\boldsymbol{f}_k^{(l)} + \boldsymbol{f}_k'\right) \times \begin{pmatrix} \cos(\theta_k \pm \phi) \\ \sin(\theta_k \pm \phi) \end{pmatrix} = 0, \tag{47}$$

where $\phi = \tan^{-1}\mu$ with $\mu$ being the coefficient of contact friction, and the sign '$+$' or '$-$' can be determined either from the previous step or using hypothesis-and-test.

Denote by $C^{(l)}$ the value of the reduced stiffness matrix $C$ that is computed based on the current contact index set $\mathbb{T} \cup \mathbb{P}$. We gather all $\boldsymbol{\delta}_k'$, $k \in \mathbb{T} \cup \mathbb{P}$, into a vector $\bar{\boldsymbol{\Delta}}'$. Due to its linearity, the equation $\bar{\boldsymbol{F}} = C\bar{\boldsymbol{\Delta}}$ as part of (31) implies the change in $\bar{\boldsymbol{F}}$ to be $\bar{\boldsymbol{F}}' = C^{(l)}\bar{\boldsymbol{\Delta}}'$. Substitute the expression for $\boldsymbol{f}_t'$, $t \in \mathbb{P}$, into (47). This yields an equation linear in $\xi$ and quadratic in $\cos\theta_t$ and $\sin\theta_t$, for every node $\boldsymbol{p}_t$, $t \in \mathbb{P}$. There are a total of $|\mathbb{P}|$ such equations that form a system $S$ in the same number of variables $\theta_t$. Given a value of $\xi$, we can solve for these $\theta_t$s. Since $\xi$ is small, Newton's method has fast convergence using the initial values $\theta_t^{(l)}$. Hence $\boldsymbol{\Delta}$ and $\bar{\boldsymbol{F}}$ are updated.

With $\theta_k$ known for every node $\boldsymbol{p}_k$ in sliding contact, we can also determine the derivative $d\theta_k/d\xi$, which will be used in checking whether the node has switched from slip to stick. Differentiate both sides of every equation in the system $S$ with respect to $\xi$. This yields a new linear system of $|\mathbb{P}|$ equations in $|\mathbb{P}|$ derivatives $d\theta_t/d\xi$, $t \in \mathbb{P}$. Simply solve the system.

### 5.3 Contact Event Detection

We let $\xi$ increase until an event occurs to trigger a change in one or both of the contact index sets $\mathbb{T}$ and $\mathbb{P}$. There are four types of event: a node comes into contact with a finger (Event A); contact breaks at a node (Event B); contact at a node switches from stick to slip (Event C); and contact at a node switches from slip to stick (Event D).

*a) Event A: New Contact* A boundary node $\boldsymbol{p}_k$ in its deformed position $\tilde{\boldsymbol{p}}_k$ comes into contact with one of the two fingers. This happens when its distance to the center of the contacting fingertip of $\mathcal{F}_i$ ($i = 1$ or 2) reduces to $r$, or equivalently, when the following condition holds:

$$\left(\tilde{\boldsymbol{p}}_k - \boldsymbol{o}_i^{(l)} - \xi\boldsymbol{t}_i\right) \cdot \left(\tilde{\boldsymbol{p}}_k - \boldsymbol{o}_i^{(l)} - \xi\boldsymbol{t}_i\right) = r^2, \tag{48}$$

where $\boldsymbol{o}_i^{(l)}$ is the position of the fingertip's center at $\rho = \rho_l$.

To determine the mode of contact for $\boldsymbol{p}_k$, we first hypothesize that it sticks, apply a small extra squeeze, and check if the resulting contact force $\boldsymbol{f}_k$ will stay inside the friction cone. If not, the node slips. Add $k$ to $\mathbb{T}$ or $\mathbb{P}$ accordingly.

*b) Event B: Contact Break* As $\xi$ increases, the force $\boldsymbol{f}_k$ at a node $\boldsymbol{p}_k$ varies inside or on one edge of the inward contact friction cone. When its magnitude reduces to zero, it is about to point into the fingertip. The contact breaks when

$$\|\boldsymbol{f}_k\| = 0. \tag{49}$$

Remove $k$ from either $\mathbb{P}$ or $\mathbb{T}$ that contains it.

*c) Event C: Stick to Slip* When the contact force $\boldsymbol{f}_k$ applied at a sticking node $\boldsymbol{p}_k$ is rotating out of the friction cone as $\rho$ increases, the contact mode switches to slip. The rotation of the force $\boldsymbol{f}_k$ at the moment is indicated by its derivative with respect to $\xi$. We need to check the conditions:

$$\begin{aligned} \boldsymbol{f}_k \times \begin{pmatrix} \cos(\theta_k \mp \phi) \\ \sin(\theta_k \mp \phi) \end{pmatrix} &= 0 \\ \mp \frac{d\boldsymbol{f}_k}{d\xi} \times \begin{pmatrix} \cos(\theta_k \mp \phi) \\ \sin(\theta_k \mp \phi) \end{pmatrix} &> 0 \end{aligned} \tag{50}$$

for reaching the left (sign '$-$') or right ('$+$') edge, respectively. Remove $k$ from $\mathbb{T}$ and add it to $\mathbb{P}$.

*d) Event D: Slip to Stick* As $\xi$ increases, the contact node $\boldsymbol{p}_k$ slides, and its polar angle $\theta_k$ with respect to the corresponding fingertip's center varies. Slip changes to stick when

$$\frac{d\theta_k}{d\xi} = 0. \tag{51}$$

In this case, remove $k$ from $\mathbb{P}$ and add it to $\mathbb{T}$.

If a node $\boldsymbol{p}_k$ sticks throughout the squeeze, then it moves along a straight line segment parallel to the trajectory of its contacting fingertip. If its has slipped, then its trajectory is a sequence of line and curve segments.

Suppose a squeeze has gone through a total of $l$ events. Over the period between the $j$th event and the $(j+1)$-st event, for $0 \leq j \leq l-1$, deformation is governed by the equation

$$K\left(\boldsymbol{\Delta}^{(j+1)} - \boldsymbol{\Delta}^{(j)}\right) = \boldsymbol{F}^{(j+1)} - \boldsymbol{F}^{(j)},$$

subject to specified $\boldsymbol{\delta}_k^{(j+1)} - \boldsymbol{\delta}_k^{(j)}$, $k \in \mathbb{T}^{(j)} \cup \mathbb{P}^{(j)}$, and $\boldsymbol{f}_s^{(j+1)} - \boldsymbol{f}_s^{(j)} = 0$, $s \notin \mathbb{T}^{(j)} \cup \mathbb{P}^{(j)}$. After the $l$th event, deformation is governed by

$$K\left(\boldsymbol{\Delta} - \boldsymbol{\Delta}^{(l)}\right) = \boldsymbol{F} - \boldsymbol{F}^{(l)}.$$

Updates of the four types of event ensure that any non-contact node $\boldsymbol{p}_k$ at a moment has $\boldsymbol{f}_k = 0$. Summing up the above $l+1$ equations, we have

$$K\boldsymbol{\Delta} = \boldsymbol{F}.$$

Suppose we knew the nodes that are in contact after the $l$th event, and their displacements $\bar{\boldsymbol{\Delta}}$. Then we would be able to generate the same final shape and contact configuration in 'one shot' based on (32) as the incremental squeeze would eventually. This is due to the uniqueness of deformation from specified contacts and their displacements, which was established in Section 3.3. Unfortunately, it is impossible to predict the final contacts and their displacements before the squeeze is even performed. The final configuration will be determined during the execution of an event-based algorithm described next in Section 5.4 to grasp the object.

**Algorithm 1** Two-Finger Squeeze

**Input:** initial contacts $\boldsymbol{p}_i$ and $\boldsymbol{p}_j$, squeeze type and depth $\rho^*$

1: $\rho \leftarrow 0$
2: initialize $\mathbb{T}$ and $\mathbb{P}$ by determining if $\boldsymbol{p}_i$ and $\boldsymbol{p}_j$ stick or slip
3: **while** $\rho < \rho^*$ and no finger slips and the proportional limit $\epsilon^*$ is not exceeded at any node **do**
4: $\quad\xi \leftarrow 0$
5: $\quad$compute the reduced stiffness matrix $C$ based on $\mathbb{T} \cup \mathbb{P}$
6: $\quad$**repeat**
7: $\quad\quad\xi \leftarrow \xi + h$
8: $\quad\quad$solve for all $\theta_k$, $k \in \mathbb{P}$, together from $|\mathbb{P}|$ equations (47) using Newton's method with their current values as the initial estimates
9: $\quad\quad$set $\boldsymbol{\delta}'_k$, $\forall\, k \in \mathbb{T} \cup \mathbb{P}$, according to (46)
10: $\quad\quad\bar{\boldsymbol{F}}' \leftarrow C\bar{\boldsymbol{\Delta}}'$
11: $\quad$**until** one of (48)–(51) is true
12: $\quad$**if** event A occurs **then**
13: $\quad\quad$determine the mode of the new contact
14: $\quad$**end if**
15: $\quad$update $\mathbb{P}$ or $\mathbb{T}$ according to the event type
16: $\quad\rho \leftarrow \rho + \xi$
17: **end while**
18: **if** either finger slips **then**
19: $\quad$**return** squeeze failure
20: **end if**

### 5.4 The Squeeze Algorithm

We may perform a squeeze grasp operation for some specified squeeze depth $\rho^*$ iteratively as follows. Start at $\rho = 0$. At step $l$, we hypothesize each of the four events for every current contact node (and its adjacent nodes), and computes the extra squeeze distance $\xi$ for the hypothesized event to happen. Then select the minimum such distance $\xi_{\min}$, and let $\rho_{l+1} = \rho_l + \xi_{\min}$.

Each of the event conditions (48)–(51) involves solving for $\xi$ and the polar angles $\theta_t$ of all nodes $\boldsymbol{p}_t$ in sliding contact from the event condition together with the corresponding $|\mathbb{P}|$ equations. Solution of this system of $|\mathbb{P}| + 1$ nonlinear equations is not easy, and repeatedly doing so can become very time consuming. For these reasons, we resort to a numerical routine. It increments the extra squeeze depth $\xi$ by a small step size $h$ (which allows Newton's method to converge fast in computing $\theta_t$ for $t \in \mathbb{P}$).

Algorithm 1 describes the squeeze grasp strategy. On line 5, the computation of $C$ involves the construction of the matrix $M$ in (27), which takes time $O(mn)$, where $m = |\mathbb{P}| + |\mathbb{T}|$, and the inversion of $M$, which takes time $O(m^3)$. Typically, $m$ is very small and can be regarded as a constant, reducing the execution time of line 5 to $O(n)$.

On line 11, checking whether an event happens becomes testing either an inequality or whether an expression changes sign. For instance, we check the inequality

$$\left(\tilde{\boldsymbol{p}}_k - \boldsymbol{o}_i^{(l)} - \xi\hat{\boldsymbol{t}}\right) \cdot \left(\tilde{\boldsymbol{p}}_k - \boldsymbol{o}_i^{(l)} - \xi\hat{\boldsymbol{t}}\right) \leq r^2.$$

for an occurrence of event A with the node $\boldsymbol{p}_k$. When the condition holds, we use bisection to find the increment in $(0, h]$ that satisfies (48).

Equations (48)–(51) each requires $O(n)$ time to set up, and $O(1)$ time to solve for $\xi$. All events except Event A need only be checked over the contact nodes. The size of $\mathbb{P} \cup \mathbb{T}$ is bounded by $2\pi r$ divided by the average arc length between two adjacent boundary nodes. It is typically very small. Because the squeeze is also small, it often suffices to check Event A on a few nodes in the neighborhoods of the outermost contact nodes. In summary, $O(1)$ nodes are checked for the events at $\rho^{(l)}$ at the time cost of $O(n)$. Consequently, Algorithm 1 takes $O((\rho^*/h)n)$ time overall.

From (46) the change in the displacement of a contact node at each step is not proportional to the squeeze distance $\xi$, neither is the overall displacement of a node during the squeeze grasp. The strain at a node is still a linear expression of $\xi$ but with a constant term. The maximum strain will not be achieved at the same node throughout the squeeze. This implies that we need to update the node with the maximum strain as $\rho$ changes from $\rho_l$ to $\rho_{l+1}$ in case the proportional limit is exceeded.

Nevertheless, most objects have proportional limits that are beyond what the squeeze forces need to generate in order to pick up the objects. For this reason, we will only pay attention to the possibility of finger sliding from now on.

### 5.5 Experiment with Foam Rubber Objects

A $0.1 \times 0.1 \times 0.0254$ square made of foam rubber was grasped by a three-fingered Barrett Hand. The two grasping fingers were mounted with semicircular plastic tips of radius 0.02. We measured Young's modulus $E \approx 5 \times 10^4$ and Poisson's ratio $\nu \approx 0.3$, using the method described in Appendix B. The coefficient of contact friction $\mu$ between a fingertip and the foam rubber was measured to be 0.4.

Table 1 in Section 1 compares an actual grasp configuration to its simulation by Algorithm 1 from Section 5.4. Here, a stable squeeze was carried out such that the two fingers translated toward each other along the line connecting their initial contact points (nodes 110 and 45 on the left and right fingertips, respectively), reducing their distance by $12\%$. Superposition of the deformed mesh from simulation onto the real shape (shown in the central image) is done by a matching algorithm described in Appendix C. The algorithm minimized in the least-squares sense the average error per node (1.3mm for the displayed object) while filtering out the effects due to different coordinate systems used in the simulation and the experiment. The first row of the table shows 12 sticking contact nodes (solid dots), and 2 sliding contact nodes (hollow dots) at the final instant of the squeeze corresponding to the center image.

Note that simulation shows a sliding node (number 113) in the interior of the left contact segment while sticking nodes (numbers 108 and 114) at both ends. This phenomenon is different from incipient slip, observed with a finger sliding on a rigid body, where slip starts in the peripheral region and propagates to the center of the contact. The reason is that on a deformable object, contact points are not rigidly connected to each other like on a rigid object. Each contact node has its own degree of freedom, and its motion is due to local stresses that are not directly influenced by those of other nodes (which are not in its neighborhood).

Figure 6 displays the evolutions of the polar angles of all contact nodes in terms of the relative squeeze depth $\varrho$ (to the original distance between the initial contact nodes 110 and 45). Note that the units in the figure apply only to single trajectories, not to the gaps between them (which are much wider as the nodes had much larger spacings than the distances they slid over). Besides the two initial contact nodes (no. 110 and 45), six other nodes (no. 108, 109, 114; 42, 43, 44) stuck on the fingertips after contact establishments until the end of the squeeze.[15] Nodes 113 and 48 slid on the fingertips from the beginning and continued so until the end of the squeeze. Nodes 111 and 46 started out sliding and switched to sticking eventually.

[15] A node was regarded as sticking if the change in its polar angle is within some tolerance. In the case of node 42, small changes were neglected.

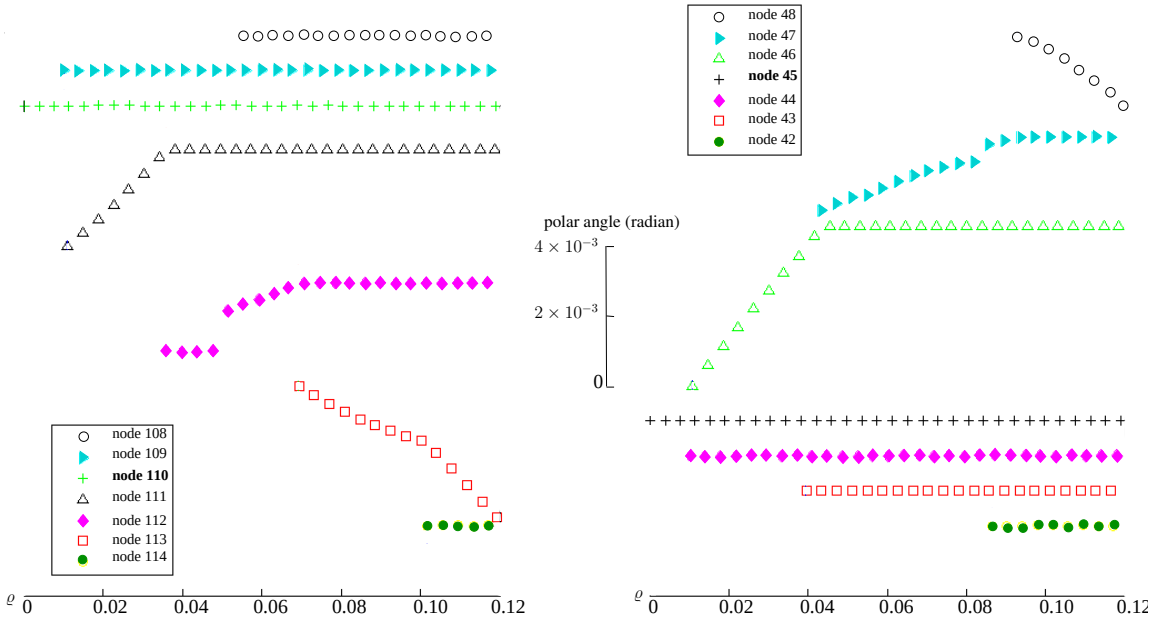


**Figure 6**: Trajectories (in polar angle) of the 14 contact nodes on the left and right fingertips in Table 1.

Nodes 112 and 47 started out sticking, later switched to sliding, and eventually switched back to sticking. Event C happened twice, while Event D four times. It is noted that all sliding distances were within 1% of the gap between two adjacent nodes so the effects were rather small.

Among the four types of event introduced in Section 5, Event A of contact establishment is destined to occur (unless the squeeze depth is very small). They were 12 occurrences during the squeeze in Table 1. Event B of contact breaking is so rare that it was not observed in the experiment. We suspect it to happen often with large rotations which are nonetheless beyond the scope of linear elasticity.

Event C of stick-to-slip transition was widely observed in both simulation and experiment wherever friction was insufficient. Table 2 shows four other grasping instances during which events of this type happened. Each of columns 2–5 displays one object, with yellow and red arrows respectively indicating movements of two points, one on the object and the other on the fingertip. These two points were shown initially in sticking contact (in row 2) and later separated from each other due to sliding (in row 3), as the squeezes continued.

In Figure 7, (a) and (b) show simulation results that correspond to the experiment images in the entries (2, 3) and (3, 3) in Table 2. The blue arrows mark the same node on the object that started out sticking in (a), transitioned into sliding in (b), and switched back to sticking in (c). Shown in (d) is an experiment image that displays the distance of sliding (about five degrees) on the fingertip by the same node identified with arrows in (a)–(c) from the fingertip contact location in (b), pointed at by the red arrow in (d), to the location of the new fingertip contact in (c), pointed at by the yellow arrow in (d).

Event D sometimes happens more often than Event C as observed in the instance of Table 1, where several contact nodes started out sliding and switched to sticking later.

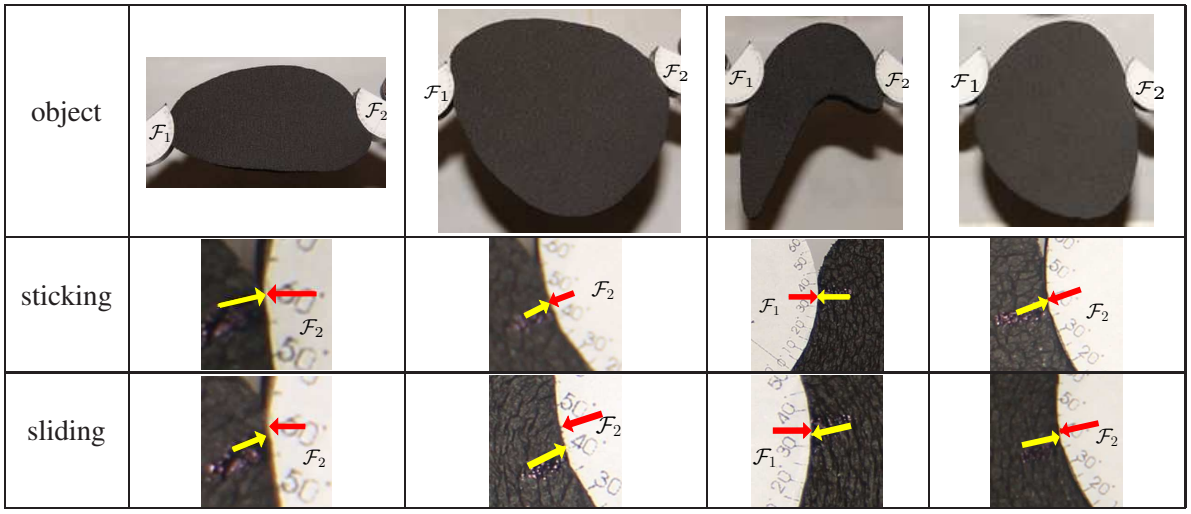


**Table 2**: Occurrences of Event C (stick-to-slip transition) during squeeze grasps of four objects.

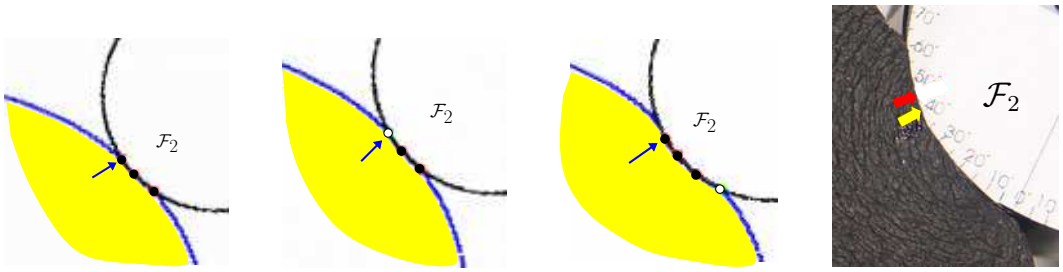


**Figure 7**: Transitions of a contact from (a) stick to (b) slip to (c) slick. Here (a) and (b) are the simulation results over the second object in Table 2 that correspond to its entries (2, 3) and (3, 3), respectively. In (c), the contact has stopped sliding, which is also observed in the experiment in (d).

## 6 Resisting an Adversary Finger

Consider a finger placement $\mathcal{G}(\boldsymbol{p}_i, \boldsymbol{p}_j)$ on the deformable object. Suppose that an adversary finger $\mathcal{A}$ makes contact with the object at $\boldsymbol{p}_k$, and tries to break the grasp via a translation $\boldsymbol{a}$. To resist $\mathcal{A}$, the two grasping fingers $\mathcal{F}_1$ and $\mathcal{F}_2$ translate by $\boldsymbol{d}_1$ and $\boldsymbol{d}_2$, respectively.[16] We would like to find $\boldsymbol{d}_1$ and $\boldsymbol{d}_2$ that result in the minimum total effort by $\mathcal{F}_1$ and $\mathcal{F}_2$ in such resistance. The effort of resistance is best characterized as the total work performed by these two fingers.[17]

The general scenario is depicted in Figure 8, in which the finger contacts have evolved from the nodes $\boldsymbol{p}_i, \boldsymbol{p}_j, \boldsymbol{p}_k$ into segments as $\mathcal{F}_1, \mathcal{F}_2, \mathcal{A}$ translate. Every contact segment is uniquely represented by a sequence of nodes on it[18]. At an instant during the resistance, $\mathcal{F}_1$ makes contact with the set of nodes $\{\boldsymbol{p}_t \mid t \in \mathbb{I}\}$,

[16]The grasping fingers under the placement $\mathcal{G}(\boldsymbol{p}_i, \boldsymbol{p}_j)$ may have applied some initial squeeze $\boldsymbol{d}_1^{(0)}$ and $\boldsymbol{d}_2^{(0)}$ before $\mathcal{A}$ makes contact with the object. In this case, they need to execute extra translations $\boldsymbol{d}_1 - \boldsymbol{d}_1^{(0)}$ and $\boldsymbol{d}_2 - \boldsymbol{d}_2^{(0)}$ to resist $\mathcal{A}$.

[17]We do not want to minimize the potential energy of the system here because its negation (assuming no energy dissipation) — the object's strain energy — can be made as large as we like with large $\boldsymbol{d}_1$ and $\boldsymbol{d}_2$, as long as the stress everywhere does not exceed the material's proportional limit.

[18]under an implicit assumption (consistent with the use of FEM) that a segment always ends at two nodes.

$\mathcal{F}_2$ with $\{\boldsymbol{p}_t \mid t \in \mathbb{J}\}$, and $\mathcal{A}$ with $\{\boldsymbol{p}_t \mid t \in \mathbb{K}\}$. Some nodes (solid dots in the figure) are sticking on the fingertips, while others (hollow dots) are sliding. We can partition the scenario into small periods, within each of which the contact index sets $\mathbb{I}, \mathbb{J}, \mathbb{K}$ do not change.

This optimization problem will be approached in three steps. In Section 6.1, we will look at fixed point contacts (i.e., $|\mathbb{I}| = |\mathbb{J}| = |\mathbb{K}| = 1$ and the three sets do not change) during the resistance. In Section 6.2, we will generalize the result to fixed segment contacts ($|\mathbb{I}|, |\mathbb{J}|, |\mathbb{K}| \geq 1$ and the sets do not vary). Building upon this, in Section 6.3, we will tackle the general situation with varying $\mathbb{I}$, $\mathbb{J}$, $\mathbb{K}$ and changing contact modes at individual nodes during the resistance under Coulomb friction.

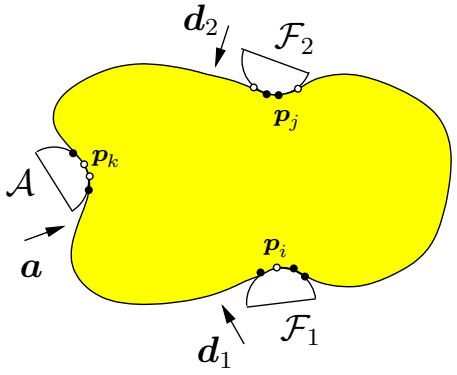


**Figure 8**: Grasp resistance to a translating adversary finger $\mathcal{A}$.

## 6.1 Fixed Point Contacts

The nodes $\boldsymbol{p}_i, \boldsymbol{p}_j$, and $\boldsymbol{p}_k$ will stay as the only contact points with the fingers $\mathcal{F}_1$, $\mathcal{F}_2$, and $\mathcal{A}$, respectively (as if the fingers and the object were glued together). Deformation of the object is due to their displacements

$$\bar{\boldsymbol{\Delta}} = \begin{pmatrix} \boldsymbol{\delta}_i \\ \boldsymbol{\delta}_j \\ \boldsymbol{\delta}_k \end{pmatrix} = \begin{pmatrix} \boldsymbol{d}_1 \\ \boldsymbol{d}_2 \\ \boldsymbol{a} \end{pmatrix}, \tag{52}$$

which results in the nodal forces

$$\bar{\boldsymbol{F}} = \begin{pmatrix} \boldsymbol{f}_i \\ \boldsymbol{f}_j \\ \boldsymbol{f}_k \end{pmatrix}.$$

Following the steps in Sections 3.2–3.3 with $m = 3$ and $i_1 = i, i_2 = j, i_3 = k$, we construct the reduced stiffness matrix $C$ in (29).

The work done by the grasping fingers is derived as follows:

$$\begin{aligned} W_{\mathcal{F}} &= \frac{1}{2}(\boldsymbol{d}_1^T \boldsymbol{f}_i + \boldsymbol{d}_2^T \boldsymbol{f}_j + \boldsymbol{0}^T \boldsymbol{f}_k) \\ &= \frac{1}{2} \begin{pmatrix} \boldsymbol{d}_1 \\ \boldsymbol{d}_2 \\ 0 \end{pmatrix}^T C \begin{pmatrix} \boldsymbol{d}_1 \\ \boldsymbol{d}_2 \\ \boldsymbol{a} \end{pmatrix}. \qquad (\text{since } \bar{\boldsymbol{F}} = C\bar{\boldsymbol{\Delta}}\,) \end{aligned} \tag{53}$$

By the result from Section 3.5, a stable contact displacement must be collinear with the eigenvector $\hat{\boldsymbol{u}}_1$ that corresponds to the largest eigenvalues of $C$. However, due to the arbitrariness of the adversary finger translation $\boldsymbol{a}$, the contact displacement $\bar{\boldsymbol{\Delta}}$ will not satisfy such condition regardless of $\boldsymbol{d}_1$ and $\boldsymbol{d}_2$ unless $\boldsymbol{a}$ is collinear with the vector consisting of the last two entries in $\hat{\boldsymbol{u}}$. This means that $\mathcal{F}_1$, $\mathcal{F}_2$, and $\mathcal{A}$ together almost never form a stable contact displacement.

We need to relax the notion of 'being stable' when it comes to resistance. Since $m = 3$, both $\mathrm{col}(C)$ and $\mathrm{col}(AC)$ have three dimensions following Theorem 7. We consider $(\boldsymbol{d}_1, \boldsymbol{d}_2)$ such that $\bar{\boldsymbol{\Delta}} \in \mathrm{col}(C)$ as a *stable resistance*. Also, we call $(\boldsymbol{d}_1, \boldsymbol{d}_2)$ a *pure resistance* if $\bar{\boldsymbol{\Delta}} \in \mathrm{col}(AC)$.

### 6.1.1 Optimal Stable Resistance

Consider all $(\boldsymbol{d}_1, \boldsymbol{d}_2)$ such that $\bar{\boldsymbol{\Delta}} \in \mathrm{col}(C)$, or equivalently, $\bar{\boldsymbol{\Delta}} \perp \mathrm{col}(B)$, which is spanned by $(1,0,1,0,1,0)^T$, $(0,1,0,1,0,1)^T$, and $(-y_i, x_i, -y_j, x_j, -y_k, x_k)^T$. Equivalently, we require

$$\boldsymbol{d}_1 + \boldsymbol{d}_2 + \boldsymbol{a} = \boldsymbol{0}, \tag{54}$$

$$\boldsymbol{p}_i \times \boldsymbol{d}_1 + \boldsymbol{p}_j \times \boldsymbol{d}_2 + \boldsymbol{p}_k \times \boldsymbol{a} = 0. \tag{55}$$

Let us substitute (54) into (53) for $\boldsymbol{d}_2$, and rewrite $W_{\mathcal{F}}$ as a quadratic form in terms of $\boldsymbol{d}_1$:

$$W_{\mathcal{F}} = \frac{1}{2} \begin{pmatrix} \boldsymbol{d}_1 \\ -\boldsymbol{d}_1 - \boldsymbol{a} \\ 0 \end{pmatrix}^T C \begin{pmatrix} \boldsymbol{d}_1 \\ -\boldsymbol{d}_1 - \boldsymbol{a} \\ \boldsymbol{a} \end{pmatrix} \tag{56}$$

$$= \frac{1}{2} \boldsymbol{d}_1^T H \boldsymbol{d}_1 + \boldsymbol{c}^T \boldsymbol{d}_1 + \omega, \tag{57}$$

where the expressions for $H$, $\boldsymbol{c}$, and $\omega$ are given in Appendix D.

**Theorem 11** *The matrix $H$ is positive semi-definite. Furthermore, $\boldsymbol{d}_1 \in \mathrm{null}(H)$ if and only if*

$$\boldsymbol{p}_k = \frac{1}{2}(\boldsymbol{p}_i + \boldsymbol{p}_j) \qquad \textit{and} \qquad \boldsymbol{d}_1 \cdot (\boldsymbol{p}_i - \boldsymbol{p}_j) = 0. \tag{58}$$

The proof is given in Appendix E. The first condition in the theorem is rarely satisfied because the midpoint of $\boldsymbol{p}_i$ and $\boldsymbol{p}_j$ often lies in the interior of the object, and thus cannot be in contact with the adversary finger.

Denote by $\hat{\boldsymbol{t}}$ the unit vector in the direction of $\boldsymbol{p}_i - \boldsymbol{p}_j$, and $\hat{\boldsymbol{n}}$ the unit vector such that $\hat{\boldsymbol{t}} \cdot \hat{\boldsymbol{n}} = 0$ and $\hat{\boldsymbol{t}} \times \hat{\boldsymbol{n}} = 1$. Write $\boldsymbol{d}_1 = \tau \hat{\boldsymbol{t}} + \eta \hat{\boldsymbol{n}}$. Substitute it and $\boldsymbol{d}_2 = -\tau \hat{\boldsymbol{t}} - \eta \hat{\boldsymbol{n}} - \boldsymbol{a}$, from (54), into (55). A few steps of manipulation leads to

$$\eta = \boldsymbol{d}_1 \cdot \hat{\boldsymbol{n}} = \frac{(\boldsymbol{p}_j - \boldsymbol{p}_k) \times \boldsymbol{a}}{\|\boldsymbol{p}_i - \boldsymbol{p}_j\|}. \tag{59}$$

From the above deduction, we see that $\boldsymbol{d}_1$, determined by $\eta$ and arbitrary $\tau$, and $\boldsymbol{d}_2 = -\boldsymbol{d}_1 - \boldsymbol{a}$ satisfy the conditions (54) and (55) for a stable resistance.

Now, plug $\boldsymbol{d}_1 = \tau \hat{\boldsymbol{t}} + \eta \hat{\boldsymbol{n}}$ into (57). After a few steps, we derive a new form for the work:

$$W_{\mathcal{F}} = \frac{1}{2} b_2 \tau^2 + b_1 \tau + b_0, \tag{60}$$

where $b_0 = \omega + \eta \left( \frac{1}{2} \eta \hat{\boldsymbol{n}}^T H + \boldsymbol{c}^T \right) \hat{\boldsymbol{n}}$, $b_1 = (\eta \hat{\boldsymbol{n}}^T H + \boldsymbol{c}^T) \hat{\boldsymbol{t}}$, and $b_2 = \hat{\boldsymbol{t}}^T H \hat{\boldsymbol{t}}$.

Since $\hat{\boldsymbol{t}} \cdot (\boldsymbol{p}_i - \boldsymbol{p}_j) = \|\boldsymbol{p}_i - \boldsymbol{p}_j\| > 0$, it follows from Theorem 11 that $\hat{\boldsymbol{t}} \notin \mathrm{null}(H)$. The positive semi-definiteness of $H$ implies that $b_2 > 0$. Therefore, $W_{\mathcal{F}}$ in (60) is a parabola with the minimum value $W_{\mathcal{F}}^* = b_0 - \frac{b_1^2}{2b_2}$ achieved at $\tau = -b_1/b_2$. Note that $b_0$ scales with $\|\boldsymbol{a}\|^2$ and $b_1$ scales with $\|\boldsymbol{a}\|$, while $b_2$ is constant. The minimum work $W_{\mathcal{F}}^*$ scales quadratically with $\|\boldsymbol{a}\|$.

We plug $\boldsymbol{a} = \|\boldsymbol{a}\| \hat{\boldsymbol{a}}$, where $\hat{\boldsymbol{a}}$ is a unit vector, first into the expressions (87) and (88) for $\boldsymbol{c}$ and $\omega$ given in Appendix D, and (59) for $\eta$, then the resulting expressions into $b_0$ and $b_1$, and finally into the expressions of $\boldsymbol{d}_1$ and $\boldsymbol{d}_2$. This yields the optimal displacement:

$$\begin{pmatrix} \boldsymbol{d}_1^* \\ \boldsymbol{d}_2^* \end{pmatrix} = \|\boldsymbol{a}\| \begin{pmatrix} \boldsymbol{\psi}_1 \\ \boldsymbol{\psi}_2 \end{pmatrix}, \tag{61}$$

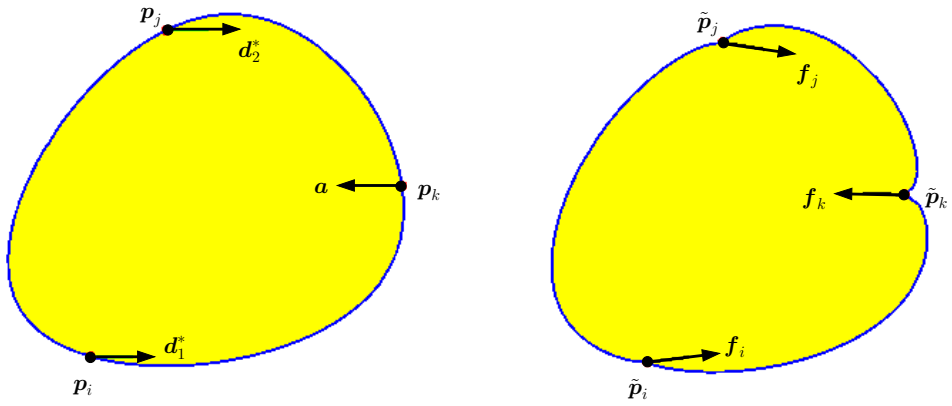


**Figure 9**: A grasp $\mathcal{G}(\boldsymbol{p}_i, \boldsymbol{p}_j)$ resisting an adversary finger at $\boldsymbol{p}_k = (0.05900, 0.00502)^T$ under translation $\boldsymbol{\delta}_k = \boldsymbol{a} = (-0.01, 0)^T$. Here $\boldsymbol{p}_i = (-0.03537, -0.04685)^T$ and $\boldsymbol{p}_j = (-0.01256, 0.05212)^T$. (a) Undeformed shape marked with optimal displacements: $\boldsymbol{d}_1^* = (0.00475, 0.00006)^T$ and $\boldsymbol{d}_2^* = (0.00525, -0.00006)^T$. (b) Deformed shape marked with the corresponding nodal forces: $\boldsymbol{f}_i = (2.5031, 0.3105)^T$, $\boldsymbol{f}_j = (2.8792, -0.4901)^T$, and $\boldsymbol{f}_k = (-5.3823, 0.1796)^T$. Young's modulus $E = 5 \times 10^4$ and Poisson's ratio $\nu = 0.3$ are the same as measured in the experiment in Section 5.5.

where $\boldsymbol{\psi}_1$ and $\boldsymbol{\psi}_2$ are given in Appendix D as (89) and (90), respectively. Under (61), the optimal directions of translation by the grasping fingers $\mathcal{F}_1$ and $\mathcal{F}_2$ are invariant to the amount $\|\boldsymbol{a}\|$ of the adversary finger translation. If $\mathcal{A}$ pushes harder, $\mathcal{F}_1$ and $\mathcal{F}_2$ just need to translate proportionally more along these directions.

Figure 9 shows a resistance scenario. The minimum work is $W_{\mathcal{F}}^* = 0.01031$. The average rotation per node is $\boldsymbol{\Delta} \cdot \boldsymbol{v}_{2n} = 0.0035418$.

When $\boldsymbol{p}_k = \frac{1}{2}(\boldsymbol{p}_i + \boldsymbol{p}_j)$, we can show that $b_1 = \boldsymbol{c}^T \hat{\boldsymbol{t}}$ and $b_0 = \omega$. Since $b_0, b_1, b_2$ are now independent of $\eta = \boldsymbol{d}_1 \cdot \hat{\boldsymbol{n}}$, $W_{\mathcal{F}}$ has the same value over $\tau \hat{\boldsymbol{t}} + \eta \hat{\boldsymbol{n}}$, for all $\eta \in \mathbb{R}$ and a given $\tau$. A continuum of optimal resistances thus exist. We simply let $\eta = 0$ while $\tau = -b_1/b_2$.

### 6.1.2 Optimal Pure Resistance

This section considers minimization of $W_{\mathcal{F}}$ over $(\boldsymbol{d}_1, \boldsymbol{d}_2)$ such that $\bar{\boldsymbol{\Delta}}$ given in (52) lies in $\mathrm{col}(AC)$. Represent $\bar{\boldsymbol{\Delta}} = \tau_1 \hat{\boldsymbol{u}}_1 + \tau_2 \hat{\boldsymbol{u}}_2 + \tau_3 \hat{\boldsymbol{u}}_3$, where $\hat{\boldsymbol{u}}_1, \hat{\boldsymbol{u}}_2, \hat{\boldsymbol{u}}_3$ are the orthogonal unit vectors that span $\mathrm{col}(AC)$. The following needs to hold:

$$\boldsymbol{a} = Q \begin{pmatrix} \tau_1 \\ \tau_2 \\ \tau_3 \end{pmatrix}, \tag{62}$$

where the $2 \times 3$ matrix $Q = (\boldsymbol{0}, I_2)(\hat{\boldsymbol{u}}_1, \hat{\boldsymbol{u}}_2, \hat{\boldsymbol{u}}_3)$. If $Q$ is not of full rank and $\boldsymbol{a}$ is not in its column space $\mathrm{col}(Q) = \mathrm{col}((\boldsymbol{0}, I_2)AC)$, then we infer that $\bar{\boldsymbol{\Delta}} \notin \mathrm{col}(AC)$ and the adversary finger cannot be resisted. If $\mathrm{rank}(Q) = 1$ and $\boldsymbol{a} \in \mathrm{col}(Q)$, we permute the subscripts of $\hat{\boldsymbol{u}}_1, \hat{\boldsymbol{u}}_2, \hat{\boldsymbol{u}}_3$ such that the last two entries in $\hat{\boldsymbol{u}}_1$ are $\tau_1 \boldsymbol{a}$ for some $\tau_1$. Simply let $\tau_2 = \tau_3 = 0$.

Let us focus on the general case that $\mathrm{rank}(Q) = 2$. We can always permute the subscripts of $\hat{\boldsymbol{u}}_1, \hat{\boldsymbol{u}}_2, \hat{\boldsymbol{u}}_3$ to make the matrix $N = (\boldsymbol{0}, I_2)(\hat{\boldsymbol{u}}_2, \hat{\boldsymbol{u}}_3)$ have full rank. Then, from (62) we obtain $\binom{\tau_2}{\tau_3} = N^{-1}(\boldsymbol{a} - \tau_1 \boldsymbol{b})$,

where $\boldsymbol{b} = (\mathbf{0}, I_2)\hat{\boldsymbol{u}}_1$. Subsequently,

$$\bar{\boldsymbol{\Delta}} = (\hat{\boldsymbol{u}}_1, \hat{\boldsymbol{u}}_2, \hat{\boldsymbol{u}}_3)\begin{pmatrix} \tau_1 \\ N^{-1}(\boldsymbol{a} - \tau_1 \boldsymbol{b}) \end{pmatrix}.$$

Substitution of the above into (53) will yield $W_{\mathcal{F}}$ as a quadratic function of $\tau_1$ with a non-negative leading coefficient. The optimal pure resistance is obtained from $dW_{\mathcal{F}}/d\tau_1 = 0$. The solution is given as (91) in Appendix D. The optimal pure resistance assumes the form (61), where

$$\begin{pmatrix} \boldsymbol{\psi}_1 \\ \boldsymbol{\psi}_2 \end{pmatrix} = (I_4, \mathbf{0})(\hat{\boldsymbol{u}}_1, \hat{\boldsymbol{u}}_2, \hat{\boldsymbol{u}}_3)\begin{pmatrix} \tau_1^* \\ N^{-1}(\hat{\boldsymbol{a}} - \tau_1^* \boldsymbol{b}) \end{pmatrix} \tag{63}$$

with $\tau_1^*$ given in Appendix D.

## 6.2 Fixed Segment Contacts

In this section, the contact index sets $\mathbb{I}, \mathbb{J}, \mathbb{K}$ may have sizes greater than one, but they will not change. In other words, no existing contact will break or new contact will be established. All the nodes in contact with the same finger undergo the same displacement. More specifically, a contact node $\boldsymbol{p}_t$ is displaced by

$$\boldsymbol{\delta}_t = \begin{cases} \boldsymbol{d}_1, & \text{if } t \in \mathbb{I}; \\ \boldsymbol{d}_2, & \text{if } t \in \mathbb{J}; \\ \boldsymbol{a}, & \text{if } t \in \mathbb{K}. \end{cases} \tag{64}$$

Let $\bar{\boldsymbol{\Delta}}$ be the column vector that gathers $\boldsymbol{\delta}_t$, for all $t \in \mathbb{I}$, followed by $\boldsymbol{\delta}_t$, for all $t \in \mathbb{J}$, and then by $\boldsymbol{\delta}_t$, for all $t \in \mathbb{K}$. In other words,

$$\bar{\boldsymbol{\Delta}} = (\boldsymbol{d}_1^T, \ldots, \boldsymbol{d}_1^T, \boldsymbol{d}_2^T, \ldots, \boldsymbol{d}_2^T, \boldsymbol{a}^T, \ldots, \boldsymbol{a}^T)^T. \tag{65}$$

Rearrange the rows and columns of the reduced stiffness matrix $C$ in the same index order as in $\bar{\boldsymbol{\Delta}}$.

Again, we first consider stable resistances, for which the following generalizations of (54) and (55) hold:

$$\sum_{t \in \mathbb{I} \cup \mathbb{J} \cup \mathbb{K}} \boldsymbol{\delta}_t = \mathbf{0} \quad \text{and} \quad \sum_{t \in \mathbb{I} \cup \mathbb{J} \cup \mathbb{K}} \boldsymbol{p}_t \times \boldsymbol{\delta}_t = 0.$$

After plugging in (64), the first condition above yields $\boldsymbol{d}_2$ in terms of $\boldsymbol{d}_1$ and $\boldsymbol{a}$. Substitute the result into the second condition to yield

$$|\mathbb{I}|(\breve{\boldsymbol{p}} - \breve{\boldsymbol{q}}) \times \boldsymbol{d}_1 + |\mathbb{K}|(\breve{\boldsymbol{r}} - \breve{\boldsymbol{q}}) \times \boldsymbol{a} = 0, \tag{66}$$

where $\breve{\boldsymbol{p}} = \frac{1}{|\mathbb{I}|}\sum_{t \in \mathbb{I}} \boldsymbol{p}_t$, $\breve{\boldsymbol{q}} = \frac{1}{|\mathbb{J}|}\sum_{t \in \mathbb{J}} \boldsymbol{p}_t$, and $\breve{\boldsymbol{r}} = \frac{1}{|\mathbb{K}|}\sum_{t \in \mathbb{K}} \boldsymbol{p}_t$ are referred to as the *contact centroids* of the fingers $\mathcal{F}_1, \mathcal{F}_2, \mathcal{A}$, respectively.

As in the case of fixed point contacts treated in Section 6.1.1, we write the work done by $\mathcal{F}_1$ and $\mathcal{F}_2$ in the form of (57), except $H$, $\boldsymbol{c}$, and $\omega$ have different forms, which are given in Appendix D.

**Proposition 12** *The matrix $H$ is positive semidefinite. That $\boldsymbol{d}_1 \in \mathrm{null(H)}$ if and only if the following three conditions are all satisfied: i) $|\mathbb{I}| = |\mathbb{J}| = |\mathbb{K}| = 1$; ii) $\boldsymbol{p}_k = \frac{1}{2}(\boldsymbol{p}_i + \boldsymbol{p}_j)$; and iii) $\boldsymbol{d}_1 \cdot (\boldsymbol{p}_i - \boldsymbol{p}_j) = 0$. In ii) and iii), $i, j, k$ are the only indices in $\mathbb{I}, \mathbb{J}, \mathbb{K}$, respectively, following i).*

**Algorithm 2** Resisting a Translating Adversary Finger under Frictional Segment Contact

**Input:** contact index sets $\mathbb{I}, \mathbb{J}, \mathbb{K}$ for $\mathcal{F}_1, \mathcal{F}_2, \mathcal{A}$, translation $\boldsymbol{a}$ of $\mathcal{A}$

$a \leftarrow 0$
let $\mathbb{I}, \mathbb{J}, \mathbb{K}$ contain the indices of the initial point contacts with $\mathcal{F}_1, \mathcal{F}_2, \mathcal{A}$, respectively
initialize $\mathbb{T}$ and $\mathbb{P}$
**while** $a < \|\boldsymbol{a}\|$ and no finger slips **do**
    construct the form of $\tilde{W}'_{\mathcal{F}}$ based on (67), (68), and $\mathbb{I}, \mathbb{J}, \mathbb{K}$
    minimize $\tilde{W}'_{\mathcal{F}}$ to obtain $\boldsymbol{\psi}_1$ and $\boldsymbol{\psi}_2$ as the translations of $\mathcal{F}_1$ and $\mathcal{F}_2$ in response to a (hypothesized) unit translation $\boldsymbol{a}/\|\boldsymbol{a}\|$ by $\mathcal{A}$
    execute lines 4–11 of Algorithm 1 until the next contact event occurs (inside the **repeat**-**until** statement, increment $\boldsymbol{\delta}'_t$ by $h\boldsymbol{\psi}_1$ if $t \in \mathbb{I}$, by $h\boldsymbol{\psi}_2$ if $t \in \mathbb{J}$, or by $h\hat{\boldsymbol{a}}$ if $t \in \mathbb{K}$)
    compute the actual work $W'_{\mathcal{F}}$
    $W_{\mathcal{F}} \leftarrow W_{\mathcal{F}} + W'_{\mathcal{F}}$
    update $\mathbb{I}, \mathbb{J}, \mathbb{K}, \mathbb{T}, \mathbb{P}$ according to the contact event
    update the contact force $\boldsymbol{f}_t, \forall\, t \in \mathbb{I} \cup \mathbb{J} \cup \mathbb{K}$
**end while**
**if** $a < \|\boldsymbol{a}\|$ and ($\mathcal{F}_1$ or $\mathcal{F}_2$ slips) **then**
    **return** failure
**else**
    **return** $W_{\mathcal{F}}$
**end if**

See Appendix F for the proof of the proposition. Minimization of the work $W_{\mathcal{F}}$ parallels that of (57) in Section 6.1.1, via a decomposition of $\boldsymbol{d}_1$ along the direction $\hat{\boldsymbol{t}}$ of $\breve{\boldsymbol{p}} - \breve{\boldsymbol{q}}$, and its orthogonal direction $\hat{\boldsymbol{n}}$. The optimal stable resistance assumes the form (61), where $\boldsymbol{\psi}_1$ and $\boldsymbol{\psi}_2$ have similar forms to those in the case of fixed point contacts treated in Section 6.1.1. Please refer to Appendix D for their expressions.

The case of optimal pure resistance with fixed segment contacts also generalizes that with fixed point contacts in Section 6.1.2. We will end up with a very similar optimization problem. Details are offered in the end of Appendix D.

## 6.3 Frictional Segment Contacts

We are finally ready to consider optimal resistance with segment contacts under friction. The two grasping fingers and the adversary finger have semicircular fingertips with possibly different radii. In a realistic scenario, the grasping fingers $\mathcal{F}_1$ and $\mathcal{F}_2$ first perform a squeeze on the object by translating toward each other via $s(\boldsymbol{p}_j - \boldsymbol{p}_i)$ and $s(\boldsymbol{p}_i - \boldsymbol{p}_j)$, respectively, for some $s > 0$. Then the adversary finger $\mathcal{A}$ makes contact at the node $\boldsymbol{p}_k$ and begins a translation $\boldsymbol{a} = \|\boldsymbol{a}\|\hat{\boldsymbol{a}}$ to try to break the grasp. The system configuration right before this disturbance, including the object's deformed shape and the contact index sets $\mathbb{I}$ and $\mathbb{J}$ for $\mathcal{F}_1$ and $\mathcal{F}_2$, can be determined using Algorithm 1 from Section 5.4.

Algorithm 2 describes how $\mathcal{F}_1$ and $\mathcal{F}_2$ resist $\mathcal{A}$. It employs an extension to Algorithm 1, which works for two grasping fingers only. Instead of the squeeze depth, the translation distance by the adversary finger $\mathcal{A}$ will be sequenced into $a_0 = 0 < a_1 < \cdots < \|\boldsymbol{a}\|$ such that at every $a_l$, one of the four contact events A, B, C, and D described in Section 5.3 takes place. Again, denote by $\mathbb{I}, \mathbb{J}, \mathbb{K}$ the sets of indices of the nodes that are in contact with $\mathcal{F}_1$, $\mathcal{F}_2$, $\mathcal{A}$, respectively.

Consider the moment when $\mathcal{A}$ has translated by the distance $a_l$. As in Section 5, for a contact node $\boldsymbol{p}_t$

we use $\boldsymbol{\delta}_t^{(l)}$, $\boldsymbol{f}_t^{(l)}$, and $\theta_t^{(l)}$ to refer to its displacement, contact force, and polar angle (with respect to the center of its contacting fingertip).

Next, $\mathcal{A}$ will continue moving by an extra distance $\xi$ in the direction of $\boldsymbol{a}$. Suppose that $\xi$ is small enough such that all contacts and their modes will not change. We determine the extra translations $\boldsymbol{d}'_1$ of $\mathcal{F}_1$ and $\boldsymbol{d}'_2$ of $\mathcal{F}_2$ to resist this extra movement by $\mathcal{A}$, via minimizing the extra work done by these two fingers:

$$W'_{\mathcal{F}} = \sum_{t\in\mathbb{I}\cup\mathbb{J}} \boldsymbol{\delta}_t'^T \boldsymbol{f}_t^{(l)} + \frac{1}{2}\sum_{t\in\mathbb{I}\cup\mathbb{J}} \boldsymbol{\delta}_t'^T \boldsymbol{f}'_t. \tag{67}$$

In the above, for $t \in \mathbb{I}\cup\mathbb{J}$, $\boldsymbol{\delta}'_t$ is the change in the displacement of the contact node $\boldsymbol{p}_t$ from $\boldsymbol{\delta}_t^{(l)}$, and $\boldsymbol{f}'_t$ the change in its contact force from $\boldsymbol{f}_t^{(l)}$.

During this extra translation period, if a node $\boldsymbol{p}_t$, $t \in \mathbb{I}\cup\mathbb{J}$, sticks, then $\boldsymbol{\delta}'_t = \boldsymbol{d}'_1$ or $\boldsymbol{d}'_2$. If it slides, then $\boldsymbol{\delta}'_t$ will be the sum of $\boldsymbol{d}'_1$ or $\boldsymbol{d}'_2$ and the node's movement $r\binom{\cos\theta_t - \cos\theta_t^{(l)}}{\sin\theta_t - \sin\theta_t^{(l)}}$ on the tip of whichever of $\mathcal{F}_1$ or $\mathcal{F}_2$ that it is in contact with. Minimization of $W'_{\mathcal{F}}$ would be over $\boldsymbol{\delta}'_1$ and $\boldsymbol{\delta}'_2$, and the polar angle $\theta_t$ of every sliding contact $\boldsymbol{p}_t$. It could get too inefficient.

We stipulate that the work done on $\boldsymbol{p}_t$, $t \in \mathbb{I}\cup\mathbb{J}$, due to its sliding, by the contacting finger $\mathcal{F}_1$ or $\mathcal{F}_2$ will be significantly less than the amount due to its translation with the finger.[19] Instead of minimizing $W'_{\mathcal{F}}$, we minimize its approximation $\tilde{W}'_{\mathcal{F}}$ by treating every sliding node in contact with $\mathcal{F}_1$, $\mathcal{F}_2$, or $\mathcal{A}$ as if it would be sticking during the period of the extra resistance period.

In short, whether a contact node $\boldsymbol{p}_t$ sticks or slips, its extra displacement $\boldsymbol{\delta}'_t$ will be set as follows:

$$\boldsymbol{\delta}'_t = \begin{cases} \boldsymbol{d}'_1, & \text{if } t \in \mathbb{I}; \\ \boldsymbol{d}'_2, & \text{if } t \in \mathbb{J}; \\ \xi\hat{\boldsymbol{a}}, & \text{if } t \in \mathbb{K}. \end{cases} \tag{68}$$

Then $\boldsymbol{d}'_1 = \xi\boldsymbol{\psi}_1$ and $\boldsymbol{d}'_2 = \xi\boldsymbol{\psi}_2$, where $\boldsymbol{\psi}_1$ and $\boldsymbol{\psi}_2$ are determined like $\boldsymbol{d}_1$ and $\boldsymbol{d}_2$ in Section 6.2 with $\hat{\boldsymbol{a}}$ replacing $\boldsymbol{a}$. All the above is carried out in lines 5–6 of the algorithm.

We now determine the extra distance $\xi$ by which $\mathcal{A}$ translates until the next contact event happens, by extending Algorithm 1 to the present case with three fingers. The extension is straightforward because all three fingers are under translations that depend on $\xi$ only. Event conditions (48)–(51) are tested, with every increment $h$ of $\xi$. Here, we must take into account contact node sliding. Once an event occurs, the overall translation distance for $\mathcal{A}$ is updated as $a_{l+1} = a_l + \xi$. In addition to the index sets $\mathbb{I}, \mathbb{J}, \mathbb{K}$, update the index set $\mathbb{P}$ for sliding contacts (with any of $\mathcal{F}_1, \mathcal{F}_2$, and $\mathcal{A}$) and the index set $\mathbb{T}$ for sticking contacts. This is summarized in lines 7–11 of Algorithm 2.

If the adversary finger $\mathcal{A}$ begins to slip after an event, it has been successfully resisted. If either $\mathcal{F}_1$ or $\mathcal{F}_2$ starts to slide, the grasp fails to resist $\mathcal{A}$. If none of the above two cases happens, $\mathcal{A}$ will complete its translation $\boldsymbol{a}$ while being resisted.

Figure 10(a) shows a convex shape grasped under a stable squeeze by $\mathcal{F}_1$ (motionless) and $\mathcal{F}_2$ (translating via $(-0.00068, 0.002)^T$ from $\boldsymbol{p}_j$ to $\boldsymbol{p}_i$). Then, an adversary finger $\mathcal{A}$ starts pushing the object through translation $\boldsymbol{a} = (0.0024, 0.0044)^T$, as shown in (b). All three fingertips have radius 0.02. Algorithm 2 generates two trajectories shown in (c) for $\mathcal{F}_1$ and $\mathcal{F}_2$ for a stable resistance. They have total displacements $\boldsymbol{d}_1 = (-0.0007, -0.0005)^T$ and $\boldsymbol{d}_2 = (-0.0008, -0.0019)^T$. Table 3 displays the components of the finger forces exerted along the translation directions, at the start and the end of resistance, and the work performed

[19] As remarked in Section 5.5, in grasping the foam rubber square shown in Table 1, all sliding distances were within 1% of the gap between two adjacent nodes.

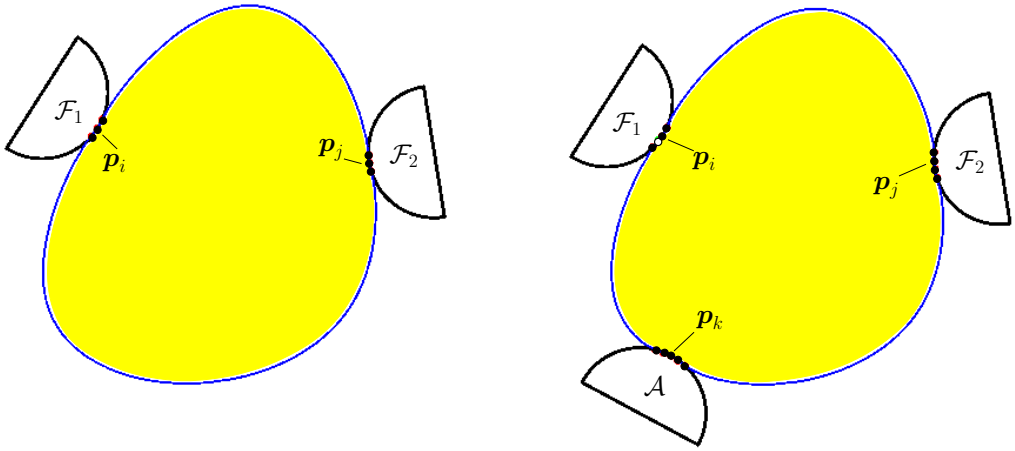


(a) (b)

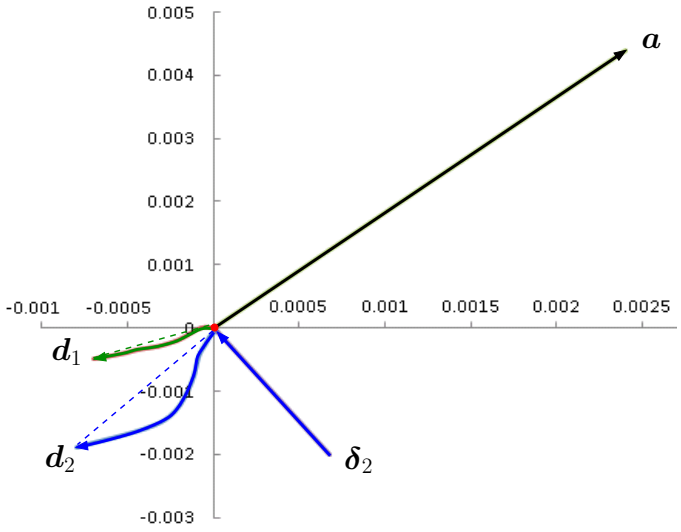


(c)

**Figure 10**: Resisting an adversary semicircular fingertip under friction. (a) A convex shape grasped via a stable squeeze. (b) Successful resistance to an adversary finger $\mathcal{A}$. (c) Trajectories of the three fingers during the resistance, with their starting points translated to coincide with the origin, which, for display purpose, is also made the ending point of the trajectory $\boldsymbol{\delta}_2$ of $\mathcal{F}_2$ in achieving an initial grasp before the resistance. Dashed lines mark the actual trajectories of $\mathcal{F}_1$ and $\mathcal{F}_2$ in a validation experiment to be described in Section 6.4.

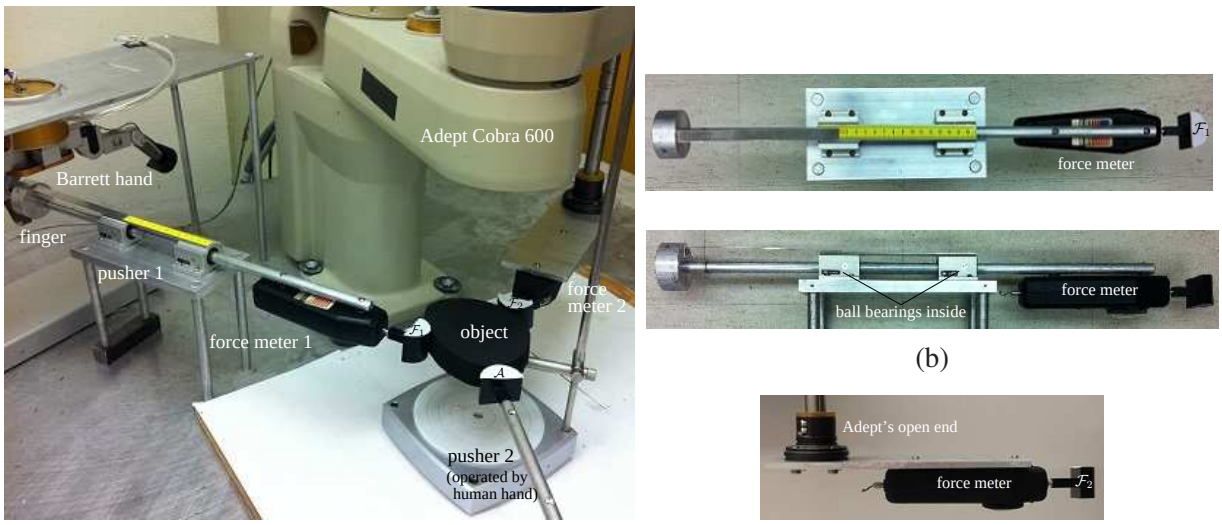


(a) (b) (c)

**Figure 11**: Setup for experimental validation of the simulation results shown in Figure 10. (a) Grasping fingertips $\mathcal{F}_1$ and $\mathcal{F}_2$ driven by a finger of the Barrett hand and an Adept Cobra 600 manipulator, respectively, and adversary fingertip $\mathcal{A}$ by the human hand. (b) $\mathcal{F}_1$ attached to a force meter rigidly connected to a linear mechanism pushed by the Barrett finger. (c) $\mathcal{F}_2$ attached to another force meter rigidly connected to the Adept's open end via an adapter.

by the grasping fingers. A negative force reading on $\mathcal{F}_1$ indicates that the contact force influenced by friction was 'pulling' away from the translation direction of the finger. Contact events A, B, C, D occurred 7, 0, 3, and 2 times, respectively, during the resistance. In the simulation, Young's modulus, Poisson's ratio, and the coefficient of friction assume the same values measured in the experiment from Section 5.5.

| | $\mathcal{F}_1$ | $\mathcal{F}_2$ |
|---|---|---|
| force (start) | $-2.566$ | 2.098 |
| force (end) | $-1.23$ | 8.136 |
| work | $\mathbf{-0.0015}$ | **0.0101** |

**Table 3**: Forces exerted and work performed by the the two grasping fingers in Figure 10 under translations $\boldsymbol{d}_1$, $\boldsymbol{d}_2$, and $\boldsymbol{a}$.

## 6.4 Experiment on Grasp Resistance

Shown in Figure 11(a) is an experiment to validate the results in Table 3 from the instance in Figure 10. An object of exactly the same shape in Figure 10 was placed on a raised platform. It was made of the same type of foam rubber used in the experiment from Section 5.5. The same pair of grasping fingertips $\mathcal{F}_1$ and $\mathcal{F}_2$ from that experiment were respectively actuated by the Barrett Hand and an Adept Cobra 600 manipulator. The values of Young's modulus, Poisson's ratio, and the coefficient of contact friction did not change from the aforementioned experiment. Since none of the three fingers of the Barrett Hand could be controlled to perform straight line motions, we let its independently controlled middle finger push $\mathcal{F}_1$ via a linear mechanism. Displayed in (b) in both top-down and side views, the mechanism was a cylindrical aluminum stick constrained to linear motions by ball bearings embedded inside two boxes. At its one end

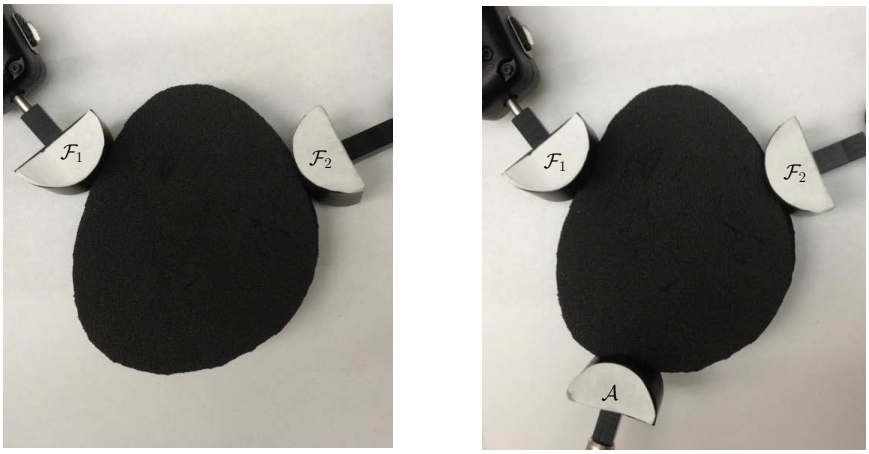


(a) (b)

**Figure 12**: Experimental validation of the simulation result shown in Figure 10. (a) Grasp of a convex object corresponding to Figure 10(a). (b) Its resistance to an adversary finger $\mathcal{A}$ corresponding to Figure 10(b). The translation $\boldsymbol{\delta}_2$ by $\mathcal{F}_2$ in (a), and the translations $\boldsymbol{d}_1$, $\boldsymbol{d}_2$, and $\boldsymbol{a}$ by $\mathcal{F}_1, \mathcal{F}_2$ and $\mathcal{A}$ in (b) are (straightened) from the trajectories in Figure 10(c).

was a disk to be pushed by the finger of the Barrett Hand. Near its other end, the stick had a force meter (from Ametek Hunter Spring) attached underneath. The tip $\mathcal{F}_1$ was mounted at the front end of the force meter, which would be able to measure the axial force exerted by the tip once it established contact with the object. As shown in (c), $\mathcal{F}_2$ was attached to another force meter, which was rigidly connected to the Adept's open end via an adapter. The manipulator has an accuracy of 0.02mm in any horizontal direction.

The human hand pushed the adversary fingertip $\mathcal{A}$ via another linear mechanism identical to the one driving $\mathcal{F}_1$. No force meter was attached to this pusher. A ruler was mounted on top of the two ball bearing boxes to measure the travel distance by $\mathcal{A}$. The translations by $\mathcal{F}_1$ and $\mathcal{F}_2$, meanwhile, were precisely controlled by the Barrett Hand and the Adept.

The fingers $\mathcal{F}_1$ and $\mathcal{F}_2$ first made contact with the object. To repeat the simulation instance in Section 6.3, $\mathcal{F}_1$ stayed still while $\mathcal{F}_2$ squeezed the object via a translation $(-0.00068, 0.002)^T$ along the line through their initial contact points with the object. The configuration after the squeeze is shown in Figure 12(a). Afterward, the human hand pushed $\mathcal{A}$ via the linear mechanism to complete the same translation $\boldsymbol{a} = (0.0024, 0.0044)^T$ as in the simulation. Algorithm 2 from Section 6.3 generated two trajectories shown in Figure 10(c) respectively for $\mathcal{F}_1$ and $\mathcal{F}_2$ based on stable squeezes. For ease of control, each trajectory was straightened by connecting its starting location to its final location (see the dashed lines in Figure 10(c)). The push through $\boldsymbol{a}$ was being resisted simultaneously by the Barrett hand and the Adept arm translating by $\boldsymbol{d}_1$ and $\boldsymbol{d}_2$ along the straightened trajectories.

We refer to the resistance specified by $\boldsymbol{d}_1$ and $\boldsymbol{d}_2$ as the 'optimal' resistance. During the resistance, $\mathcal{F}_1$ retreated slightly (i.e., moved away from the object). The work done by $\mathcal{F}_1$ or $\mathcal{F}_2$ was estimated as half the product of the translation distance with the sum of the initial and final force readings. Columns 2 and 3 in Table 4 displayed the force readings on these two grasping fingers at the start and end of the resistance, and the work they performed. Small discrepancies exist in comparison with Table 3. They were mainly due to the trajectory straightening and measurement errors in the experiment.

For comparison, we also tested an 'arbitrary' resistance strategy against the same adversary finger disturbance. We arbitrarily chose a translation direction $\boldsymbol{d}_1/\|\boldsymbol{d}_1\| = (0.447, -0.894)^T$ for $\mathcal{F}_1$. Then $\boldsymbol{d}_1 =$

| | 'optimal' resist. | | 'arbitrary' resist. | |
|---|---|---|---|---|
| finger | $\mathcal{F}_1$ | $\mathcal{F}_2$ | $\mathcal{F}_1$ | $\mathcal{F}_2$ |
| force (start) | $-2.67$ | 2.22 | 4.20 | 7.05 |
| force (end) | $-1.45$ | 8.06 | 13.93 | 14.86 |
| work | $\mathbf{-0.0017}$ | **0.0107** | **0.0328** | **0.0463** |

**Table 4**: Forces exerted and work performed by $\mathcal{F}_1$ and $\mathcal{F}_2$ in Figure 11 under $\boldsymbol{d}_1$ and $\boldsymbol{d}_2$ computed by the resistance algorithm (columns 2–3) or arbitrarily chosen (columns 4–5).

$(0.0016, -0.0032)^T$ and $\boldsymbol{d}_2 = (-0.004, -0.0012)^T$ were determined from the condition $(\boldsymbol{d}_1^T, \boldsymbol{d}_2^T, \boldsymbol{a}^T)^T \perp \mathrm{col}(B)$ for a stable squeeze. The experimental result was shown in columns 4 and 5 in Table 4. It can be seen that much less work was carried out by $\mathcal{F}_1$ and $\mathcal{F}_2$ under the 'optimal' resistance strategy.

# 7 Squeezing Ring-like Objects

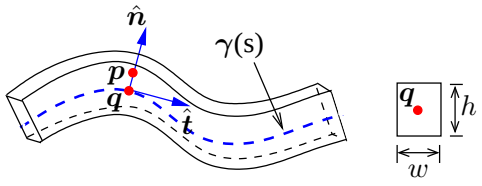


**Figure 13**: Segment of a curve-like shape with rectangular cross section.

A variety of objects, from plastic and metal cookie cutters to rubber and onion rings, are hollow. More likely to bend than solid objects, they tend to make very small contact areas with the grasping fingers such that these contacts are well approximated as points.

Such a ring-like object may be viewed as being swept out by a rectangular cross section with width $w$ and height $h$ along a closed plane curve $\boldsymbol{\gamma}(s)$ parametrized by arc length $s$. Referred to as the middle curve, $\boldsymbol{\gamma}(s)$ has its perimeter $l$ significantly greater than $w$ and $h$. Figure 13 illustrates a section of the object. Denote by $\hat{\boldsymbol{t}}$ and $\hat{\boldsymbol{n}}$ respectively the unit tangent and normal at a point on the curve $\boldsymbol{\gamma}$. Because of its small dimensions, the cross section is assumed to have no deformation. Therefore, we treat Poisson's ratio as zero. The object is essentially a degenerated shell that is very small in two out of three dimensions.

## 7.1 Grasp Testing

We follow Kirchhoff's assumptions (Reddy, 2007, p. 96) that fibers initially normal to $\boldsymbol{\gamma}$ remain straight after deformation, do not change their lengths, and remain normal to the curve $\boldsymbol{\gamma}(s) + \boldsymbol{\delta}(s)$ that deforms from $\boldsymbol{\gamma}(s)$. Here the displacement of $\boldsymbol{\gamma}(s)$ is $\boldsymbol{\delta}(s) = \alpha(s)\hat{\boldsymbol{t}} + \beta(s)\hat{\boldsymbol{n}}$.

For a small deformation, we obtain the extensional strain $\epsilon$ and the change in curvature $\zeta$ at a point $\boldsymbol{q}$ on $\boldsymbol{\gamma}$ with a reduction of one dimension from those for shells (Tian and Jia, 2010):

$$\begin{aligned} \epsilon &= \nabla_{\hat{t}}\alpha + (\nabla_{\hat{t}}\hat{\boldsymbol{n}} \cdot \hat{\boldsymbol{t}})\beta \\ &= \frac{d\alpha}{ds} - \kappa\beta, \end{aligned} \tag{69}$$

$$\begin{aligned} \zeta &= \nabla_{\hat{t}}\left(-\nabla_{\hat{t}}\beta + (\nabla_{\hat{t}}\hat{\boldsymbol{n}} \cdot \hat{\boldsymbol{t}})\alpha\right) \\ &= -\frac{d^2\beta}{ds^2} - \frac{d\kappa}{ds}\alpha - \kappa\frac{d\alpha}{ds}. \end{aligned} \tag{70}$$

In the above, $\kappa$ is the curvature of $\boldsymbol{\gamma}(s)$, $\nabla_{\hat{t}}\alpha$ the *directional derivative* of $\alpha$ with respect to $\hat{\boldsymbol{t}}$, and $\nabla_{\hat{t}}\hat{\boldsymbol{n}}$ the *covariant derivative* which measures the rate of change of the normal $\hat{\boldsymbol{n}}$ along the curve $\boldsymbol{\gamma}$ at $\boldsymbol{q}$.[20]

As shown in Figure 13, we let $\boldsymbol{p}$ be a point inside the object. The normal section through $\boldsymbol{p}$ intersects the middle curve $\boldsymbol{\gamma}(s)$ at $\boldsymbol{q}$. The strain and stress at $\boldsymbol{p}$ are respectively $\epsilon + y\zeta$ and $E(\epsilon + y\zeta)$. The object's strain energy is obtained via integration:

$$\begin{aligned} U &= \int_V \frac{1}{2}\sigma\epsilon \, dV \\ &= \frac{1}{2}\int_V E(\epsilon + y\zeta)^2 w \, dyds \\ &= \frac{1}{2}Ew\int_0^l \int_{-\frac{h}{2}}^{\frac{h}{2}} (\epsilon + y\zeta)^2 \, dyds \\ &= \frac{1}{2}Ew\int_0^l \left(h\epsilon^2 + \frac{h^3}{12}\zeta^2\right) ds. \end{aligned} \tag{71}$$

In (71), the component linear in the height $h$ represents the extensional energy, while the cubic component represents the bending energy.

Under FEM, we discretize the middle curve $\boldsymbol{\gamma}$ into linear elements and rewrite the strain energy into the standard form $U = \frac{1}{2}\boldsymbol{\Delta}^T K \boldsymbol{\Delta}$, where $\boldsymbol{\Delta}$ gathers the displacements of all the nodes on the middle curve $\boldsymbol{\gamma}$. The stiffness matrix thus obtained again has a three-dimensional null space that comprises all translations and rotations in the plane. Results from Section 3 on the uniqueness of deformation carry over for specified displacements of two contact nodes.

Unlike on a solid object, no tangent discontinuity occurs at a point contact on the ring-like object under deformation caused by point loads. The displacement of every node is linear in the squeeze depth $\rho$. We estimate the normal at a contact $\boldsymbol{p}_i$ by approximating its osculating circle with the circle passing through the displaced locations $\tilde{\boldsymbol{p}}_i$ of $\boldsymbol{p}_i$, and $\tilde{\boldsymbol{p}}_{i-1}$ and $\tilde{\boldsymbol{p}}_{i+1}$ of its adjacent nodes $\boldsymbol{p}_{i-1}$ and $\boldsymbol{p}_{i+1}$. The center $\boldsymbol{o}$ of the circle lies at the intersection of the perpendicular bisectors of the segments $\overline{\tilde{\boldsymbol{p}}_{i-1}\tilde{\boldsymbol{p}}_i}$ and $\overline{\tilde{\boldsymbol{p}}_i\tilde{\boldsymbol{p}}_{i+1}}$. The inward normal, approximated by the vector from $\boldsymbol{o}$ to $\tilde{\boldsymbol{p}}_i$, becomes a fractional in $\rho$ with a cubic polynomial as the numerator and a quadratic polynomial as the denominator. Meanwhile, the contact force $\boldsymbol{f}_i$ at $\boldsymbol{p}_i$ is linear in $\rho$. Determining when it will reach the left or right edge of the contact friction cone reduces to finding the roots of some cross products, which are essentially the roots of some quartic polynomials (and thus have closed forms).

The object is represented as a linear mesh consisting of a sequence of $n$ segments, and the strain within each segment is everywhere the same. The element with the highest strain will stay the same as $\rho$ increases. It is located by an $O(n)$-time search. Thus, we can determine the $\rho$ value at which the material's proportional limit is exceeded. The maximum $\rho$ value without violating a friction cone constraint or exceeding the proportional limit can be computed beforehand. Given a squeeze depth $\rho$, we can answer if the squeeze will be successful in $O(n)$ time.

## 7.2 Experiment with Ring-like Objects

The shape of an object in the experiment was either obtained using a scanner or reconstructed over sampled points from a closed form. Two fingers of the Barrett Hand were used directly in grasping without mounting

[20] If the curve parametrization is arbitrary-speed, say, in the form of $\boldsymbol{\gamma}(t)$, we can easily evaluate $\epsilon$ and $\zeta$ according to (69) and (70) based on $ds/dt = \|d\boldsymbol{\gamma}/dt\|$.

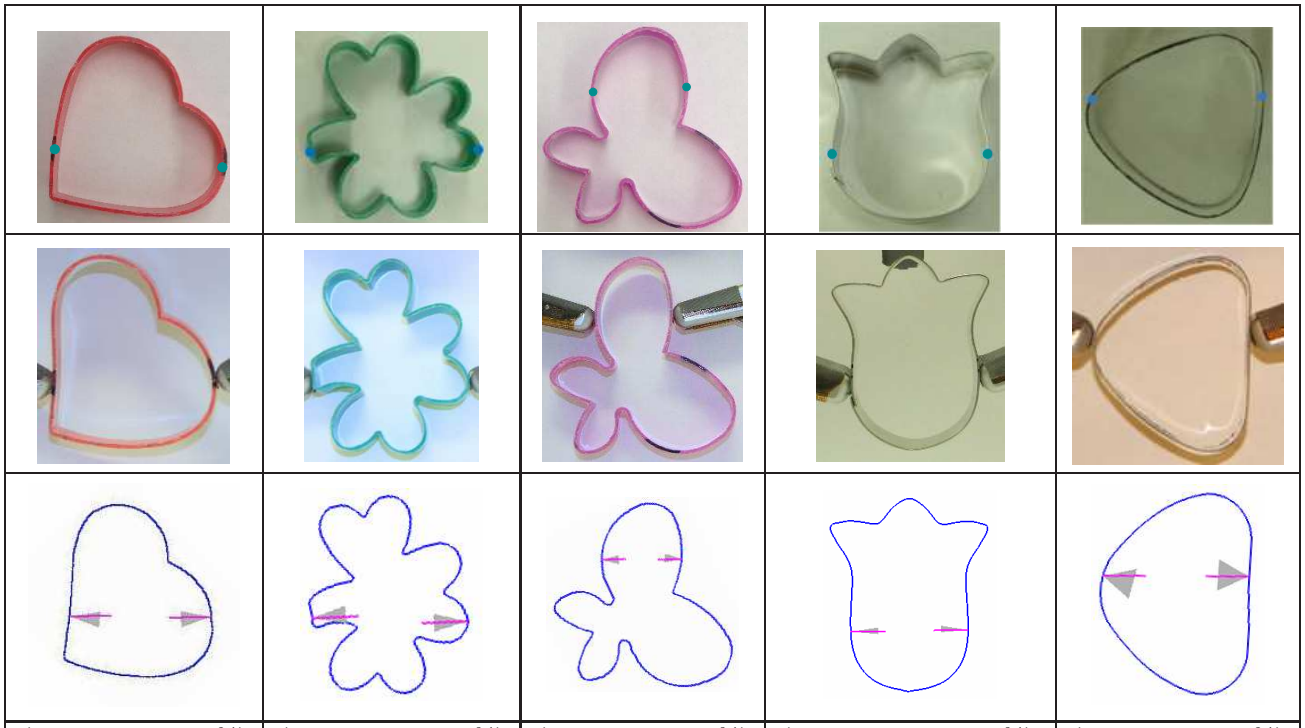

| $(2, 0.26, 0.005, 10\%)$ | $(2, 0.26, 0.005, 11\%)$ | $(2, 0.26, 0.005, 9\%)$ | $(200, 0.12, 0.003, 15\%)$ | $(3, 0.5, 0.003, 15\%)$ |
|---|---|---|---|---|

**Table 5**: Successful grasps of five deformable objects (row 1) both in experiment (row 2) and from simulation (row 3) under specified values of the physical parameters $(E, \mu, h, \varrho)$ (row 4).

any external tips. Their tips were much more pointed than the semicircular ones used in the experiments described in Sections 5.5 and 6.4. The two fingers had one coupled control such that their tips were always at the same height during a grasping operation. Since the fingers could only perform coupled translations toward each other, only stable squeezes were tested. Also, for setup convenience, all ring-like objects in the experiment were vertical given their light weights. The grasp testing method from Section 7.1 was employed to predict all finger placements that could result in grasps under specified squeeze depths. The Barrett Hand then performed grasping operations under some placements randomly selected from the predictions.

Table 5 shows successful grasps of five objects. In the first row, the boundary of each object is marked with two dots to indicate the finger placement that was executed. The second row displays these objects under some squeeze grasps by the Barrett Hand. The third row shows the corresponding simulation results, with contact friction cones drawn as gray triangles and forces indicated by short purple lines. At every contact, the friction was enough to keep the contact force pointing at the opposite contact, which ensures equilibrium. The last row lists the estimated values of the physical parameters for these grasps: Young's modulus $E$ (GPa), coefficient of friction $\mu$, thickness $h$, and the relative squeeze depth $\varrho$.

Figure 14 shows the grasp failure resulting from a different finger placement on the butterfly-shaped object in entry (1, 3) of Table 5 than the placement in entry (2, 3). Part (a) of the figure reveals that both contact friction cones on the original object have rotated (in the arrow directions) under the squeeze. The computed force $\boldsymbol{f}_j$ at the upper contact $\boldsymbol{p}_j$ is out of its friction cone, while the $\boldsymbol{f}_i$ at the lower contact $\boldsymbol{p}_i$ is aligned with the right edge of its friction cone. In (b), the object escaped completely from the grasp, releasing its strain energy. In (c), the same finger placement succeeded on the same object with plastic foam


(a) (b) (c)

**Figure 14**: Grasp failure due to deformation at the relative squeeze depth of 15%. (a) Contact forces out of the friction cones. (b) Escape of the object. (c) Success at grasping a 'rigid' identical shape under the same finger placement.

stuffed inside. Though with the same boundary shape and material, the stuffed object is far more 'rigid' (because of the high Young's modulus of the plastic foam) than the original one filled with air inside.

Rotations of contact friction cones caused by deformation do not always lead to a grasp failure. On some occasions, they rotate toward each other, so that the grasping forces become more aligned with the cone axes to strengthen the grasp. An example is given over the same object in Figure 15.

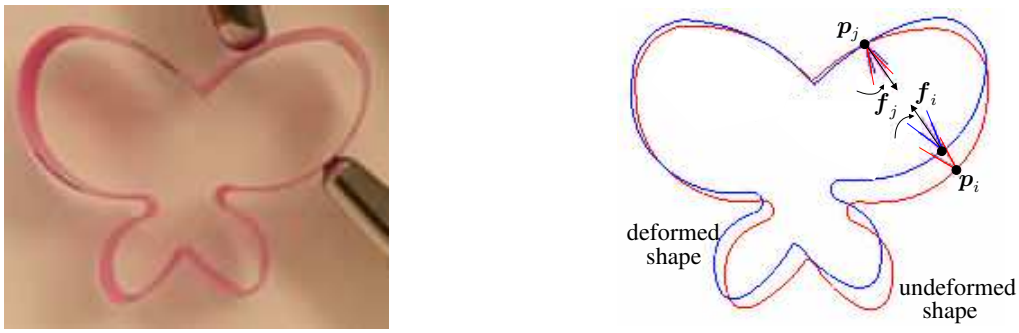


(a) (b)

**Figure 15**: Rotations of two contact friction cones make the grasping forces more aligned in (a) experiment and (b) the corresponding simulation, where the arrows indicate the rotation directions.

## 8 Discussion and Future Work

This paper studies how to grasp a planar deformable object by squeezing it with two fingers. *One key idea is to specify the displacements of the grasping fingers rather than the forces they need to exert.* Moving the fingers according to prescribed displacements will not only maintain torque equilibrium as deformation happens, but also be easy to control. The displacements will additionally serve as the constraints for updating the deformed shape using, say, FEM.

*The second key idea is to introduce two types of squeeze on a deformable object.* A stable squeeze minimizes the potential energy for the same amount of squeeze by moving the two fingers toward each other. A pure squeeze ensures that the grasped object undergoes no rigid body motion as it deforms to eliminate unnecessary finger movements and to address the inapplicability of linear elasticity to modeling large rotations. They were introduced in Section 2.4 in terms of the (continuous) displacement field and are

hence applicable with a different computational method such as the boundary element method (BEM).

In a common situation with frictional segment contacts, contact configuration (including stick/slip statuses at individual contacts) is also needed for a deformation update. *The third key idea is to track this contact configuration in an event-driven manner as a squeeze continues.* A formal analysis of this grasping scheme is provided along with numerical simulation and robot experiments.

Algorithm 1 is similar in its iterative updating of contact status to previous FEM-based solutions to elastic contact problems (Okamoto and Nakazawa, 1979; Sachdeva and Ramakrishnan, 1981; Chandrasekaran et al., 1987). Contact constraints (46) for both sticking and sliding, and force constraints (47) for sliding were also used in the deformation computation by Sachdeva and Ramakrishnan (1981). However, these methods had to assume extra constraints for computing the deformation under input loads. In contrast, our algorithm takes as input specified displacements that can serve as constraints directly. Further, we characterize four types of contact event in the new context of robot grasping, in which objects are initially free rather than already constrained (fully or partially) as in classical solid mechanics problems.

We have also looked at the resistance by a formed grasp to an adversary finger pushing against the grasped object. *The fourth key idea is to measure the effort of such resistance by the amount of work performed by the grasping fingers, rather than the total force they exert as commonly used in rigid body grasping.* Optimal resistance strategies are first analyzed assuming fixed point and segment contacts. Then, Algorithm 2 is offered for the general case of area contacts under Coulomb friction, by incorporating the contact event detection subroutine from Algorithm 1.

Though rounded fingertips are considered for clarity, the strategies for grasping and resistance generalize to fingers with other shapes in a straightforward manner.

The described grasping strategies seemingly rely heavily on accurate measurements of physical parameters and monitoring of the contact regions between the fingers and the object. However, high accuracy for Young's modulus and Poisson's ratio appears to be unnecessary since equilibrium of force and torque are guaranteed by the physics of elasticity, as long as the contacts are not completely lost (due to a large rotation) or sliding in the same direction on a finger. Our experiments also suggested that there was large room for errors in the estimates for the physical parameters.

Monitoring of the contact region can be improved by mounting a tactile array sensor on each fingertip. The sensor could capture the fluctuations of the normal force to tell that a slip is about to happen (Howe and Cutkosky, 1989) in a small contact region corresponding to a node. Another indicator of a slip is the ratio between the normal and tangential components of the contact force (Howe 1994). For robustness, we need to modify the grasping algorithm into a reactive one in the future. The algorithm will be executed in real time with the grasp operation, receiving data from tactile sensors to monitor the contact regions, and adjusting the movements of the grasping fingers.

Under a stable squeeze, two fingers always translate toward each other, regardless of the object's shape. It is in principle directly applicable to unknown or partially known objects. Nevertheless, investigation is needed on monitoring the contact using a tactile sensor. In case a slip is about to happen, translate the fingers to squeeze in a new direction, say, of a pure squeeze or along the changed contact normals under deformation.

Generalization of the work to grasping 3D objects is under way. The concepts and algorithms presented in this work should carry over. Torques about the contact normals (just like in the situation of soft fingers on a hard object) may play a prominent role, especially, on grasp resistance.

Further investigation and experimental validation need to be conducted for the introduced grasp quality measures. We would like to explore, at more depth, the stability of grasping in the presence of a disturbance, especially the grasped object's ability to absorb the disturbance into its strain energy. Such absorption is

expected to be more prominent with large deformations, to which nonlinear elasticity theory (Novozhilov, 1959) needs to be applied.

A deformable object is often easier to grasp than a rigid object. Grasp resistance to a disturbance on a deformable body is also easier than on a rigid body, because not only does deformation enlarge the contact regions (and yields large frictional forces) but also the concavities of these regions cause the normal contact forces to directly participate in the resistance. The latter phenomenon can be prominent because the coefficient of friction is typically less than one. Investigation is underway on comparing rigid body grasping and deformable body grasping.

## Funding

Support for this research was provided by the National Science Foundation through the grant IIS-0915876. Any opinions, findings, and conclusions or recommendations expressed in this material are those of the authors and do not necessarily reflect the views of the National Science Foundation.

## Acknowledgment

We wish to thank former ISU undergraduate Trenton Anagnostopoulos for writing the mesh generation code, and Ph.D. student Feifei Wang for her help on the experiment in Section 6.4. We owe much appreciation to the anonymous reviewers of IJRR for their valuable feedback. This paper is a revision of two papers (Guo et al., 2013; Jia et al., 2013) that have respectively appeared in the proceedings of the IEEE International Conference on Robotics and Automation (ICRA) and the IEEE/RSJ International Conference on Intelligent Robots and Systems (IROS), both in 2013. Thanks to the anonymous reviewers of these two conference papers for their helpful comments.

## References

[1] Aliabadi MH (2002) *The Boundary Element Method, Applications in Solids and Structures*. Wiley, 2nd edition.

[2] Besl PJ and McKay ND (1992) A method for registration of 3-D shapes. *IEEE Transactions on Pattern Analysis and Machine Intelligence*, 14(2):239–256.

[3] Bicchi A and Kumar V (2000) Robotic grasping and contact: a review. In *Proceedings of the IEEE International Conference on Robotics and Automation*, pp. 348–353.

[4] Bower AF (2009) *Applied Mechanics of Solids*. CRC Press.

[5] Boyd SP and Wegbreit B (2007) Fast computation of optimal contact forces. *IEEE Transactions on Robotics*, 23(6):1117–1132.

[6] Brost RC and Goldberg KY (1994) A complete algorithm for synthesizing modular fixtures for polygonal parts. In *Proceedings of the IEEE International Conference on Robotics and Automation*, pp. 535–542.

[7] Buss M, Faybusovich L, and Moore J (1998) Dikin-type algorithms for dexterous grasping force optimization. *International Journal of Robotics Research*, 17(8):831–839.

[8] ChandraseKaran N, Haisler WE, and Goforth RE (1987) A finite element solution method for contact problems with friction. *International Journal for Numerical Methods in Engineering*, 24:477–495.

[9] Coppersmith D and Winograd S (1990) Matrix multiplication via arithmetic progressions. *Journal of Symbolic Computation*, 9(3):251–280.

[10] Crandall SH, Dahl NC, and Lardner TJ (1978) *An Introduction to the Mechanics of Solids*. McGraw-Hill, Inc., 2nd edition.

[11] Faugeras OD and Hebert M (1986) The representation, recognition, and locating of 3-d objects. *International Journal of Robotics Research*, 5(3):27–52.

[12] Francavilla A and Zienkiewicz OC (1975) A note on numerical computation of elastic contact problems. *International Journal for Numerical Methods in Engineering*, 9:913–924.

[13] Fung YC and Tong P (2001) *Classical and Computational Solid Mechanics*. World Scientific.

[14] Gallagher RH (1975) *Finite Element Analysis*. Prentice-Hall, Inc.

[15] Gopalakrishnan K and Goldberg K (2005) D-space and deform closure grasps of deformable parts. *International Journal of Robotics Research*, 24(11):899–910.

[16] Guo F, Lin H, and Jia YB (2013) Squeeze grasping of deformable planar objects with segment contact and stick/slip transitions. in *Proceedings of the IEEE International Conference on Robotics and Automation*, pp. 3721–3726.

[17] Hirai S, Tsuboi T, and Wada T (2001) Robust grasping manipulation of deformable objects. In *Proceedings of the IEEE International Symposium on Assembly and Task Planning*, pp. 411–416.

[18] Horn BKP (1987) Closed-form solution of absolute orientation using unit quaternions. *Journal of Optical Society of America A*, 4(4):629–642.

[19] Howe RD and Cutkosky MR (1989) Sensing skin acceleration for texture and slip perception. In *Proceedings of the IEEE International Conference on Robotics and Automation*, pp.145–150.

[20] Howe RD (1994) Tactile sensing and control of robotic manipulation. *Journal of Advanced Robotics*, 8(3):245–261.

[21] Jia YB (1995) On computing optimal planar grasps. In *Proceedings of the IEEE/RSJ International Conference on Intelligent Robots and Systems*, pp. 3:427–434.

[22] Jia YB, Guo F, and Tian J (2011) On two-finger grasping of deformable planar objects. In *Proceedings of the IEEE International Conference on Robotics and Automation*, pp. 5261–5266.

[23] Jia YB, Lin H, and Guo F (2013) Optimal two-finger squeezing of deformable object . Iin *Proceedings of the IEEE/RSJ International Conference on Intelligent Robots and Systems*, pp. 3514-3519.

[24] Kerr J and Roth B (1986) Analysis of multifingered hands. *International Journal of Robotics Research*, 4(4):3–17.

[25] Ladd AM and Kavraki LE (2004) Using motion planning for knot untangling. *International Journal of Robotics Research*, 23(7):797–808.

[26] Li Z and Sastry SS (1988) Task-oriented optimal grasping by multifingered robot hands. *IEEE Journal of Robotics and Automation*, 4(1):32–44.

[27] Luo Q and Xiao J (2006) Geometric properties of contacts involving a deformable object. In *Proceedings of the IEEE Symposium on Haptic Interfaces for Virtual Environment and Teleoperator Systems*, pp. 533–538.

[28] Lurie AI (2005) *Theory of Elasticity*. Springer-Verlag Berlin Heidelberg.

[29] Markenscoff X, Ni L, and Papadimitriou CH (1990) The geometry of grasping. *International Journal of Robotics Research*, 9(1):61–74.

[30] Markenscoff X and Papadimitriou CH (1989) Optimum grip of a polygon. *International Journal of Robotics Research*, 8(2):17–29.

[31] Matsuno T and Fukuda T (2006) Manipulation of flexible rope using topological model based on sensor information. In *Proceedings of the IEEE/RSJ International Conference on Intelligent Robots and Systems*, pp. 2638–2643.

[32] Mirtich B and Canny J (1994) Easily computable optimum grasps in 2-D and 3-D. In *Proceedings of the IEEE International Conference on Robotics and Automation*, pp. 739–741.

[33] Mishra B, Schwartz JT, and Sharir M (1987) On the existence and synthesis of multifinger positive grips. *Algorithmica*, 2(4):541–558.

[34] Mishra B (1995) Grasp metrics: optimality and complexity. In Goldberg K et al., editor, *Algorithmic Foundations of Robotics*, pp. 137–165. A. K. Peters, Boston, MA.

[35] Moll M and Kavraki LE (2006) Path planning for deformable linear objects. *IEEE Transactions on Robotics and Automation*, 22(4):625–636.

[36] Nealen A, Pett J, Alexa M, and Igarashi T (2009) GridMesh: fast and high quality 2D mesh generation for interactive 3D shape modeling. In *Proceedings of the IEEE International Conference on Shape Modeling and Applications*, pp. 155-162.

[37] Negi LS (2008) *Strength of Materials*. Tata McGraw-Hill Education.

[38] Nguyen V-D (1988) Constructing force-closure grasps. *International Journal of Robotics Research*, 7(3):3–16.

[39] Novozhilov VV (1959) *The Theory of Thin Shells*. Noordhoff, Gronigen, The Netherlands.

[40] Okamoto N and Nakazawa M (1979) Finite element incremental contact analysis with various frictional conditions. *International Journal for Numerical Methods in Engineering*, 14:337–357.

[41] Ponce J, Sullivan S, Sudsang A, Boissonnat J, and Merlet JP (1997) On computing four-finger equilibrium and force-closure grasps of polyhedral objects. *International Journal of Robotics Research*, 16(1):11–35.

[42] Ponce J, Stam D, and Faverjon B (1993) On computing two-finger force-closure grasps of curved 2D objects. *International Journal of Robotics Research*, 12(3):263–273.

[43] Reddy JN (2007) *Theory and Analysis of Elastic Plates and Shells*. CRC Press, second edition.

[44] Remde A, Henrich D, and Worn H (1999) Picking-up deformable linear objects with industrial robots. In *Proceedings of the International Symposium on Robotics*, Tokyo, Japan.

[45] Reuleaux F (1876) *The Kinematics of Machinery*. London: MacMillan. Reprinted by Dover, New York, 1963. Original title *Theoretische Kinematic*.

[46] Rice JR (1964) *The Approximation of Functions*. Addison-Wesley Publishing Company.

[47] Rimon E and Blake A (1999) Caging planar bodies by one-parameter two-fingered gripping systems. *International Journal of Robotics Research*, 18:299–318.

[48] Rimon E and Burdick J (1996) On force and form closure for multiple finger grasps. In *Proceedings of the IEEE International Conference on Robotics and Automation*, pp. 1795–1800.

[49] Rodriguez A, Mason MT, and Ferry S (2012) From caging to grasping. *International Journal of Robotics Research*, 31(7):886–900.

[50] Saada AS (1993) *Elasticity: Theory and Applications*. Krieger Publishing Company.

[51] Sachdeva TD and Ramakrishnan CV (1981) A finite element solution for the two-dimensional elastic contact problems with friction. *International Journal for Numerical Methods in Engineering*, 17:1257–1271.

[52] Saha M and Isto P (2006) Motion planning for robotic manipulation of deformable linear objects. In *Proceedings of the IEEE International Conference on Robotics and Automation*, pp. 2478–2484.

[53] Salisbury JK and Roth B (1983) Kinematic and force analysis of articulated mechanical hands. *Journal of Mechanisms, Transmissions, and Automation in Design*, 105:35–41.

[54] Schwartz JG and Sharir M (1987) Identification of partially obscured objects in two and three dimensions by matching noisy characteristic curves. *International Journal of Robotics Research*, 6(2):29–44.

[55] Sinha PR and Abel JM (1992) A contact stress model for multifingered grasps of rough objects. *IEEE Transactions on Robotics and Automation*, 8(1):7–22.

[56] Strang G (1993) *Introduction to Linear Algebra*. Wellesley-Cambridge Press, 2nd edition.

[57] Strassen V (1969) Gaussian elimination is not optimal. *Numerische Mathematik*, 13(4):354–356.

[58] Tian J and Jia YB (2010) Modeling deformations of general parametric shells grasped by a robot hand. *IEEE Transactions on Robotics*, 26(5):837–852.

[59] Trinkle JC (1992) On the stability and instantaneous velocity of grasped frictionless objects. *IEEE Transactions on Robotics and Automation*, 8(5):560–572.

[60] van der Stappen AF, Wentink C, and Overmars MH (2000) Computing immobilizing grasps of polygonal parts. *International Journal of Robotics Research*, 19(5):467–479.

[61] Wakamatsu H, Arai E, and Hirai S (2006) Knotting/unknotting manipulation of deformable linear objects. *International Journal of Robotics Research*, 25(4):371–395.

[62] Wakamatsu H and Hirai S (2004) Static modeling of linear object deformation based on differential geometry. *International Journal of Robotics Research*, 23(3):293–311.

[63] Wakamatsu H, Hirai S, and Iwata K (1996) Static analysis of deformable object grasping based on bounded force closure. In *Proceedings of the IEEE/RSJ International Conference on Intelligent Robots and Systems*, pp. 3324–3329.

# A Proof of Theorem 7

**Proof** (i) The symmetry of $C$ follows that of $M^{-1}$, which exists by Theorem 5 since $m \geq 2$. Any $\bar{\boldsymbol{\Delta}}$ uniquely induces a $2n$-vector $\boldsymbol{\Delta}$ in the form of (32). Because $K$ is positive semidefinite, by (33) we have $\bar{\boldsymbol{\Delta}}^T C \bar{\boldsymbol{\Delta}} = \boldsymbol{\Delta}^T K \boldsymbol{\Delta} \geq 0$, This establishes that $C$ is also positive semidefinite.

It follows from (30) that $B^T C = \mathbf{0}$, which implies $C^T B = CB = \mathbf{0}$ given the symmetry of $C$. Therefore, $\mathrm{col}(B) \subseteq \mathrm{null}(C)$. Meanwhile, $\mathrm{null}(C)$ has no other independent vector. Suppose there is one, say, $\bar{\boldsymbol{\xi}}$. Then it would induce a rigid body displacement $\boldsymbol{\xi}$ given by (32). This is because by (33) we have

$$\frac{1}{2}\boldsymbol{\xi}^T K \boldsymbol{\xi} = \frac{1}{2}\bar{\boldsymbol{\xi}}^T C \bar{\boldsymbol{\xi}} = 0,$$

which implies $\boldsymbol{\xi} \in \mathrm{null}(K)$. However, since $\bar{\boldsymbol{\xi}}$ is independent of $\bar{\boldsymbol{v}}_{2n-2}$, $\bar{\boldsymbol{v}}_{2n-1}$, and $\bar{\boldsymbol{v}}_{2n}$, $\boldsymbol{\xi}$ must be independent of $\boldsymbol{v}_{2n-2}$, $\boldsymbol{v}_{2n-1}$, and $\boldsymbol{v}_{2n}$, or equivalently, independent of $\boldsymbol{w}_x$, $\boldsymbol{w}_y$, and $\boldsymbol{w}_r$. This contradicts that $\mathrm{null}(K)$ has rank 3. Therefore, $\mathrm{col}(B) = \mathrm{null}(C)$. Due to the symmetry of $C$, $\mathrm{row}(C) = \mathrm{col}(C)$. This leads to

$$\begin{aligned} \mathbb{R}^{2m} &= \mathrm{null}(C) \oplus \mathrm{row}(C) \\ &= \mathrm{col}(B) \oplus \mathrm{col}(C). \end{aligned}$$

(ii) We first show that the $2m \times 3$ matrix $E$ has rank 3. Clearly, $\mathrm{rank}(E) \leq 3$. It is well known (and also easy to show) that the rank of the product of two matrices is at most the rank of either matrix. So $\mathrm{rank}(E) \geq \mathrm{rank}(B^T E) = \mathrm{rank}(I_3) = 3$. Hence $\mathrm{rank}(E) = 3$.

It then follows that $\mathrm{null}(E^T)$ has rank $2m - 3$. For any $\bar{\boldsymbol{\Delta}} \in \mathrm{null}(E^T)$,

$$\begin{aligned} E^T \bar{\boldsymbol{\Delta}} = 0 \quad &\Rightarrow \quad BE^T \bar{\boldsymbol{\Delta}} = 0 \\ &\Rightarrow \quad (I_{2m} - AC)\bar{\boldsymbol{\Delta}} = 0 \quad (\text{since } AC + BE^T = I_{2m}) \\ &\Rightarrow \quad (AC)\bar{\boldsymbol{\Delta}} = \bar{\boldsymbol{\Delta}}. \end{aligned}$$

Thus, $\bar{\boldsymbol{\Delta}}$ is an eigenvector of $AC$ corresponding to the eigenvalue 1. Because $\bar{\boldsymbol{\Delta}}$ is arbitrary from $\mathrm{null}(E^T)$, $AC$ has rank at least $2m - 3$ and a unit eigenvalue of multiplicity at least $2m - 3$. Meanwhile, for any $\bar{\boldsymbol{\Delta}} \in \mathrm{null}(C)$, we have

$$\begin{aligned} C\bar{\boldsymbol{\Delta}} = 0 \quad &\Rightarrow \quad (AC)\bar{\boldsymbol{\Delta}} = 0 \\ &\Rightarrow \quad \mathrm{rank}(AC) \leq 2m - \mathrm{rank}(\mathrm{null}(C)). \end{aligned}$$

But $\mathrm{null}(C) = \mathrm{col}(B)$ has rank 3 following part (i) of the theorem. Therefore, $AC$ has rank $2m - 3$ and only one eigenvalue 1.

(iii) The property will follow from (ii) and $\mathrm{rank}(E) = 3$ if we can show that $\mathrm{col}(AC) \perp \mathrm{col}(E)$. Equation (30) tells us that

$$\begin{array}{rcll} AE + BH = 0 & \Rightarrow & CAE + CBH = 0 & \\ & \Rightarrow & CAE = 0 & \text{(since } CB = 0\text{)} \\ & \Rightarrow & (A^T C^T)^T E = 0 & \\ & \Rightarrow & (AC)^T E = 0 & \text{(by the symmetries of } A \text{ and } C\text{)} \\ & \Rightarrow & \mathrm{col}(AC) \perp \mathrm{col}(E). & \end{array}$$

□

# B Measurement of Young's Modulus, Poisson's Ratio, and the Coefficient of Contact Friction

Young's modulus $E$ and Poisson's ratio $\nu$ of foam rubber were estimated by deforming multiple cuboids cut from a foam board, and measuring the applied forces and the resulting changes in their geometry.

The longest side $l$ of a cuboid ranged between 0.05 and 0.1. Denote by $w$ and $h$ its two other sides. The cuboid was placed against the surface of the phalanx of a finger of the Barrett Hand such that the side $l$ was perpendicular to the surface. A human finger pushed the cuboid against the phalanx by exerting a vertical force on the facet of the cuboid opposite to the one in contact with the phalanx. Assumed to be equally distributed, the force had its magnitude $f$ measured by a strain gauge sensor mounted at the joint of the fingertip. The changes in the three dimensions of the cuboid were measured as $\Delta l$, $\Delta w$, and $\Delta h$, respectively.

Because $\Delta w$ and $\Delta h$ were small compared with $w$ and $h$, Young's modulus was estimated as

$$E \approx \frac{fl}{wh\Delta l}.$$

Poisson' ratio was approximated as

$$\nu \approx -\frac{\Delta w/w}{\Delta l/l}.$$

All solid objects in the experiments were made of foam rubber.

To measure the coefficient of friction between an object and a finger, we placed a small piece of the same material of the object on a slope, which was made of the same material of the fingertip. Denote by $\alpha$ the angle between the slope and the horizontal plane. Using bisection, we searched the range $[0, \pi/2]$ for $\alpha_0$, the critical value below which the piece stayed still on the slope and above which the piece slid. Neglecting the difference between static friction and dynamic friction, the coefficient of friction was taken as $\mu = \tan \alpha_0$.

# C Matching Deformed Shapes from Simulation and Experiment

A boundary contour was first drawn on the computer screen. Based on the printout (with some enlargement), an object was cut from a foam board. When we compared two deformed shapes, generated by simulation and acquired in the experiment[21], respectively, the two sets of data points differed by scale, orientation, and translation. A homogeneous transformation needed to be found for the matching.

[21] The shape data in the experiment was generated by a scanner.

More formally, given two sets of points $P = \{\boldsymbol{p}_1, \ldots, \boldsymbol{p}_n\}$ and $Q = \{\boldsymbol{q}_1, \ldots, \boldsymbol{q}_n\}$ in the plane, where $\boldsymbol{p}_i = (x_i, y_i)^T$ corresponds to $\boldsymbol{q}_i = (u_i, v_i)^T$, for $i = 1, 2, \ldots, n$. We determine the scale $s$, rotation $\theta$, and translation $(t_x, t_y)^T$ applied to $Q$ to minimize the least-squares difference between these two point sets:

$$\mathcal{E} = \sum_i^n (\boldsymbol{p}_i - M\boldsymbol{q}_i)^T (\boldsymbol{p}_i - M\boldsymbol{q}_i), \tag{72}$$

where $M$ is the transformation matrix given by

$$M = \begin{pmatrix} s\cos\theta & -s\sin\theta & t_x \\ s\sin\theta & s\cos\theta & t_y \\ 0 & 0 & 1 \end{pmatrix}. \tag{73}$$

Least-squares matching of two point sets in two or three dimensions with known correspondences under rigid motions was solved by Faugeras and Hebert (1986), Horn (1987), and Schwartz and Sharir (1987). Matching a set of points against a 3D model up to rotation and translation (with unknown point correspondences) could be effectively carried out by the iterative closest point algorithm (Besl and Mckay, 1992).

In our application, correspondences are known but the motion is non-rigid. Write

$$(c_1, c_2, c_3, c_4, c_5, c_6, c_7, c_8, c_9, c_{10})^T = \frac{1}{n} \sum_i^n (x_i, y_i, u_i, v_i, x_i u_i, x_i v_i, y_i u_i, y_i v_i, u_i^2, v_i^2)^T.$$

Vanishing of the partial derivatives of $\mathcal{E}$ with respect to $\theta$, $s$, $t_x$, and $t_y$ yields the following equations:

$$c_3 s\cos\theta - c_4 s\sin\theta + t_x - c_1 = 0, \tag{74}$$

$$c_3 s\sin\theta + c_4 s\cos\theta + t_y - c_2 = 0, \tag{75}$$

$$(c_3\sin\theta + c_4\cos\theta)t_x + (c_4\sin\theta - c_3\cos\theta)t_y - (c_5 + c_8)\sin\theta + (c_7 - c_6)\cos\theta = 0, \tag{76}$$

$$(c_4\sin\theta - c_3\cos\theta)t_x - (c_3\sin\theta + c_4\cos\theta)t_y + (c_5 + c_8)\cos\theta + (c_7 - c_6)\sin\theta - (c_9 + c_{10})s = 0. \tag{77}$$

For the moment, we assume $c_3^2 + c_4^2 \neq 0$. Solve (74) and (75) to obtain

$$s\cos\theta = \frac{c_1 c_3 + c_2 c_4 - c_3 t_x - c_4 t_y}{c_3^2 + c_4^2}, \tag{78}$$

$$s\sin\theta = \frac{c_2 c_3 - c_1 c_4 + c_4 t_x - c_3 t_y}{c_3^2 + c_4^2}, \tag{79}$$

We also obtain, from $\cos\theta \times (76) + \sin\theta \times (77)$,

$$s\sin\theta = \frac{c_4 t_x - c_3 t_y + c_7 - c_6}{c_9 + c_{10}}; \tag{80}$$

and from $\sin\theta \times (76) - \cos\theta \times (77)$,

$$s\cos\theta = -\frac{c_3 t_x + c_4 t_y - c_5 - c_8}{c_9 + c_{10}}. \tag{81}$$

Eliminate $s\cos\theta$ from (78) and (81), and $s\sin\theta$ from (79) and (80). Then solve the two resultant equations for $t_x$ and $t_y$. To obtain $s$, square both sides of (78) and both sides of (79), and add up the two resulting

equations to eliminate $\theta$. Finally, from (78) and (79) we obtain $\theta$ after plugging the expressions for $t_x$ and $t_y$. The solution is given below:

$$t_x = \frac{c_4(c_7-c_6)-c_3(c_5+c_8)+c_1(c_9+c_{10})}{c_9+c_{10}-(c_3^2+c_4^2)}, \tag{82}$$

$$t_y = \frac{c_2(c_9+c_{10})-c_4(c_5+c_8)-c_3(c_7-c_6)}{c_9+c_{10}-(c_3^2+c_4^2)}, \tag{83}$$

$$s = \frac{\sqrt{(c_1c_3+c_2c_4-(c_5+c_8))^2+(c_1c_4-c_2c_3+(c_7-c_6))^2}}{c_9+c_{10}-(c_3^2+c_4^2)}, \tag{84}$$

$$\theta = \text{atan2}(c_7-c_6+c_1c_4-c_2c_3, c_5+c_8-(c_1c_3+c_2c_4)). \tag{85}$$

Note that $c_9+c_{10} > c_3^2+c_4^2$ for $n \geq 2$.

In the special case $c_3 = c_4 = 0$, by solving the simplified (74)–(77) directly we can verify that the solution (82)–(85) carries over and simplifies to $t_x = c_1$, $t_y = c_2$, $s = \frac{\sqrt{(c_7-c_6)^2+(c_5+c_8)^2}}{c_9+c_{10}}$ and $\theta = \text{atan2}(c_7-c_6, c_5+c_8)$.

# D Expressions Needed in Section 6

This appendix lists the missing expressions for some terms used in Section 6. In Section 6.1.1, the quadratic form (57) for $W_{\mathcal{F}}$ contains

$$H = S^T C S, \tag{86}$$

where

$$S = \begin{pmatrix} 1 & 0 & -1 & 0 & 0 & 0 \\ 0 & 1 & 0 & -1 & 0 & 0 \end{pmatrix}^T,$$

and

$$\boldsymbol{c}^T = \begin{pmatrix} \mathbf{0} \\ -\boldsymbol{a} \\ \boldsymbol{a}/2 \end{pmatrix}^T CS, \tag{87}$$

$$\omega = \frac{1}{2}\begin{pmatrix} 0 \\ -\boldsymbol{a} \\ 0 \end{pmatrix}^T C \begin{pmatrix} 0 \\ -\boldsymbol{a} \\ \boldsymbol{a} \end{pmatrix}. \tag{88}$$

The optimal displacement (61) are in the directions of $(\boldsymbol{\psi}_1^T, \boldsymbol{\psi}_2^T)^T$ where

$$\boldsymbol{\psi}_1 = -\left(\left(\frac{(\boldsymbol{p}_j-\boldsymbol{p}_k)\times\hat{\boldsymbol{a}}}{\|\boldsymbol{p}_i-\boldsymbol{p}_j\|}\hat{\boldsymbol{n}}^T H + \begin{pmatrix} 0 \\ -\hat{\boldsymbol{a}} \\ \hat{\boldsymbol{a}}/2 \end{pmatrix}^T CS\right)\hat{\boldsymbol{t}} \Big/ (\hat{\boldsymbol{t}}^T H \hat{\boldsymbol{t}})\right)\hat{\boldsymbol{t}} + \frac{(\boldsymbol{p}_j-\boldsymbol{p}_k)\times\hat{\boldsymbol{a}}}{\|\boldsymbol{p}_i-\boldsymbol{p}_j\|}\hat{\boldsymbol{n}}, \tag{89}$$

$$\boldsymbol{\psi}_2 = -\boldsymbol{a} - \boldsymbol{\psi}_1. \tag{90}$$

In Section 6.1.2, the optimal pure resistance given in (63) involves

$$\tau_1^* = \begin{pmatrix} 1 \\ N^{-1}\boldsymbol{b} \end{pmatrix}^T \left(L\begin{pmatrix} \mathbf{0} \\ N^{-1}\hat{\boldsymbol{a}} \end{pmatrix} - \frac{1}{2}(\hat{\boldsymbol{u}}_1, \hat{\boldsymbol{u}}_2, \hat{\boldsymbol{u}}_3)^T C \begin{pmatrix} \mathbf{0} \\ \mathbf{0} \\ \hat{\boldsymbol{a}} \end{pmatrix}\right) \Big/ \left(\begin{pmatrix} 1 \\ -N^{-1}\boldsymbol{b} \end{pmatrix}^T L \begin{pmatrix} 1 \\ -N^{-1}\boldsymbol{b} \end{pmatrix}\right), \tag{91}$$

where $L = (\hat{\boldsymbol{u}}_1, \hat{\boldsymbol{u}}_2, \hat{\boldsymbol{u}}_3)^T C(\hat{\boldsymbol{u}}_1, \hat{\boldsymbol{u}}_2, \hat{\boldsymbol{u}}_3)$.

In Section 6.2, the work $W_{\mathcal{F}}$ done by a stable resistance is in the form (57) with the matrix $H$ assuming the form (86) except

$$S = \left( I_2, \ldots, I_2, -\frac{|\mathbb{I}|}{|\mathbb{J}|} I_2, \ldots, -\frac{|\mathbb{I}|}{|\mathbb{J}|} I_2, \mathbf{0}, \ldots, \mathbf{0} \right)^T, \tag{92}$$

and $\boldsymbol{c}$ and $\omega$ given differently below:

$$\boldsymbol{c}^T = \begin{pmatrix} 0 \\ \vdots \\ 0 \\ -\frac{|\mathbb{K}|}{|\mathbb{J}|}\boldsymbol{a} \\ \vdots \\ -\frac{|\mathbb{K}|}{|\mathbb{J}|}\boldsymbol{a} \\ \boldsymbol{a}/2 \\ \vdots \\ \boldsymbol{a}/2 \end{pmatrix}^T CS, \qquad \text{and} \qquad \omega = \frac{1}{2} \begin{pmatrix} 0 \\ \vdots \\ 0 \\ -\frac{|\mathbb{K}|}{|\mathbb{J}|}\boldsymbol{a} \\ \vdots \\ -\frac{|\mathbb{K}|}{|\mathbb{J}|}\boldsymbol{a} \\ 0 \\ \vdots \\ 0 \end{pmatrix}^T C \begin{pmatrix} 0 \\ \vdots \\ 0 \\ -\frac{|\mathbb{K}|}{|\mathbb{J}|}\boldsymbol{a} \\ \vdots \\ -\frac{|\mathbb{K}|}{|\mathbb{J}|}\boldsymbol{a} \\ \boldsymbol{a} \\ \vdots \\ \boldsymbol{a} \end{pmatrix}. \tag{93}$$

The optimal resistance takes the form (61), where $\boldsymbol{\psi}_1$ and $\boldsymbol{\psi}_2$ are obtained from (89) and (90) by replacing $\boldsymbol{p}_i, \boldsymbol{p}_j, \boldsymbol{p}_k$ with $\breve{\boldsymbol{p}}, \breve{\boldsymbol{q}}, \breve{\boldsymbol{r}}$, respectively, and $S$ is given as (92).

Finally, for a pure resistance with segment contact, the $2m \times 3$ matrix $E = (\boldsymbol{e}_1, \boldsymbol{e}_2, \boldsymbol{e}_3)$ has full rank 3 by Theorem 7. For $1 \le t \le 3$, we denote $\boldsymbol{e}_t = (e_{1t}, \ldots, e_{2m,t})^T$. The conditions $\boldsymbol{e}_t^T \bar{\boldsymbol{\Delta}} = 0$, $1 \le t \le 3$, can be rewritten as

$$\begin{pmatrix} \breve{\boldsymbol{e}}_{11} & \breve{\boldsymbol{e}}_{12} & \breve{\boldsymbol{e}}_{13} \\ \breve{\boldsymbol{e}}_{21} & \breve{\boldsymbol{e}}_{22} & \breve{\boldsymbol{e}}_{23} \\ \breve{\boldsymbol{e}}_{31} & \breve{\boldsymbol{e}}_{32} & \breve{\boldsymbol{e}}_{33} \end{pmatrix}^T \begin{pmatrix} \boldsymbol{d}_1 \\ \boldsymbol{d}_2 \\ \boldsymbol{a} \end{pmatrix} = \mathbf{0},$$

where the $6 \times 3$ matrix has entries:

$$\breve{\boldsymbol{e}}_{st} = \begin{cases} \sum_{u \in \mathbb{I}} \binom{e_{2u-1,t}}{e_{2u,t}}, & \text{if } s = 1, \\ \sum_{u \in \mathbb{J}} \binom{e_{2u-1,t}}{e_{2u,t}}, & \text{if } s = 2, \\ \sum_{u \in \mathbb{K}} \binom{e_{2u-1,t}}{e_{2u,t}}, & \text{if } s = 3. \end{cases}$$

Generally, this matrix has rank 3, so does its null space. We use SVD to find three unit orthogonal vectors $\hat{\boldsymbol{u}}'_1, \hat{\boldsymbol{u}}'_2, \hat{\boldsymbol{u}}'_3$ that span its null space. Let $\bar{\boldsymbol{\Delta}} = \tau'_1 \hat{\boldsymbol{u}}'_1 + \tau'_2 \hat{\boldsymbol{u}}'_2 + \tau'_3 \hat{\boldsymbol{u}}'_3$.

The work done by the grasping fingers can be rewritten into the following form:

$$W_{\mathcal{F}} = \frac{1}{2} \begin{pmatrix} \boldsymbol{d}_1 \\ \boldsymbol{d}_2 \\ \mathbf{0} \end{pmatrix}^T P^T C P \begin{pmatrix} \boldsymbol{d}_1 \\ \boldsymbol{d}_2 \\ \boldsymbol{a} \end{pmatrix}, \tag{94}$$

where the $2m \times 6$ 'expansion' matrix $P$ has transpose

$$P^T = \begin{pmatrix} I_2 & \cdots & I_2 & \mathbf{0} & \cdots & \mathbf{0} & \mathbf{0} & \cdots & \mathbf{0} \\ \mathbf{0} & \cdots & \mathbf{0} & I_2 & \cdots & I_2 & \mathbf{0} & \cdots & \mathbf{0} \\ \mathbf{0} & \cdots & \mathbf{0} & \mathbf{0} & \cdots & \mathbf{0} & I_2 & \cdots & I_2 \end{pmatrix}.$$

Aside from a different form of $W_{\mathcal{F}}$ and different variables $\tau'_1, \tau'_2, \tau'_3$, the constraint over these variables is $\boldsymbol{a} = (\mathbf{0}, I_2)(\hat{\boldsymbol{u}}'_1, \hat{\boldsymbol{u}}'_2, \hat{\boldsymbol{u}}'_3)(\tau'_1, \tau'_2, \tau'_3)^T$.

## E Proof of Theorem 11

Before (57) we first write $W_{\mathcal{F}}$ from (56) into an intermediate quadratic form:

$$W_{\mathcal{F}} = \frac{1}{2}\bar{\boldsymbol{\Delta}}'^{T} C \bar{\boldsymbol{\Delta}}' + \begin{pmatrix} 0 \\ -\boldsymbol{a} \\ \boldsymbol{a}/2 \end{pmatrix}^{T} C\bar{\boldsymbol{\Delta}}' + \omega, \tag{95}$$

where $\bar{\boldsymbol{\Delta}}' = (\boldsymbol{d}_1^T, -\boldsymbol{d}_1^T, \mathbf{0}^T)^T$. The following lemma is needed for the proof the theorem.

**Lemma 13** *The 6-tuple $\bar{\boldsymbol{\Delta}}' \in \mathrm{null}(C)$ if and only if conditions (58) hold.*

**Proof** Note that $\bar{\boldsymbol{\Delta}}'$ is already orthogonal to $\bar{\boldsymbol{w}}_x = (1,0,1,0,1,0)^T$ and $\bar{\boldsymbol{w}}_y = (0,1,0,1,0,1)^T$. The vector that represents rotation is $\bar{\boldsymbol{w}}_r = (-y_i, x_i, -y_j, x_j, -y_k, x_k)^T$. Hence $\bar{\boldsymbol{\Delta}}'$ is in the null space if and only if it is collinear with the following vector:

$$\begin{aligned} \bar{\boldsymbol{w}}_\perp &= \bar{\boldsymbol{w}}_r - \frac{\bar{\boldsymbol{w}}_r \cdot \bar{\boldsymbol{w}}_x}{\bar{\boldsymbol{w}}_x \cdot \bar{\boldsymbol{w}}_x}\bar{\boldsymbol{w}}_x - \frac{\bar{\boldsymbol{w}}_r \cdot \bar{\boldsymbol{w}}_y}{\bar{\boldsymbol{w}}_y \cdot \bar{\boldsymbol{w}}_y}\bar{\boldsymbol{w}}_y \\ &= \frac{1}{3}\begin{pmatrix} -2y_i + y_j + y_k \\ 2x_i - x_j - x_k \\ y_i - 2y_j + y_k \\ -x_i + 2x_j - x_k \\ y_i + y_j - 2y_k \\ -x_i - x_j + 2x_k \end{pmatrix}. \end{aligned} \tag{96}$$

Collinearity of $\bar{\boldsymbol{\Delta}}'$ and $\bar{\boldsymbol{w}}_\perp$ is equivalent to the truths of the following four equations:

$$\begin{aligned} (-2y_i + y_j + y_k) + (y_i - 2y_j + y_k) &= 0, \\ (2x_i - x_j - x_k) + (-x_i + 2x_j - x_k) &= 0, \\ y_i + y_j - 2y_k &= 0, \\ -x_i - x_j + 2x_k &= 0. \end{aligned}$$

It is easy to verify that the last two equations above are equivalent to $\boldsymbol{p}_k = \frac{1}{2}(\boldsymbol{p}_j + \boldsymbol{p}_j)$. Also, for $\bar{\boldsymbol{\Delta}}'$ and $\bar{\boldsymbol{w}}_\perp$ to be collinear, $\boldsymbol{d}_1$ must be collinear with the first two entries in $\bar{\boldsymbol{w}}_\perp$:

$$\begin{pmatrix} -2y_i + y_j + y_k \\ 2x_i - x_j - x_k \end{pmatrix}, \qquad \text{or equivalently,} \qquad \begin{pmatrix} -y_i + y_j \\ x_i - x_j \end{pmatrix},$$

under the last two equations above. Hence, $\boldsymbol{d}_1$ is orthogonal to $\boldsymbol{p}_i - \boldsymbol{p}_j$. □

**Proof** (Theorem 11) The positive semi-definiteness of $H$ follows from that of $C$, $\boldsymbol{\Delta}'^T C \boldsymbol{\Delta}' = \boldsymbol{d}_1^T H \boldsymbol{d}_1$ by $\bar{\boldsymbol{\Delta}}' = S\bar{\boldsymbol{\Delta}}_i$ and (86), and the fact that $\boldsymbol{\Delta}' = 0$ if and only if $\boldsymbol{d}_1 = 0$. The second part of the theorem easily follows from Lemma 13. □

# F Proof of Proposition 12

**Proof** Observe that $\boldsymbol{d}_1^T H \boldsymbol{d}_1 = (S\boldsymbol{d}_1)^T C (S\boldsymbol{d}_1)$ given $H = S^T C S$. Here, $S$ is given in (92) in Appendix D, and

$$S\boldsymbol{d}_1 = \left( \boldsymbol{d}_1^T, \ldots, \boldsymbol{d}_1^T, -\frac{|\mathbb{I}|}{|\mathbb{J}|}\boldsymbol{d}_1^T, \ldots, -\frac{|\mathbb{I}|}{|\mathbb{J}|}\boldsymbol{d}_1^T, 0, \ldots, 0 \right)^T.$$

Clearly, $\boldsymbol{d}_1 = 0$ if and only if $S\boldsymbol{d}_1 = 0$. Thus, the positive semidefiniteness of $H$ follows from that of $C$.

Sufficiency of conditions i), ii), and iii) for $\boldsymbol{d}_1 \in \mathrm{null}(H)$ trivially follows from Theorem 11. To establish their necessity, suppose $\boldsymbol{d}_1 \in \mathrm{null}(H)$. Then, $S\boldsymbol{d}_1 \in \mathrm{null}(C)$. We just need to establish part i) of the proposition: $|\mathbb{I}| = |\mathbb{J}| = |\mathbb{K}| = 1$, since then parts ii) and iii) will follow from Theorem 11.

As in Appendix E, the $2(|\mathbb{I}| + |\mathbb{J}| + |\mathbb{K}|)$-tuples $\bar{\boldsymbol{w}}_x, \bar{\boldsymbol{w}}_y, \bar{\boldsymbol{w}}_r$ represent unit translations along the $x$- and $y$-axes, and a rotation of all contact points together about the origin respectively. In $\bar{\boldsymbol{w}}_r$, the tuples $(-y_t, x_t)^T$, $t \in \mathbb{I} \cup \mathbb{J} \cup K$, appear in the same index order as their corresponding displacements $\boldsymbol{\delta}_t$ in $\bar{\boldsymbol{\Delta}}$.

Since $S\boldsymbol{d}_1$ is orthogonal to $\bar{\boldsymbol{w}}_x$ and $\bar{\boldsymbol{w}}_y$, $S\boldsymbol{d}_1 \in \mathrm{null}(C)$ implies that the vector must be parallel to $\bar{\boldsymbol{w}}_\perp$, defined in (96), which now takes the form of the product of $1/q$, where $q = |\mathbb{I}| + |\mathbb{J}| + |\mathbb{K}|$, with a vector that lists the tuples

$$\begin{pmatrix} \sum_{t \in \mathbb{I} \cup \mathbb{J} \cup \mathbb{K}} y_t - q y_l \\ -\sum_{t \in \mathbb{I} \cup \mathbb{J} \cup \mathbb{K}} x_t + q x_l \end{pmatrix},$$

where the index $l$ ranges over $\mathbb{I}, \mathbb{J}, \mathbb{K}$ sequentially. From $S\boldsymbol{d}_1 \parallel \bar{\boldsymbol{w}}_\perp$, we infer that, for any $u, v \in \mathbb{I}$ with $u \neq v$,

$$\begin{aligned} 0 &= \begin{pmatrix} \sum_{t \in \mathbb{I} \cup \mathbb{J} \cup \mathbb{K}} y_t - q y_u \\ -\sum_{t \in \mathbb{I} \cup \mathbb{J} \cup \mathbb{K}} x_t + q x_u \end{pmatrix} - \begin{pmatrix} \sum_{t \in \mathbb{I} \cup \mathbb{J} \cup \mathbb{K}} y_t - q y_v \\ -\sum_{t \in \mathbb{I} \cup \mathbb{J} \cup \mathbb{K}} x_t + q x_v \end{pmatrix} \\ &= q \begin{pmatrix} y_v - y_u \\ x_u - x_v \end{pmatrix}. \end{aligned}$$

Hence $\boldsymbol{p}_u = \boldsymbol{p}_v$ whenever $u, v \in \mathbb{I}$. Similarly, we establish that $\boldsymbol{p}_u = \boldsymbol{p}_v$ whenever $u, v \in \mathbb{J}$. This establishes that $|\mathbb{I}| = |\mathbb{J}| = 1$.

Finally, $S\boldsymbol{d}_1 \parallel \bar{\boldsymbol{w}}_\perp$ implies that the last $2|\mathbb{K}|$ entries in $\bar{\boldsymbol{w}}_\perp$ are zero, that is, for $l \in \mathbb{K}$,

$$\begin{aligned} \sum_{t \in \mathbb{I} \cup \mathbb{J} \cup \mathbb{K}} y_t - q y_l &= 0, \\ -\sum_{t \in \mathbb{I} \cup \mathbb{J} \cup \mathbb{K}} x_t + q x_l &= 0. \end{aligned}$$

This yields the same point

$$\boldsymbol{p}_l = \frac{1}{q} \sum_{t \in \mathbb{I} \cup \mathbb{J} \cup \mathbb{K}} \boldsymbol{p}_t,$$

for all $l \in \mathbb{K}$. Therefore, $|\mathbb{K}| = 1$. □